Development of a High-Energy X-Ray Computed Tomography Sensor for Detecting the Solidification Front Position in Aluminum Casting

by

Mark Matthew Hytros

S.B. Mechanical Engineering, Massachusetts Institute of Technology (1994)
S.M. Mechanical Engineering, Massachusetts Institute of Technology (1996)

Submitted to the Department of Mechanical Engineering
in Partial Fulfillment of the Requirements for the Degree of

Doctor of Philosophy in Mechanical Engineering

at the

Massachusetts Institute of Technology

February 1999

Signature of Author.....
Department of Mechanical Engineering
September 30, 1998

Certified by.....
Jung-Hoon Chun
Associate Professor of Mechanical Engineering
Thesis Supervisor

Accepted by.....
Ain A. Sonin
Chairman
Departmental Committee on Graduate Students

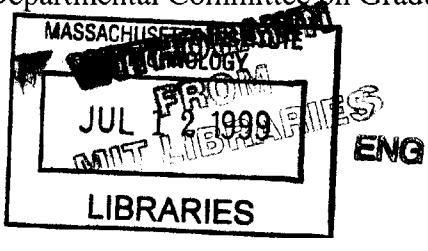

Development of a High-Energy X-Ray Computed Tomography Sensor for Detecting the Solidification Front Position in Aluminum Casting

by

Mark Matthew Hytros

Submitted to the Department of Mechanical Engineering
on September 30, 1998, in Partial Fulfillment of the
Requirements for the Degree of Doctor of Philosophy in
Mechanical Engineering

Abstract

In all casting operations, the driving physical phenomenon is the solidification of metal from the liquid to the solid phase. Solidification involves complex heat transfer, mass transfer, and fluid flow. Casting defects such as dendritic microsegregation, grain boundary segregation, interdendritic precipitation, porosity, macrosegregation, and cracks are all linked to the solidification mechanism. To better understand the dynamics of the solidification process, the development of non-invasive process sensors has been intensively researched. These sensors are based on technology such as acoustic ultrasound, laser ultrasound, laser microscopy, eddy currents, x-ray diffraction, and x-ray radiography. Although all these sensors provide information regarding the solidification process, many possess some type of shortcoming that limits their industrial potential.

This thesis developed an x-ray computed tomography-based (CT) solidification sensor as an alternative and improvement to the current technology. CT provides excellent qualitative and quantitative data on solidification dynamics and has great potential for industrial implementation. The sensor employs a 6 MeV linear accelerator (linac) emitting photons in 5 μs pulses at a rate of 180 Hz for the x-ray source. The source intensity is 300 R/min at 1 m. The x-ray beam is collimated in a 30° fan shape with a 4.5 mm beam height. A detector array comprising 128 $CdWO_4$ scintillator elements is located 845 mm from the source. The performance characteristics of the sensor include a spatial resolution of 1.76 mm, a contrast resolution of 1.1%, and data acquisition time of 120 seconds. Typical reconstruction time for a CT image ranges from 5 seconds to 60 minutes, depending on the final image parameters.

Solidification experiments were conducted using pure aluminum, Al-11.2wt.%Cu, Al-29.7wt.%Cu, and 6061 aluminum alloy. The aluminum, placed in a clay-graphite crucible (178 mm OD, 146 mm ID), was melted in a resistance heater furnace. A cooling tube at the center of the crucible solidified the molten aluminum to simulate the casting process. A solidification front formed around the tube and progressed outward until the aluminum was completely solidified. X-ray attenuation measurements were taken every minute during this time. CT later reconstructed density images from these measurements.

For pure aluminum, the progression of the solidification front position was well identified. The density maps agreed with expected values and correlated well with temperature measurements obtained independently by thermocouples. For the Al-11.2wt.%Cu and the Al-29.7wt.%Cu, a discrete solidification front was not evident because of the presence of a mushy zone. The solidification dynamics were better observed by performing a region-of-interest analysis on the density maps. The density maps correlated well with post-solidification metallographic analyses and hardness tests. For the 6061 aluminum alloy, CT imaging revealed the formation of significant porosity and voids. The size, shape, and location of these defects were confirmed through post-solidification visual inspection.

Thesis Committee:
Prof. Jung-Hoon Chun, Associate Professor of Mechanical Engineering, Committee Chairman
Prof. Derek Rowell, Professor of Mechanical Engineering
Dr. Richard Lanza, Senior Research Scientist of Nuclear Engineering
Dr. Nannaji Saka, Principal Research Scientist of Mechanical Engineering
Dr. Ho Yu, Senior Research Specialist, Aluminum Company of America

Acknowledgements

Looking back on the last eight years of my life, all of which were spent as an engineering student at MIT, I often wonder whether a Ph.D. degree was worth pursing. I guess only time will tell. Regardless, there are many people who deserve to be thanked for their contributions towards my thesis work. First and foremost, I would like to thank my co-worker on this research project, Imad Jureidini. When working on a project of this magnitude and duration, the most important factor is the relationship you have with the people you see on a daily basis. I feel truly lucky to have had Imad for a colleague. Long after I forget about x-rays, linacs, and solidification, I will still remember Subspace, that Indian restaurant, Allez Les Bleues, and all the other minutia that made the lab fun. We'll have to go back to Kelly's one day – for which I am officially preempting for right now!

I would like to thank my advisor, Professor Jung-Hoon Chun, and my thesis committee, Dr. Richard Lanza, Dr. Nannaji Saka, Professor Derek Rowell, and Dr. Ho Yu, for their input and direction on the outcome of this thesis work. I would like to thank the LMP machine shop staff, including Fred Cote, Gerry Wentworth, and Mark Belanger, for their help with building many of the parts that went into this project. I would like to thank the LMP and Mechanical Engineering Department staff, including Geoff Barss, Julie Drennan, and Leslie Regan for their help with much of the bureaucratic work.

I would like to thank Tim Roney, Tim White, and Dennis Kunerth of the Idaho National Engineering and Environmental Laboratory for their assistance in procuring the linear accelerator as well as their general insight regarding the development of our high-energy CT system. I would like to thank Russ Schonberg and David Skowbo of Schonberg Research Corporation, for their instruction on operating and troubleshooting the linear accelerator. I would also like to thank John Dobbs of Analogic Corporation, for providing the detector array and associated electronics. I would like to thank Richard Appel for his work on the detector data acquisition system.

I would like to thank the many people at the Bates Linear Accelerator Laboratory for their support and cooperation in helping to build and maintain the CastScan lab. There are countless Bates personnel who deserve credit, but in particular I would like to mention Chris Tschalaer, John Quattrochi, Dennis Boyden, Ken Hatch, Jim Grenham, Bob Avril, and Dick Ackerson.

I would like to thank several individuals from the MIT Materials Science Department. These include Harold Larson and Toby Bashaw for their assistance in the foundry, Yin-Lin Xie for her assistance with the metallography, and Joe Adario for his assistance with the spectroscopy.

I would like to thank Erik Norton and Melissa Kuroda for giving me a place to stay during the last months of my thesis work. Their kindness and generosity will never be forgotten. I hope one day I will be able to repay them in *spades* (or Scotland)! I would also like to thank Erik Newboe and Annie Devedjian for their ceaseless encouragement and support when things were looking bleak.

This research was funded by the National Science Foundation (Grant No. DMI-9522973), the Idaho National Engineering and Environmental Laboratory – University Research Consortium (Contract No. C95-175002-LKK-267-95, LITCO award No. N135-Phase III), and the CastScan Consortium, which consists of the Aluminum Company of America, Inland Steel Industries and the Reynolds Metals Company.

For Mom and Dad
without your love, support, care, and guidance,
I would not be here

Contents

Appendix

List of Figures

List of Tables

Chapter 1 Introduction

1.1 Background

The casting of liquid metal into a mold to obtain a finished part is one of the oldest and most useful manufacturing processes. It offers tremendous versatility in terms of the size and shape of the final product, allowing complex shapes, internal geometries, or very large dimensions. There are several categories of casting processes, the main division being that of discrete casting versus continuous casting. Discrete casting involves the manufacture of single or multiple near-net-shape parts from either a permanent or expendable mold. Continuous casting differs greatly from discrete casting. It resembles an extrusion or rolling process in that the output of the operation is not a near-net-shape part, but a continuous strand of metal of a chosen cross-section. The primary purpose of continuous casting is the bulk production of metal, such as steel or aluminum, in finite geometries such as billets or slabs for use in secondary manufacturing operations. In all casting operations, continuous or discrete, the driving physical phenomenon is the solidification of the metal from the liquid to solid.

The solidification of molten metal involves complex fluid flow and heat and mass transfer phenomena. Fluid flow during solidification has a large influence on both the crystal structure and homogeneity of the metal casting, as documented by Fisher (1981). Cole (1971) reports that the interactions that take place when a liquid becomes solid may produce structural inhomogeneities of various types. These include dendritic microsegregation, grain boundary segregation, interdendritic precipitation, and porosity at the microscopic level. At the macroscopic level, solidification can affect macrosegregation. With respect to continuous casting, Bobadilla et al. (1993) report that the origins of axial macrosegregation, V-shaped segregates, segregated cracks, and porosity are all linked to the final moments of solidification in a bloom or slab. Cole (1971) asserts that if the defects that accompany solidification can be clearly specified, many of the steps between initial solidification and a final homogeneous product can be reduced.

Currently, computer simulations are used to model the complex solidification behavior in a casting (Chidiac et al., 1993; Lewis and Roberts, 1987; Dalhuijsen and Segal, 1986). However, simulations require precise knowledge of the shape and extent of the solute boundary layer, real growth rate, interface morphology, and nucleation (Curreri and Kaukler, 1996). In addition, interpolations must often be made, always introducing some degree of uncertainty. Lack of adequate thermophysical data, particularly for commercial alloys, is another barrier to accurate modeling. Ultimately, simulations need to be validated, however, current experimental techniques are expensive and fraught with error (Giamei, 1993).

1.2 Review of Literature

Because of the crucial role solidification plays in metal casting, a significant amount of scientific and industrial research has been devoted to understanding the solidification process. One large area of study is that of solidification sensors, which aim to experimentally monitor characteristics of the evolving solidification front. This work has produced a variety of different techniques and methodologies.

1.2.1 Direct Measurement Techniques

One of the simplest methods of obtaining information about the solidification front is to mount a tree of thermocouples inside a metal ingot as it solidifies to acquire direct temperature measurements. Bakken and Bergstrom (1986) used this technique in the direct-chill casting of aluminum to determine surface temperature, heat flux, and heat transfer coefficients. These data were later used to verify and improve computer modeling. Although thermocouples placed inside an ingot are an excellent tool, their presence is intrusive to the casting process, which limits their usage. One alternative is to mount thermocouples inside the mold rather than in the metal ingot, as was done for the continuous steel casting process by Ozgu et al. (1985). The temperature measurements were used to calculate time-dependent heat fluxes and heat transfer coefficients for the process which were later incorporated into a two-dimensional solidification model. The major benefit of this technique is that it is non-intrusive. However, the information acquired on the position and evolution of the solidification front is now gathered indirectly, requiring the temperature in the ingot to be extrapolated from the mold temperature data. In general, thermocouple techniques may suffer from slow response time, signal noise, and lack of measurement repeatability.

Story et al. (1993) reported on a liquid core monitoring system for the continuous casting process using segment load measurements. Segment loads, which are greatly influenced by the ferrostatic pressure associated with the presence of a liquid zone, are measured using strain gauges positioned on the segment thickness setting pins. The location of the final solidification point in a cast steel strand is determined by recognizing the transition in segment load between the liquid and solid regions. Schade et al. (1994) documented an increase of 4% in caster line speed through implementation of a liquid core monitoring and control system. It is evident that liquid core monitoring is industrially beneficial. However, it does not yield any significant quantitative information about the shape, position, or movement of the solidification front. In addition, although liquid core monitoring is well suited for continuous casting, it does not transfer well to other types of casting.

1.2.2 Non-Destructive Evaluation Techniques

The benefit of a sensor that does not interfere with the solidification process has fueled the development of many non-destructive evaluation (NDE) techniques. Parker (1983) described a pulsed-echo ultrasonic flaw detector that operates on the principle that longitudinal sound velocity and density are lower in the liquid portion of a casting than in the solid portion. Consequently, the solidification front in a metal casting can be identified because it produces a reflection in the ultrasonic pulse. Laboratory tests using acoustic ultrasound techniques have been attempted on solidification in tin and tin alloys and aluminum and aluminum alloys. Suzuki et al. (1987) reported real-time sensor capability in detecting the solidification front position in tin with a spatial resolution of 10 μm in a 32 mm diameter cylindrical sample. Jen et al. (1997) documented the use of an acoustic ultrasound sensor for monitoring mold filling, gap development, and solidification front movement in aluminum die casting. They encountered problems because casting conditions such as temperature, pressure, melt cleanliness, and mold coating affect the sensor efficiency. As a result, it is difficult to obtain the ultrasonic attenuation in the aluminum part accurately. In addition, once an air gap develops between the aluminum and the mold, the sensor becomes ineffective because the ultrasound cannot be transmitted into the part.

In contrast to acoustic ultrasound, Walter and Telschow (1996) tested a laser ultrasonic sensor to measure the solidification front in tin and tin-lead alloys. A pulsed Nd-YAG laser with a 4 mm spot size generated ultrasonic waves in the liquid metal by ablation. The signal was detected with a confocal interferometer using an argon laser. The system was tested on a moving solidification front in 80 mm of pure tin and Sn-0.6%Pb alloy. Walter and Telschow were able to record the location of the solidification front in both cases, although difficulties were encountered when the solidification front moved faster than 0.1 mm/min. In addition, the presence of a mushy zone scattered the ultrasonic wave and decreased the reflected signal amplitude. Chikama et al. (1996) used a confocal laser microscope combined with an infrared image furnace to study the growth of crystals in iron-carbon alloy melts. The confocal scanning microscope had a resolution of 0.5 μm and employed a 1.5 mW He-Ne laser. Tests were carried out using Fe-0.83%C and Fe-0.2%C disks having a 4.3 mm diameter and 2 mm thickness. Results in both cases show the planar to cellular and cellular to dendritic crystal transition and cell coarsening.

Kunerth and Wallace (1980) used eddy currents to monitor the solidification in pure lead and Pb-20%Sn samples. An eddy current sensor exploits the conductivity discontinuity between the liquid and solid phases of a metal. Because of this discontinuity, the amplitude and phase of reflected electromagnetic radiation are descriptive of the change in conductivity and the depth at which the change occurs. The extent of solidification in a metal can be determined by continuously monitoring the reflected electromagnetic radiation's amplitude and phase. The results showed that morphological data regarding the solidification front were present in the eddy current measurements. However, the

measurements were subject to errors from thermal gradients present in the mold or melt and segregation effects that altered the conductivity of the metal.

1.2.3 X-Ray Techniques

A subset of non-destructive evaluation techniques involves those sensors that employ and detect x-ray radiation. Fitting et al. (1996) described one such process of locating the boundary in a solidifying metal by measuring the ordered Laue pattern of diffracted x-rays. They used an x-ray tube with a 1.2 mm spot size and a variable x-ray energy that was set at 160 kV for the solidification experiments. The x-rays were measured using a scintillator screen coupled to an image intensifier and CCD camera. To test the apparatus, a 22 mm diameter rod of pure aluminum was melted in a quartz tube furnace and x-ray diffraction measurements were recorded. The results showed an ordered diffraction pattern when the aluminum was in a solid state. As the aluminum neared the melting point, the pattern began to degenerate and eventually resulted in a diffuse ring of scattering when the aluminum was fully melted. In a similar approach, Matsumiya et al. (1987) used synchrotron orbital x-ray radiation to observe solidification in a 300 μm by 10 mm by 50 mm specimen of 3% silicon steel. The x-ray beam was 8 mm in diameter. The Laue spots were observed using an x-ray vidicon camera. Although x-ray diffraction measurements unmistakably differentiate between the solid and liquid states of a metal, the quantitative information regarding the solidification front position, evolution, and characteristics attainable through this technique is limited.

Deryabina and Ripp (1980) reported on the use of x-ray attenuation measurements through a continuously cast steel billet. X-ray radiation was produced using a Cobalt-60 (Co^{60}) radioisotope. The x-rays were detected with a CsI scintillation crystal and photomultiplier. By projecting the x-rays through the steel billet during casting and measuring the transmitted and scattered intensities along a single path, the ratio of the solid phase to the liquid phase in the billet can be determined. This information was used to calculate the shell thickness of the billet at the measurement point and provide feedback to control caster speed to avoid breakout accidents.

A common method of detecting the solidification front evolution in a metal casting is by x-ray radiography. Pool and Koster (1994) used a 160 kV x-ray source with a spot size of 0.4 mm to acquire x-ray images of the solidification of gallium with a CsI fluoroscopic screen and CCD camera in real time. The 3% density difference between the liquid and solid states was easily visualized. Curreri and Kaukler (1996) performed x-ray radiography studies on the solidification of 1 mm thick samples of aluminum-indium. Using a 100 kV x-ray source with a spot size of 5 μm, the solidification front was visualized with a spatial resolution of 30 μm and a contrast resolution of 2%. Further studies by Kaukler et al. (1997) using the same x-ray sensor showed lead precipitate formation ahead of a moving solidification

front in 1 mm thick Al-1.5%Pb alloy. Using the same radiography apparatus, Sen et al. (1997) documented the solidification front evolution of pure aluminum near 500 μm diameter ZrO_2 particles and 500 to 1000 μm diameter voids. X-ray radiography studies such as these provide insight on the evolution and characteristics of solidification. The majority of these techniques operate in real time and yield sub-millimeter spatial resolution with low noise. However, the low photon energy and source strength limits the use of x-ray radiography for metal samples thicker than a few centimeters. This limits the industrial feasibility of an x-ray radiography-based sensor. In addition, techniques such as x-ray radiography produce a single projected view through an object, similar to a medical x-ray. Consequently, there is no depth information about the solidification front.

A natural extension of x-ray radiography is the use of x-ray computed tomography (CT). CT produces two or three-dimensional information on the interior of a solidifying casting. Nagarkar et al. (1993) used an x-ray CT sensor to monitor the melt interface in the production of cadmium telluride crystals. The x-ray source was a 662 keV Cs^{137} radioisotope. The detector system consisted of three 7 mm by 2 mm by 2 mm CdTe scintillators. Nagarkar et al. used this CT system to successfully capture images of the melt interface in the semiconductor crystal with a spatial resolution of 0.7 mm. The 2.5% to 3% difference between the liquid tellurium and the solid CdTe crystal was readily visible. Chen and Chen (1991) used an x-ray CT system to verify the porosity of the mushy zone in an aqueous ammonium chloride solution. After performing a series of cooling experiments on 30% NH_4Cl-H_2O solution, CT scans were carried out on the 10 mm thick mushy zone in the steady-state solution. The density variation across the mushy zone was identified and visual images of the plumes and chimneys were captured.

1.3 Sensor Concept

Although all current sensor technologies provide some degree of information regarding the solidification process, many have some shortcoming. Most of these shortcomings limit the industrial potential of the particular sensor technique in question. Computed tomography, however, offers the possibility of a non-invasive sensor system with the potential of industrial application.

CT-based sensors have been used in non-medical applications since the mid-1980s. The implementation has been mostly limited to defect inspection and dimensional measurement of finished parts, as described by Ross and McQueeney (1990) and Bossi and Georgeson (1992). The feasibility of CT as a method of detecting solidification phenomena was documented in the work of both Nagarkar et al. and Chen and Chen. However, work in this area has thus far been limited to non-metallic materials. Although the solidification studies on semiconductor crystal and aqueous ammonium chloride are

intriguing, the thermophysical and transport properties of these materials differ significantly from those of metals.

A CT sensor for metal solidification is based on the attenuation of x-rays of sufficient energy through the solidifying cast part as well as through any surrounding equipment (Chun et al., 1996). A schematic of this sensor is shown in Figure 1-1. Radiation from an x-ray source is collimated to produce a narrow beam. The beam exits the aperture of the collimator and traverses a path from the source to the detector array. Along this path, the x-ray beam travels through air, the solidified metal shell, the liquid metal core, the solidified metal shell again, and finally through air to the detector. As it travels, the x-ray beam interacts with the material it encounters and is attenuated by the solid and liquid metal. Thus, the incident beam intensity produced at the source will be greater than the transmitted beam intensity at the detector. Since the mass attenuation coefficients of liquid and solid metals are the same while their densities are different (Evans, 1972), the thickness of the liquid and solid phases of the metal that the x-ray beam encounters can be calculated. A complete profile of the density distribution within the strand is mapped by translating and rotating the source and detector about the casting. If the scanning and processing are done rapidly, a real-time, two or three-dimensional image of the solidification front within the casting is generated.

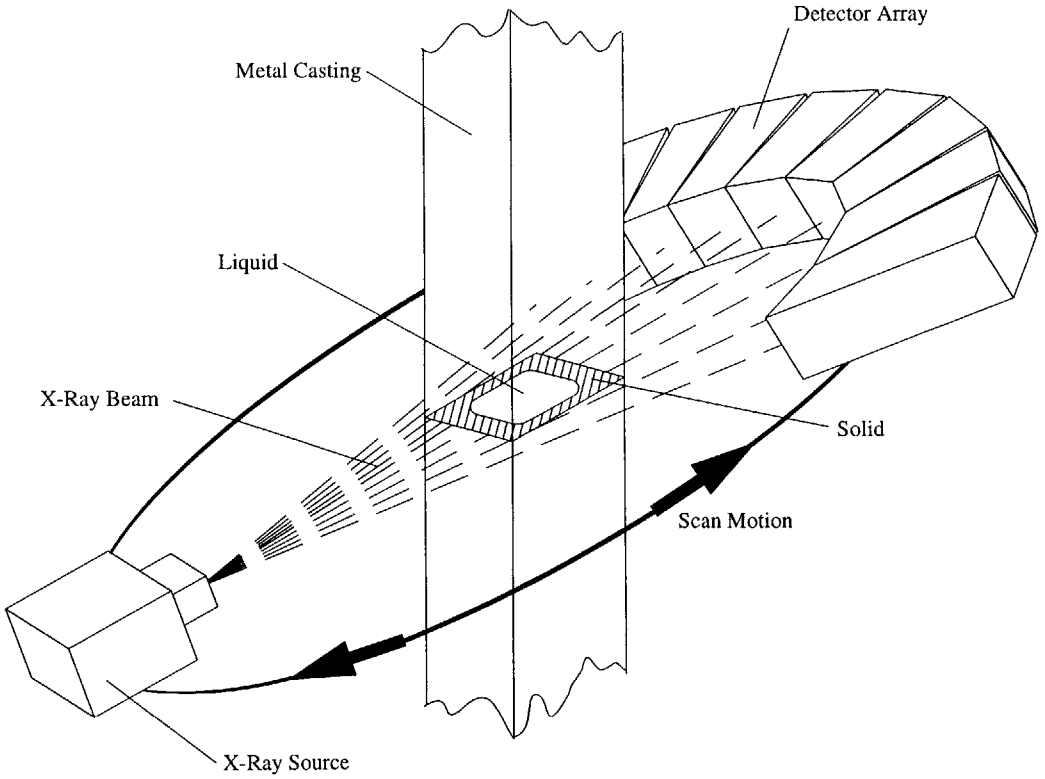

Figure 1-1: Schematic of a CT-based solidification sensor

1.4 Previous Work

In prior work, a feasibility study was conducted to verify the potential of using CT as a method of detecting the liquid/solid interface in a metal (Hytros, 1996). Because of tin's low melting point, solidification experiments were performed using pure tin contained in a graphite crucible (51 mm ID, 64 mm OD, 152 mm length). The tin was melted by a 500 W cartridge heater inside the crucible and solidified by chilled circulating water around the crucible's exterior. Varying the current to the heater and the flow rate of the water maintained the tin in a partially solidified steady state. The crucible had sixteen chromel-alumel thermocouples mounted inside it. Temperature measurements from the thermocouples monitored the exact position of the solidification front.

The CT system consisted of a 7 mCi Co^{60} radioisotope as the radiation source and a single NaI scintillation crystal coupled to a photomultiplier as the detector. A Co^{60} source produces γ-ray (identical to x-ray) radiation in two discrete energy bands, 1.16 MeV and 1.33 MeV. In this study, the γ-rays from the Co^{60} source were collimated into a 6 mm diameter pencil beam at the source. The NaI detector was collimated with a 2 mm diameter aperture. The pencil-beam, single detector arrangement necessitated a translate/rotate data acquisition scheme to acquire the proper number of view angles for CT reconstruction. This was accomplished by mounting the solidification experiment on a rotary and translational stage. Figure 1-2 is a schematic of the experimental setup.

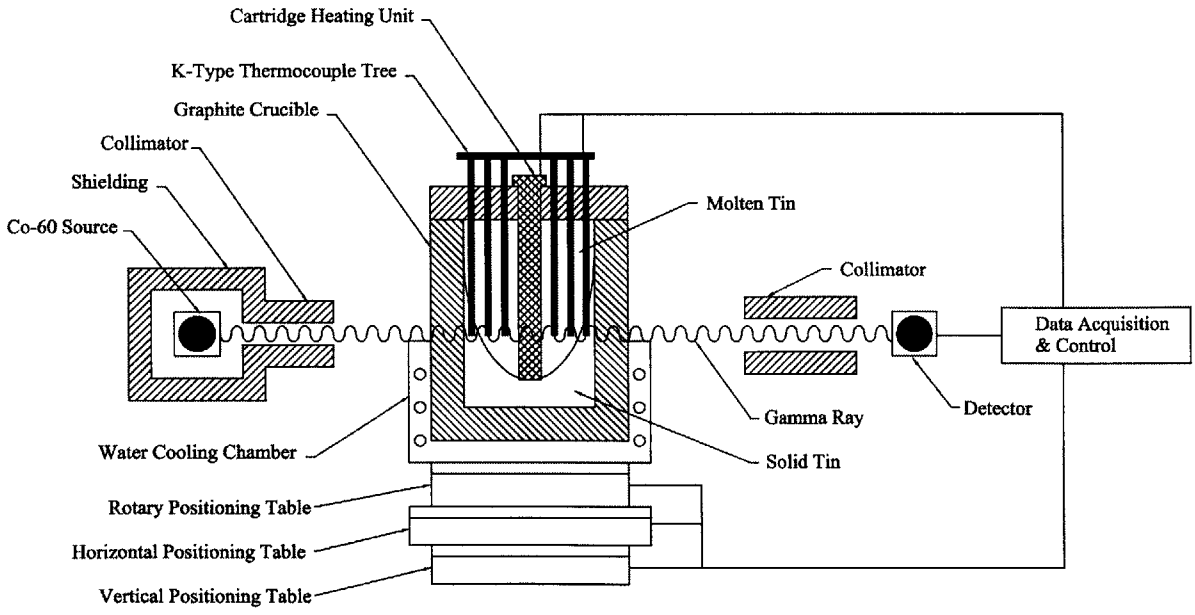

Figure 1-2: Schematic of the Co^{60}-based solidification experiment.

CT scans of the experiment, in the form of γ-ray attenuation data, were acquired once the solidification front of the two-phase tin reached a quasi-steady state. Measurements were recorded at a mid-section through the crucible, in line with the ends of the thermocouples. Figure 1-3 shows a photograph of the experiment. There were 67 transverse measurements (1.9 mm step size) and 60 view angles (3.0° step size). Data were acquired in a photon counting mode, with each measurement acquired over 300 seconds. This resulted in an overall data acquisition time of approximately 14 days.

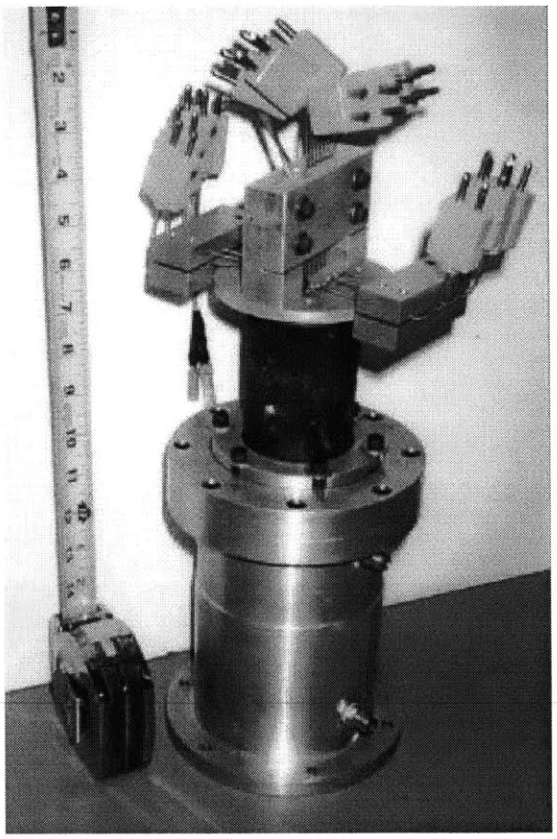

Figure 1-3: The apparatus for the pure tin solidification experiment.

The CT image was reconstructed using a standard pencil-beam filtered back-projection (FBP) algorithm with a high-cutoff frequency ramp filter. A CT image from the experiment is shown in Figure 1-4. The liquid and solid regions of the pure tin were discernable in the CT image. This density difference is more evident when the pixel values are plotted as a function of position, as shown in Figure 1-4c. Although much noise is present, the image does validate CT as a potential solidification detection tool. However, as witnessed from the image, the spatial and contrast resolutions were poor. In addition, the data acquisition time was unacceptably long. The poor image quality and slow system performance

stem primarily from the choice of x-ray source and detector. The 7 mCi Co^{60} radioisotope did not have a high enough γ-ray flux for efficient data acquisition. When coupled with only a single detector, long sample times were required to produce statistically significant data. The long data acquisition time introduced another source of error–fluctuations in solidification front position–which caused a blurring in the CT image.

Obviously, a single detector, radioisotope-based CT sensor is neither practical nor desirable. Despite the limitations, this study found potential in using CT to monitor solidification in metals. Improved CT image quality and decreased data acquisition time *could* be realized through the use of a high-flux radiation source and a multi-channel data acquisition system.

1.5 Research Goals

The intent of the project at hand is to:

- Develop a high-energy, linear accelerator-based CT sensor system capable of achieving a spatial resolution of 1 mm, a contrast resolution of 1%, and a data acquisition time of 1 second (near real-time). The prototype CT sensor should have the potential for implementation in an industrial environment with only limited modification or revision.
- Develop a platform for simulating the solidification conditions of an industrial-size metal casting.
- Evaluate the capabilities of the CT-based sensor in detecting the evolution of the solidification front in pure aluminum.
- Evaluate the capabilities of the CT-based sensor in detecting the evolution of the solidification front and mushy zone in a variety of aluminum alloys (binary hypoeutectic, binary eutectic, and commercial grade).
- Discuss possible improvements for future development from laboratory prototype to industrial implementation.

As evident from the ongoing research in the field of sensor development, an effective method to non-invasively monitor the solidification front position and evolution during the metal casting process does not exist. CT-based sensors have been examined, but limited work has been done to test their application using metals. In addition, past development has been hampered by the lack of x-ray producing equipment adequate to penetrate large metal castings. This work is the first of its kind to observe the solidification front evolution in large-sized castings of aluminum and aluminum alloy using high-energy CT.

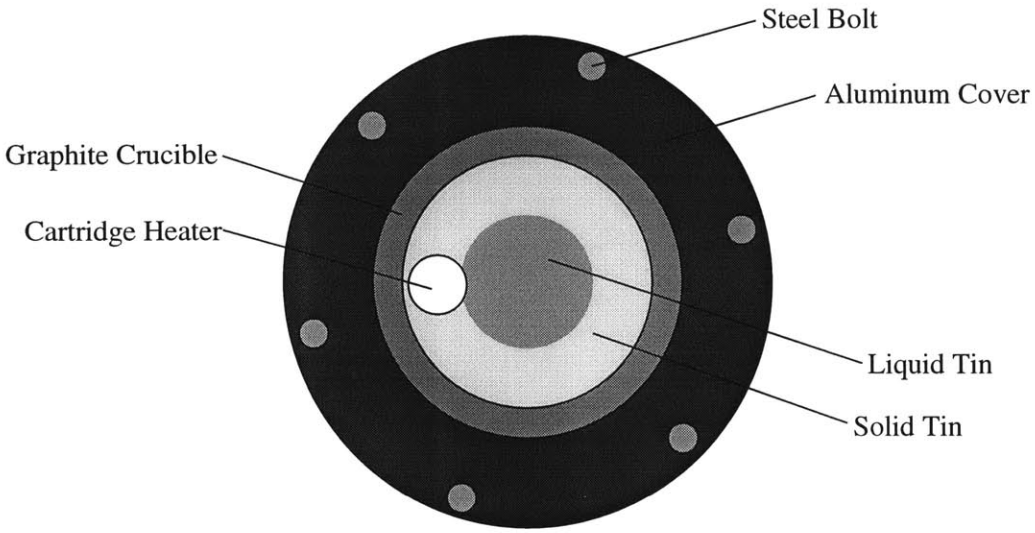

(a)

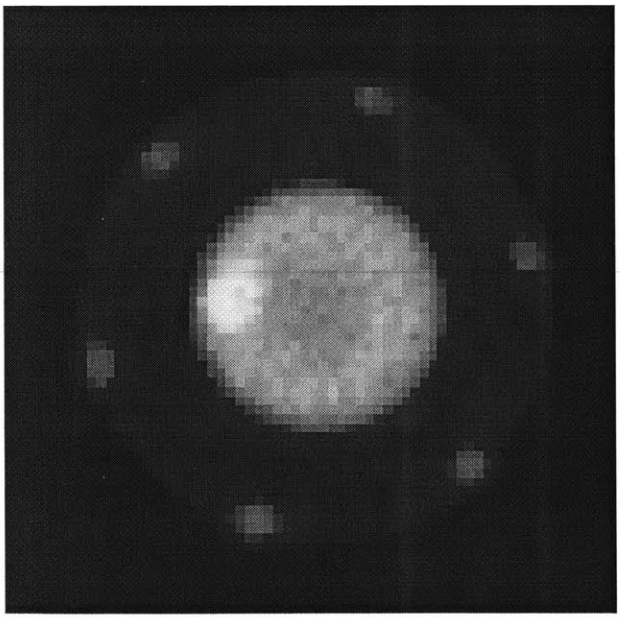

(b)

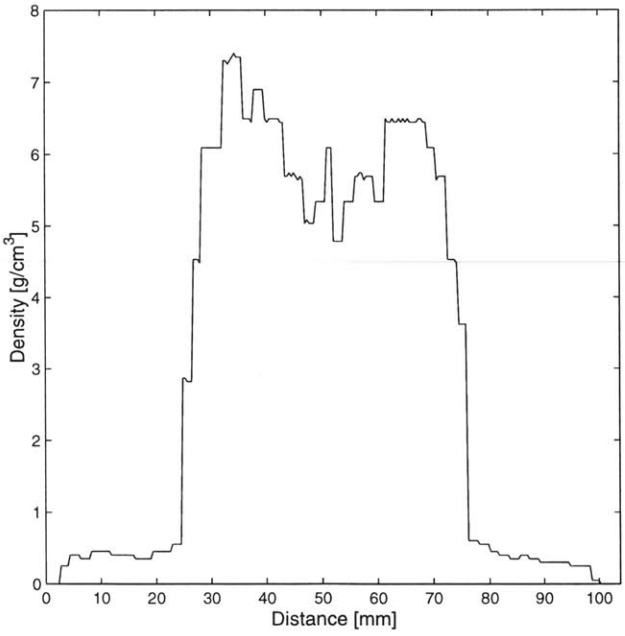

(c)

Figure 1-4: (a) Schematic of image features. (b) CT image of solidifying tin and surrounding apparatus. (c) Plot of computed density vs. position taken through a vertical cross-section of the CT image.

1.6 Outline

This chapter provides an introduction to the project, a review of the previous work by others in the field of solidification sensors, and a summary of prior work on a CT-based solidification monitor. The goals of this thesis are also stated. Chapter 2 discusses the prototype sensor design, the principles governing its operation, and its performance characteristics. Chapter 3 covers the design and performance of the laboratory solidification experiment. It also shows and discusses the results of using the CT sensor on solidification where a discrete liquid/solid interface is present. Chapter 4 presents the results and discusses the use of this sensor on metals in which a mushy zone is present. The metals tested include two binary aluminum alloys (Al-11.2wt.%Cu and Al-29.7wt.%Cu) and a commercial aluminum alloy (6061). Chapter 5 concludes by summarizing the implications of the current prototype sensor, discussing its application in the casting industry and its potential for scale-up to an industrial environment, and making recommendations for future work. Appendix A provides detailed information regarding the linear accelerator and its operation. Appendix B provides a detailed description of the heat transfer calculations used in predicting the time of the solidification experiment.

Chapter 2 CT Sensor: Principles, Design, and Performance

2.1 Principles

Computed tomography visualizes a two-dimensional cross-section through the interior of an object at a chosen view-plane, or slice. A three-dimensional image of the object is reconstructed by combining multiple two-dimensional slices. Hounsfield originally developed CT for the field of medicine in the 1970s, where it revolutionized the process of diagnostic imaging with its ability to provide detailed information non-invasively (Moore, 1990). This ability to investigate the interior of a material non-destructively led to application of CT in industry.

The basic principles of CT are best understood when compared to the technique of radiography, such as the common medical x-ray. Figure 2-1 shows a simple example of the differences in imaging ability between the two methods. In radiography, radiation is directed perpendicular to an object, or phantom, at a *single* view. The image reproduced represents the total radiation attenuation through the thickness of the object. As a result, any difference between object density and object thickness along a particular path from source to image plane cannot be resolved. In contrast, radiation is directed through a phantom at *multiple* view angles in CT, as depicted in Figure 2-2. The radiation attenuation at multiple positions is then recorded. Using the attenuation data from these multiple view angles, the local attenuation value for a small volume element within the object is calculated. The local attenuation value is a material-dependent property, independent of object geometry (Evans, 1972). Consequently, the distribution of the local attenuation values reconstructs an image of the interior of the object. The image is representative of a thin slice parallel to the incident radiation beam.

2.1.1 X-Ray Attenuation

Fundamentally, x-ray photons are absorbed or scattered in a single event. Any photons that undergo an interaction are completely removed from an x-ray's path-of-travel. As a result, x-ray photons display exponential attenuation behavior. The probability, P, that a single photon will not undergo one of the three main interactions (photoelectric effect, pair-production, Compton scattering) while traversing through a path length, x, is:

$$P = e^{-\int_0^x p ds} \qquad 2.1$$

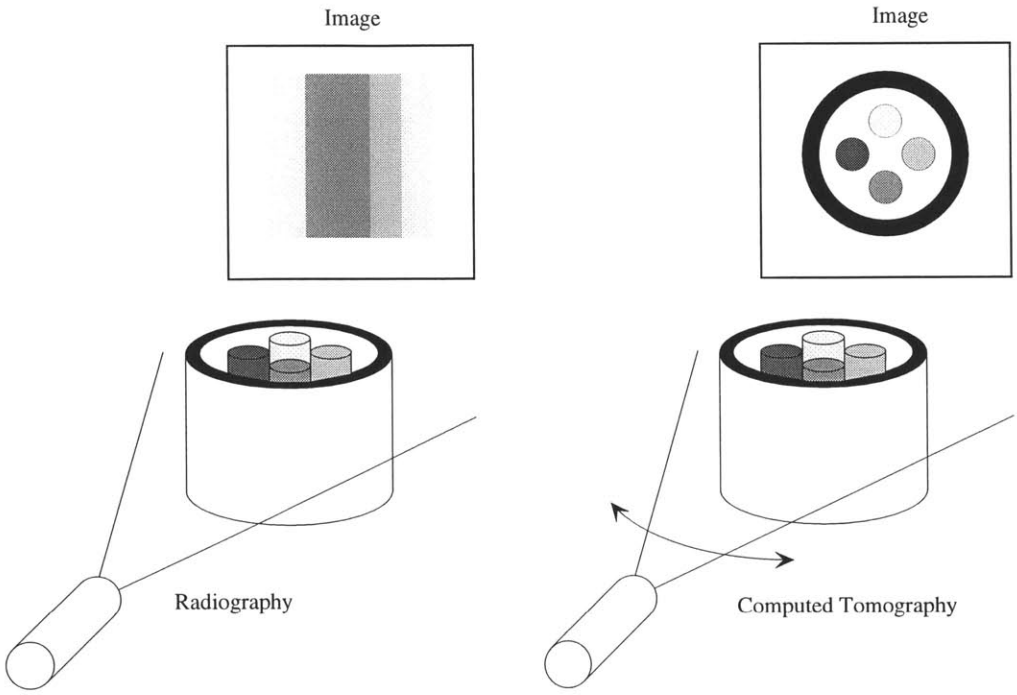

Figure 2-1: Comparison of radiography and CT imaging techniques.

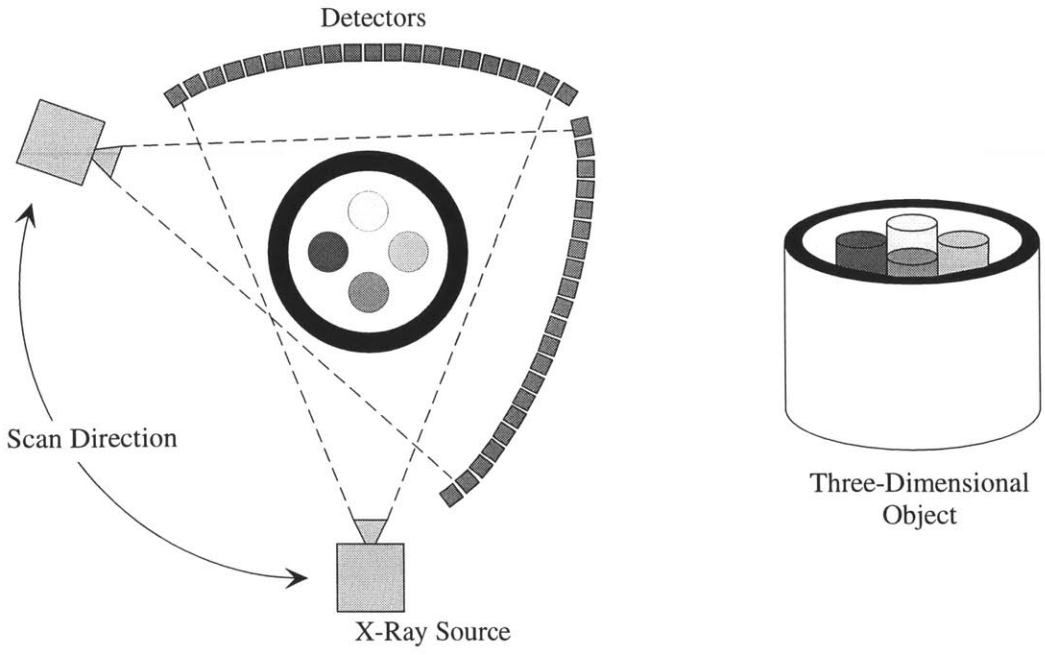

Figure 2-2: Schematic of CT imaging technique.

where p is the probability of the particular interaction per unit length. When all three interaction methods are considered, the probability of interaction per unit length is known as the linear attenuation coefficient, μ_o, defined as:

$$\mu_o = N(\tau + \kappa + Z\sigma) \tag{2.2}$$

where N is the number of atoms per unit volume of the traversed material, τ is the probability of photoelectric absorption per atomic cross-section, κ is the probability of pair production per atomic cross-section, Z is the material atomic number, and σ is the probability of Compton scattering per atomic cross-section. As a result, the number of photons, I, which pass through an object is:

$$I(s) = I_o e^{-\int_0^x \mu_o ds} \tag{2.3}$$

where I_o is the number of photons incident to the object. When calculating x–ray attenuation, the mass attenuation coefficient, μ, is more often used. The mass attenuation coefficient is independent of the density and physical state of the material and varies only as a function of photon energy. It is defined as:

$$\mu = \frac{\mu_o}{\rho} \tag{2.4}$$

where ρ is the density of the material. Substituting Equation 2.4 into Equation 2.3, derives Beer's Law, which is:

$$I(s) = I_o e^{-\int_0^x \rho \mu ds} \tag{2.5}$$

Since both the density and mass attenuation coefficient vary for an object composed of several different materials, Beer's Law is more appropriately written as:

$$I(s) = I_o e^{-\int_0^x \rho(s)\mu(s) ds} \tag{2.6}$$

2.1.2 CT Reconstruction

In CT, line integrals of the x-ray attenuation measurement over various angles about an object are reconstructed into a planar image of the object. The image plane is divided into two coordinate systems, as shown in Figure 2-3. The first is the object coordinate system (x,y), defined in the plane of the object.

The second is the projection coordinate system (z, θ), which describes a set of attenuation measurements through the object. The origin of both coordinate systems is at the center of rotation of the object. As seen in Figure 2-3, the quantity $p(z, \theta)$ is a function of both z and θ. Its analytical form is:

$$p(z,\theta) = \iint \mu_o(x, y)\delta(x\cos\theta + y\sin\theta - z)dxdy \qquad 2.7$$

Equation 2.7 maps the (x,y) coordinate system to the (z,θ) coordinate system. This is the Radon transformation (Kak and Slaney, 1987; Cho et al., 1993). The result of the Radon transformation is a two-dimensional function, $p(z, \theta)$, or a projection. The set of projects over all θ constitutes a sinogram. When a CT scan is conducted, the x-ray attenuation measurements form a data set that is, in fact, a sinogram.

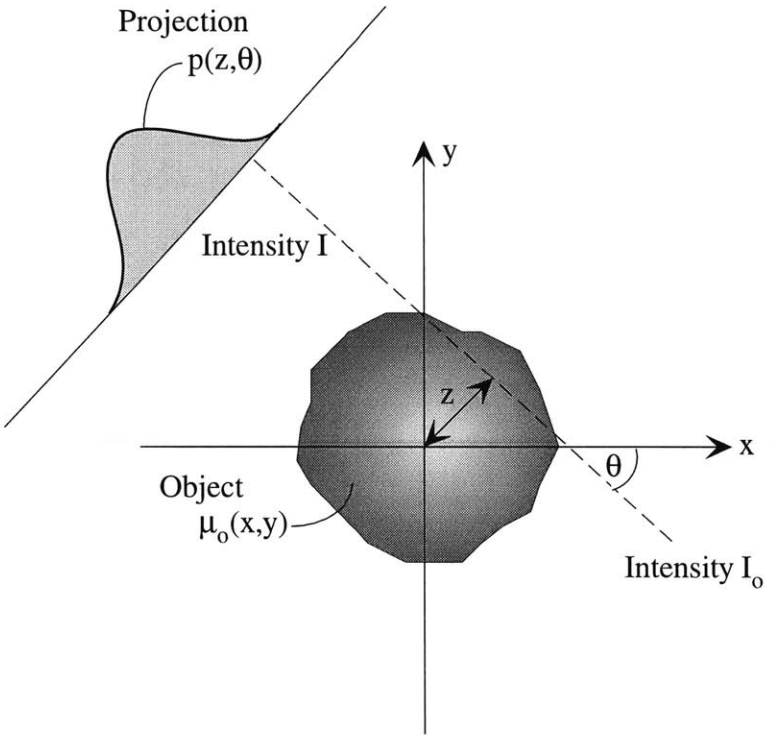

Figure 2-3: Coordinate systems for CT image reconstruction.

Using the sinogram, it is necessary to solve the inverse of the Radon transform to return information about the object in the (x,y) coordinate system. The inverse Radon transform is found by first taking the Fourier transform of Equation 2.7:

$$P(w_z,\theta) = \int_{-\infty}^{\infty}\int_{-\infty}^{\infty}\int_{-\infty}^{\infty} \mu_o(x,y)\delta(x\cos\theta + y\cos\theta - z)e^{-iw_z z}\,dxdydz$$

$$= \int_{-\infty}^{\infty}\int_{-\infty}^{\infty} \mu_o(x,y)e^{-iw_z(x\cos\theta + y\sin\theta)}\,dxdy$$

$$= M(w_x, w_y) \qquad 2.8$$

The result of Equation 2.8 is known as the central slice theorem. It states that the one-dimensional Fourier transform of the sinogram is equal to the two-dimensional Fourier transform of the map of the object. The function $\mu_o(x,y)$ is now obtained by taking the two-dimensional inverse Fourier transform of $M(w_x, w_y)$:

$$\mu_o(x,y) = \frac{1}{4\pi^2}\int_{-\infty}^{\infty}\int_{-\infty}^{\infty} M(w_x,w_y)e^{i(w_x x + w_y y)}\,dw_x dw_y$$

$$= \frac{1}{4\pi^2}\int_{0}^{2\pi}\int_{-\infty}^{\infty} P(w_z,\theta)e^{iw_z z}|J|\,dw_z d\theta \qquad 2.9$$

where $|J|$ is the Jacobian of the transformation from (w_x,w_y) to (w_z,θ), and is equal to $|w_z|$. The Radon transformation is summarized as:

$$\mu_o(x,y) = \frac{1}{\pi}\int_0^{\pi} F^{-1}\{P(w_z,\theta)\cdot|w_z|\}d\theta \qquad 2.10$$

where F^{-1} is a shorthand notation for the inverse Fourier transform. The integration defined by Equation 2.10 is known as a backprojection. A backprojection for the linear attenuation coefficient, $\mu_o(x,y)$, can be found through five steps (Budinger and Gullberg, 1974):

1. obtain the sinogram, $p(z,\theta)$, experimentally
2. obtain $P(w_z,\theta)$ by taking the z-axis Fourier transform of $p(z,\theta)$
3. filter $P(w_z,\theta)$ using a filter-function $|w_z|$
4. obtain the inverse Fourier transform of the result
5. backproject the result.

This process is known as the filtered backprojection (FBP) algorithm. Use of a filter, indicated in step 3, compensates for blurring that results if only a standard backprojection is performed. The inverse of the Radon transform can also be obtained by applying one of several mathematical methods, including summation, series expansion, and analytical solutions. However, in the majority of today's commercial CT scanning and reconstruction equipment, the FBP algorithm is the method of choice because of its

efficient hardware implementation, flexibility, robustness, and model application ability (Schneberk et al., 1990).

The mass attenuation coefficient of a material is nearly constant for x-rays of high energy, as seen in Figure 2-4 for some selected materials. As a result, once the linear attenuation coefficient is found through solution of the inverse Radon transform, the density distribution through the object follows from Equation 2.4.

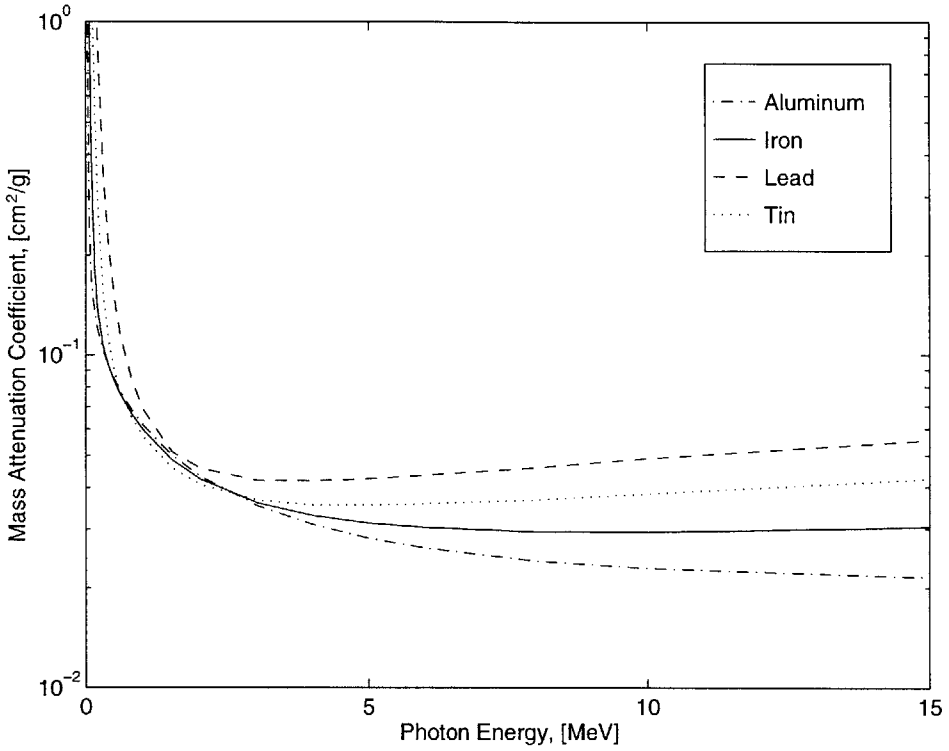

Figure 2-4: Mass attenuation coefficient as a function of x-ray energy for selected materials.

2.2 Design and Implementation

A typical CT system consists of six components: a radiation source; a radiation detector or detectors; a motion/position system; an operations console; control and processing software; and a test specimen, otherwise know as a phantom (Burstein, 1990). As CT systems developed over time, so did multiple equipment configurations. Although each has its own advantages, successive generations of scanners have improved upon prior shortcomings, primarily by decreasing the data acquisition time. For example, a first-generation system consists of a single radiation source and a single detector. The x-rays are collimated into a thin pencil-beam. This requires both rotation and translation in order to acquire a complete set of attenuation measurements through the object. In a third-generation system, an array of

multiple detectors is used and the x-rays are collimated in a fan-beam configuration, thus eliminating the need for translation in the data acquisition routine. Higher generation systems often involve multiple detector arrays and multiple radiation sources to further decrease data acquisition time.

The CT sensor developed in this work is a modified third-generation rotate-only system.[1] The radiation source is a 6 MeV x-ray linear accelerator with the x-ray beam collimated into a 30° fan shape. The detector array is composed of scintillation detectors arranged along an arc. To simplify the system design, a position system was chosen to move the phantom within a fixed linac-detector arrangement, rather than rotate the entire linac-detector array in synchrony about a fixed phantom. The positioning system consists of a rotary stage and translational stage mounted in position between the linac x-ray head and the detector array. A custom software application written in C++ controls the system on a PC-compatible computer. The following three sections describe in detail each of the CT system's main equipment components.

2.2.1 Linear Accelerator

The x-ray linear accelerator in the CT sensor is a field-portable MINAC 6 model manufactured by Schonberg Corporation (Santa Clara, CA). The unit can deliver a dose of 300 R/min at 1 m. The linac comprises a standing wave electron linear accelerator (x-ray head), a flexible RF waveguide, an RF head, a power supply/modulator unit, a water circulation unit, and a control console assembly. Figure 2-5 is a schematic of the components. Although the system is field portable, all components were either mounted or fixed in position. Each of the linac components is described in detail in Appendix A.

The x-rays produced by the linac are not monoenergetic. Instead, they range in intensity in a bremsstrahlung spectrum with a maximum of 6 MeV. The average x-ray energy is 1.3 MeV. The spot size is 2 mm. The linac operates in a pulsed-mode, producing x-rays in 5 μs bursts with a frequency of 180 Hz. The x-rays are collimated in a 30° cone beam. Additional collimation was added to reduce the x-ray beam to a 30° fan beam configuration. The theoretical beam height at the detectors is 20 mm in size. This corresponds to a theoretical beam height of 10 mm in the center of the CT field. The actual beam height in the center of the CT field was experimentally determined to be 4.5 mm, as discussed in Section 2.3.3.

---

[1] Although the system is a rotate-only design, in reality data acquisition is performed using both translation and rotation. This is done to increase the effective spatial resolution and is discussed in Sections 2.3.1 and 3.3.

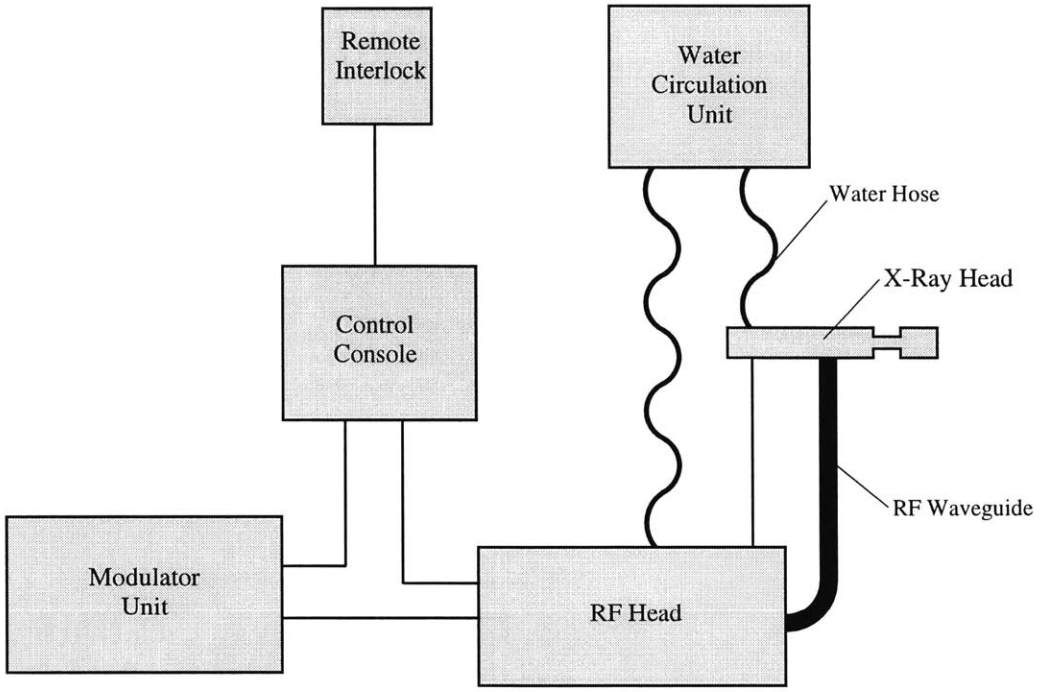

Figure 2-5: Schematic of the linear accelerator components and interconnections.

2.2.2 Detector Array

The data acquisition system consists of an array of 128 detectors, arranged on an arc with a radius of 845 mm, and associated signal acquisition electronics. Analogic Corporation (Peabody, MA) manufactured the basic system; proprietary customizations were done for this CT application. Each detector consists of a cadmium tungstate ($CdWO_4$) scintillation crystal coupled to a semiconductor photodiode. Each crystal is 20 mm high, 1.8 mm wide, and 3 mm deep, with 1.8 mm space between each detector along the arc. The detectors operate by converting x-ray energy into a proportional amount of visible light. The diodes then convert this light to a current proportional to the deposited energy. The data acquisition electronics (six signal acquisition boards, one timing board, one digital I/O board, and one frame grabber board) integrate the current, which then is recorded using custom-developed software on a PC-compatible computer (Jureidini, 1998). The data acquisition electronics are powered using two 5 V and two 15 V power supplies. Figure 2-6 shows the detector array mounted in position.

One shortcoming of a high-energy x-ray CT system is the large amount of scattered radiation that is produced when the primary x-rays interact with an object. When detected, scattered radiation degrades a CT image through blurring and reduced contrast. In the current system, the top and bottom of the array are shielded with a 57 mm thickness and a 45 mm thickness of lead, respectively, to reduce the amount of

scattered x-rays. In addition, tungsten alloy collimator plates, 20 mm high by 1.8 mm wide by 80 mm long, are mounted in front of the array between adjacent detectors. The density of the alloy is 17.5 g/cm^3. These "anti-scatter" plates focus the primary x-rays by reducing the scattered x-rays in the plane of the fan-beam. Jureidini (1997) performed a comprehensive study of the scatter reduction of the tungsten alloy plates. Figure 2-7 shows a close-up of the lead shielding and the tungsten alloy anti-scatter plates.

In addition to the 128 detectors located along the array, a set of 64 detectors is positioned directly behind the x-ray head of the linac, out of the primary x-ray beam. The signal measured by these detectors is not attenuated by any intermediary and thus provides an independent measure of the output intensity of the linac during operation. This measure is used to tune the linac to achieve peak performance during a CT scan.

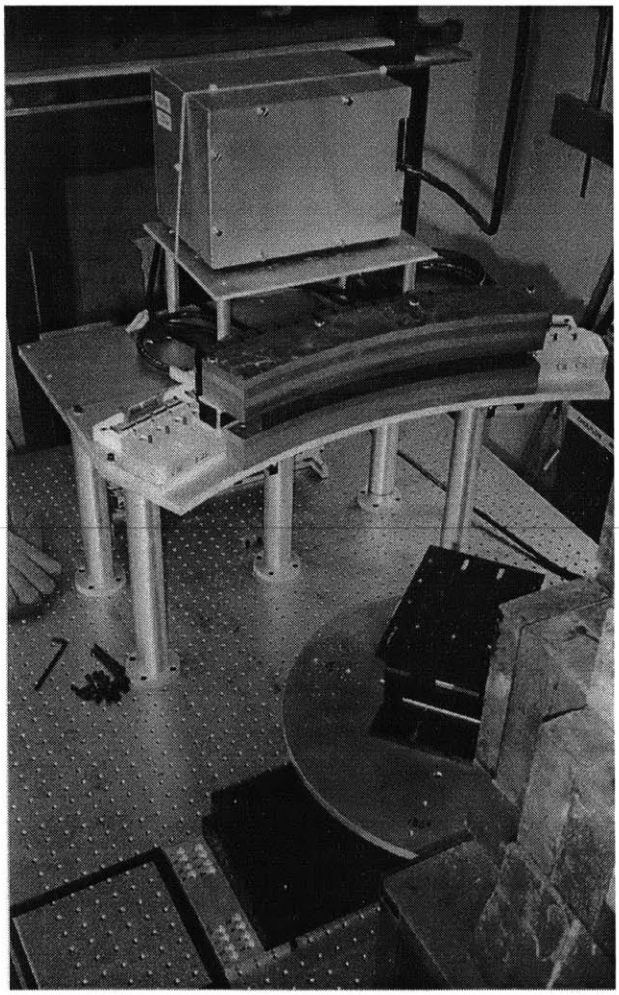

Figure 2-6: The 128 channel $CdWO_4$ detector array. The box behind the array contains the associated electronics for the data acquisition system. Note the positioning system visible in the lower right of the picture.

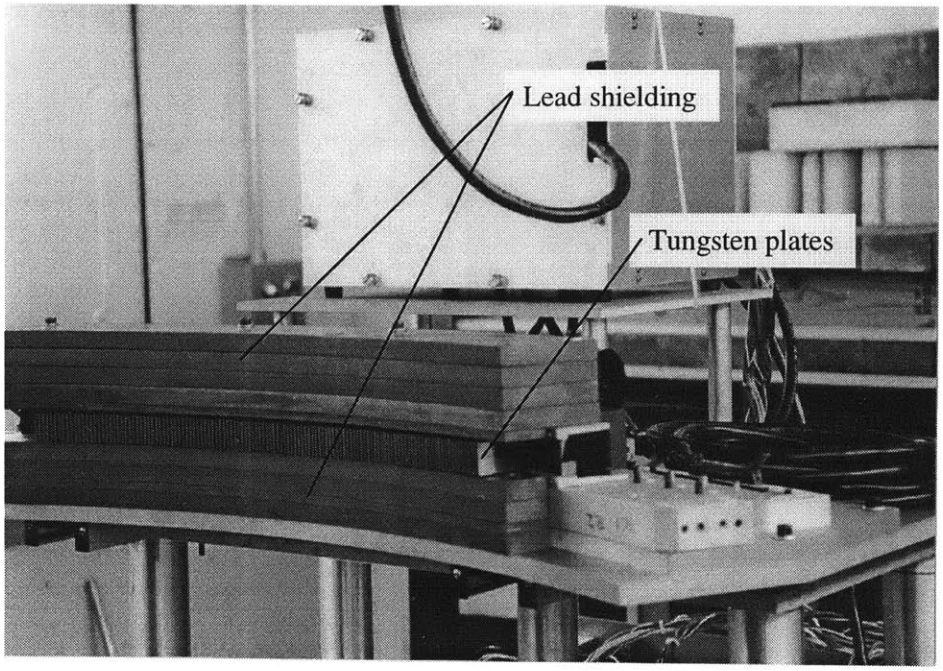

Figure 2-7: Lead shielding and tungsten alloy anti-scatter plate components of the detector array.

2.2.3 Positioning System

Acquisition of x-ray attenuation data for CT requires the phantom to move relative to the fixed-position linac and detector array. Two stages are used for this purpose. The positioning system is composed of a motorized rotary table mounted to a motorized horizontal translation table, as shown in Figure 2-8. The rotary table is a RT-12-SM model manufactured by New England Affiliated Technologies (Lawrence, MA). The rotary stage has a 305 mm diameter platform that supports a maximum load of 180 kg. A 5 V stepper motor operating at 200 steps per revolution drives the table. The horizontal translation stage is a HM-2400-SM model, also manufactured by New England Affiliated Technologies. The translational stage has maximum travel of 610 mm and supports a maximum load of 1000 kg. Two 5 V stepper motors operating at 200 steps per revolution drive both tables. Both motorized stages were operated in an open-loop mode using a pcStep4a model control card and amplifier, manufactured by nuLogic, Inc., (Newton, MA), and a PC-compatible computer. The rotary stage moves 1.0° for every 1000 motor steps. The minimum angular step size is 0.01°, with a maximum accuracy of 3.0 minutes and a maximum repeatability of 0.3 minutes. The translational stage moves 1 mm for every 1000 motor steps. It has a maximum resolution of 0.01 mm.

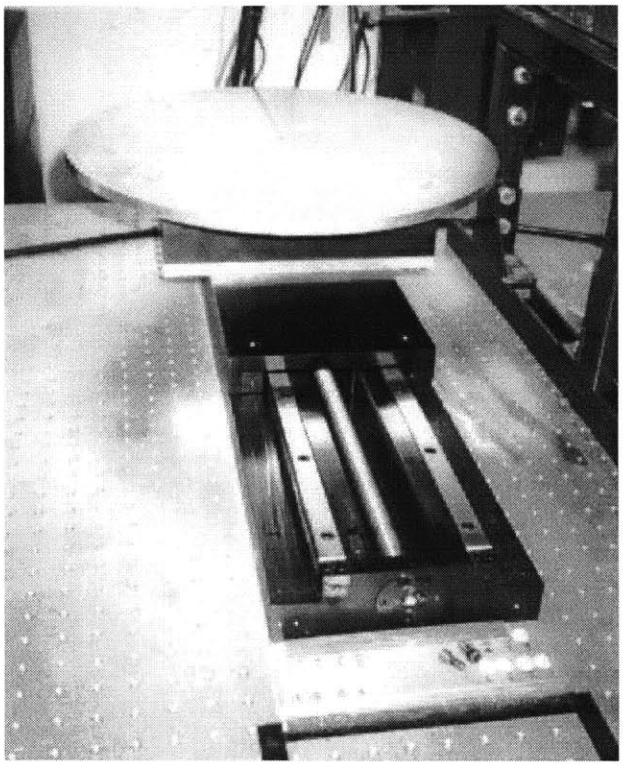

Figure 2-8: The positioning system of a rotary stage mounted on a linear translational stage.

2.2.4 System Layout

Figure 2-9 shows a top view of the final arrangement of the components of the CT system. As discussed previously, the CT system has a fixed x-ray source and detector array. When CT scans are conducted, it is the phantom that is rotated within the 30° x-ray fan beam. The linac x-ray head, detector array, and positioning system are mounted on a 1.25 m by 2.5 m by 210 mm rigid optical table, model 07OTN002 manufactured by Melles Griot (Irvine, CA). Each component is precisely positioned and aligned on a uniform datum surface. The optical table has a high-load capacity of 2500 kg with a deflection of less than 1.5 μm per 113 kg. Because vibration is not a concern, non-damping, rigid supports are used to elevate the optical table.

The x-ray head is the only component of the linac to be mounted on the optical table. It was elevated and leveled in place using a steel channel structural assembly. The RF head is positioned underneath the optical table directly below the x-ray head to minimize the length of the RF waveguide. The remaining components of the linac are near the x-ray head, away from the optical table.

Because the detector array is mounted on a permanent arc, the focal point is fixed at 845 mm. As a result, the detector array is positioned 845 mm away from the x-ray head target. When the collimators for both the source and detectors are taken into account, 546 mm of clearance remain. The detector array

is mounted on two linear rails, which allow the array to be moved toward or away from the x-ray head for precise focusing. The linear rails also allow the detector array to be moved back to accommodate a large phantom. The centerline of the x-ray head and the centerline of the detector array are mounted in-line, 565 mm above the surface of the optical table.

The positioning stage is mounted so that the center of rotation is 500 mm away from the x-ray head target. The positioning stage has a height of 187 mm. When mounted to the optical table, the x-ray beam is approximately 378 mm above the surface of the positioning stage. The positioning stage is oriented so that the linear table's direction of motion is perpendicular to the centerline from source to detector.

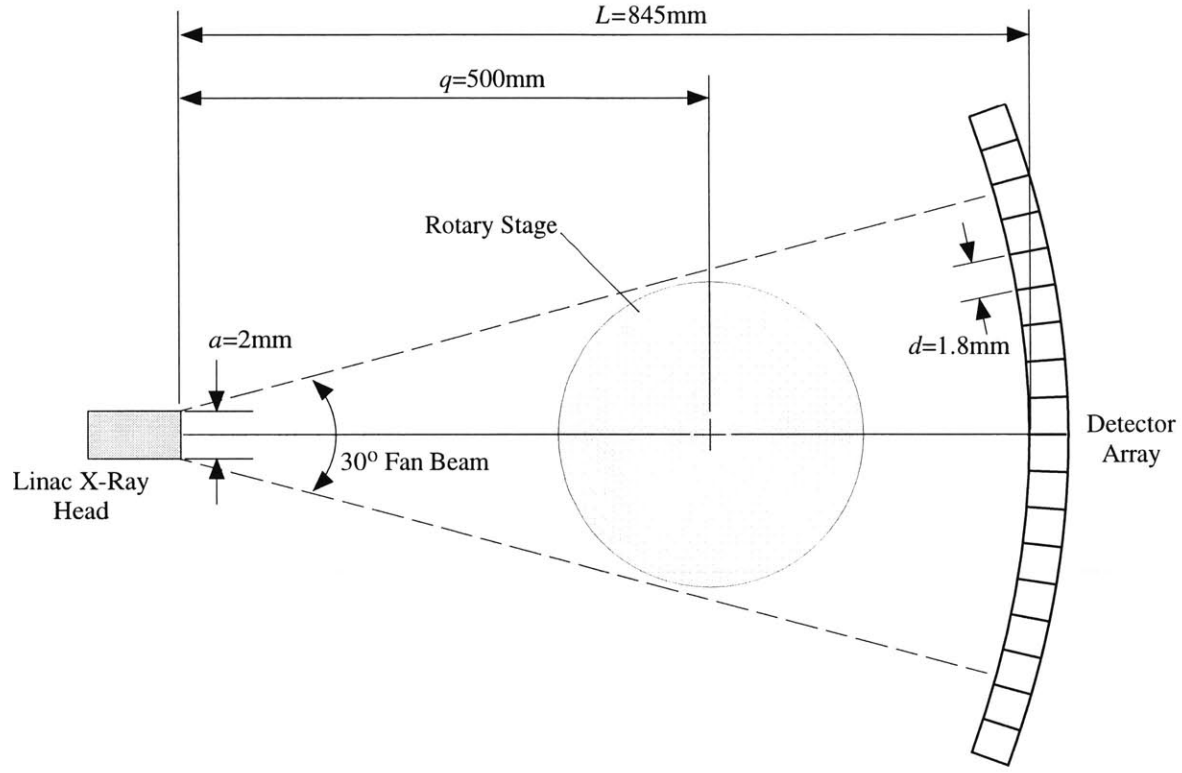

Figure 2-9: Dimensional layout of the CT sensor.

2.3 CT Sensor Performance Characteristics

The primary performance specification of a CT system is the ability to detect a defect or anomaly within an object of interest, be it a tumor in a human being, a crack in a turbine blade, or a density deviation in a solidification process. Detection is linked directly to the overall quality of the CT image, in addition to how well the image accurately represents the properties of the real object. The quality of the

CT image is defined by four main parameters: data acquisition speed; spatial resolution; contrast resolution; and noise (Burstein, 1990; Ross and McQueeney, 1990; Copley et al., 1994). Since these parameters are not mutually independent, performance trade-offs must often be made based on individual system needs. In general, those factors that increase spatial resolution also increase noise and decrease contrast resolution. For the CT system developed in this work, the performance goals are to acquire a CT image in 1 second (near real-time) with the ability to resolve a feature of 1 mm with a 1% contrast resolution.

2.3.1 CT System Operation

A CT scan consists of measuring x-ray attenuation at each detector during a 360° rotation of the phantom. The rotation lasts one minute, during which time 2700 measurements are made at each detector. Data acquisition begins with a 360° clockwise rotation. Then, the phantom is shifted perpendicularly to the beam direction by 0.9 mm, or half the width of a detector. The phantom is then rotated 360° counter-clockwise during which time another 2700 measurements are made. The attenuation data acquired during the two rotations (one clockwise, one counter-clockwise with shift) is interlaced. The result is equivalent to acquiring data over 360° using twice the number of detectors. In this case, the technique yields a data set from 256 detectors rather than 128. The procedure takes two minutes.

It is sufficient to use the attenuation data from a single rotation to reconstruct a CT image. However, offsetting the phantom, acquiring a second rotational data set, and combining the data nearly doubles the spatial resolution of the system. The increase in spatial resolution more than compensates for the increase in data acquisition time. Once the attenuation data is acquired, a FBP fan-beam algorithm with a ramp filter and a high cutoff frequency reconstructs the CT image. Typical image reconstruction time ranges from 5 seconds to 60 minutes, depending on the final image size. The reconstruction algorithm uses an experimentally-acquired attenuation curve to reduce image artifacts introduced by beam hardening. The curve equals the x-ray attenuation through an aluminum wedge with thickness ranging from 1 mm to 300 mm. Detailed information on the CT image reconstruction algorithm and related software can be found in Jureidini (1998).

2.3.2 Planar Spatial Resolution

The planar spatial resolution, or spatial resolution, of a CT system describes the ability to distinguish between two closely spaced features within the plane of the CT image. It is the scale on which shapes in a CT image are faithful reproductions of the actual object. Spatial resolution is determined primarily by the size of the x-ray source spot, the collimation of the detector, and the scanner geometry. Accordingly, a specific geometric configuration defines the spatial resolution of a CT system.

The mechanical accuracy of the positioning system also contributes to the spatial resolution. An image cannot be reconstructed to an accuracy greater than that of the positioning mechanism. The theoretical spatial resolution, r, of a CT system can be determined using the geometric relation defined by Sivers and Silver (1990):

$$r \cong \frac{\sqrt{d^2 + \left[a\left(\frac{L}{q} - 1\right)\right]^2}}{\left(\frac{L}{q}\right)} \qquad 2.11$$

where a is the x-ray source spot size, d is the detector width, L is the distance from source to detector, and q is the distance from source to the imaging point. For this CT system, a=2 mm, d=1.8 mm, L=845 mm, and q=500 mm, as shown previously in Figure 2-9. Using the geometric parameters of the system in Equation 2-11, the theoretical spatial resolution was:

$$r \cong 1.338 \text{ mm}$$

Experimentally, the spatial resolution is visualized by using a phantom with slots or holes of controlled width or diameter. The resolution is defined as the smallest dimension that can clearly distinguished. The resolution capability of this system was demonstrated by using a rectangular phantom made of aluminum with holes ranging in diameter from 2.9 mm to 1.0 mm. Figures 2-10a and 2-10b show a photograph of the phantom and a schematic of its dimensions, respectively. The holes in the phantom pass completely through the thickness of the aluminum block. The exception is the 1.4 mm diameter hole, which is filled with a steel insert. Figure 2-10c is a CT image of the block phantom. The image size is 512 by 512 pixels, which represents a scaling of 0.53 mm/pixel. The pixel intensity was scaled to correspond with density so that the aluminum block has a value of 2.7 g/cm^3. Dark regions represent areas of lower density and bright regions represent areas of higher density. As seen from the CT image, all the holes are visible. Also visible is the steel insert, as indicated by the bright spot.

Although even the smallest hole is visible in Figure 2-10c, this does not necessarily mean that the true spatial resolution of this CT system is 1.0 mm. To quantitatively determine the spatial resolution, the point-spread function (PSF) of a uniform object with a thickness less than the pixel size is often used. The PSF can be determined by scanning an object such as a wire perpendicular to the image plane. The width of the PSF function at half its maximum (FWHM) provides an estimate of the image sharpness, and thus spatial resolution. In practice however, it is difficult to acquire a PSF because "point" objects always have some finite width. As an alternative, the line spread function (LSF) can be used. The one-

dimensional profile of a circularly symmetric PSF is equivalent to a profile taken perpendicular to the two-dimensional response of a LSF (Sivers and Silver, 1990). The LSF is well approximated by the derivative of the response of the system to an edge (ERF).

To determine the LSF, a CT image of an aluminum cylinder (100 mm OD) was acquired. The image is shown in Figure 2-11a. The image pixels were scaled such that the calculated density of the aluminum was 2.7 g/cm^3. Plotting the calculated density versus position through the center of the phantom generated the ERF, shown in Figure 2-11b. To reduce noise, the ERF was composed of an average of 360 profiles through the phantom. Taking the derivative of the ERF produces the LSF, shown in Figures 2-11c and 2-11d. The FWHM, indicative of the spatial resolution of the system, was found to be 1.76 mm.

Since spatial resolution is a function of geometry, resolution can conceivably be improved by changing the configuration of a CT system. In the current setup, neither the spot size of the x-ray head nor the width of the detectors can be modified without significant cost. Thus, the easiest alteration to make is the source-detector and source-object spacing. Figure 2-12 shows a plot of the theoretical spatial resolution as a function of the ratio between source-to-detector and source-to-object distance. The results show that the maximum theoretical spatial resolution for this CT system is approximately 1.338 mm at a geometric distance ratio (L/q) of 1.69. The actual distance ratio of this system is already 1.69 mm. Consequently, there is little to no room for additional spatial resolution improvement by modifying the system configuration.

The design goal for the spatial resolution of this sensor was 1.0 mm. However, equipment parameters such as the x-ray and detector spot size constrain the maximum theoretical spatial resolution to 1.338 mm at best. The actual spatial resolution was found to be 1.76 mm, worse than the predicted spatial resolution by roughly 0.42 mm. A wide range of factors contributes to this degradation. They include, but are not limited to, the detection of erroneous scattered radiation, long and short-term variations in the linac intensity, noise in the detected signal, and artifacts in the CT image. In addition, the smallest misalignment between the x-ray source and the detector array can affect the fan beam focus and reduce resolution. Although the design goal of 1.0 mm was not achieved with the current hardware and configuration, it may be possible to approach the theoretical limit for spatial resolution with more diligent alignment of the source and detector array and further collimating against scattered radiation.

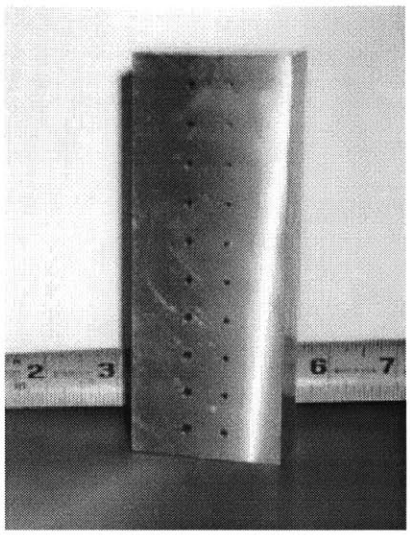

(a)

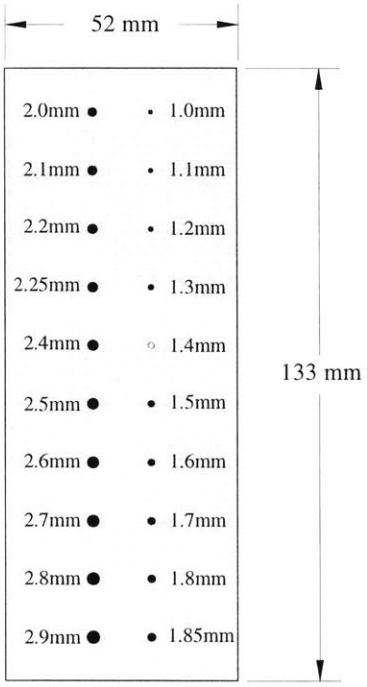

(b)

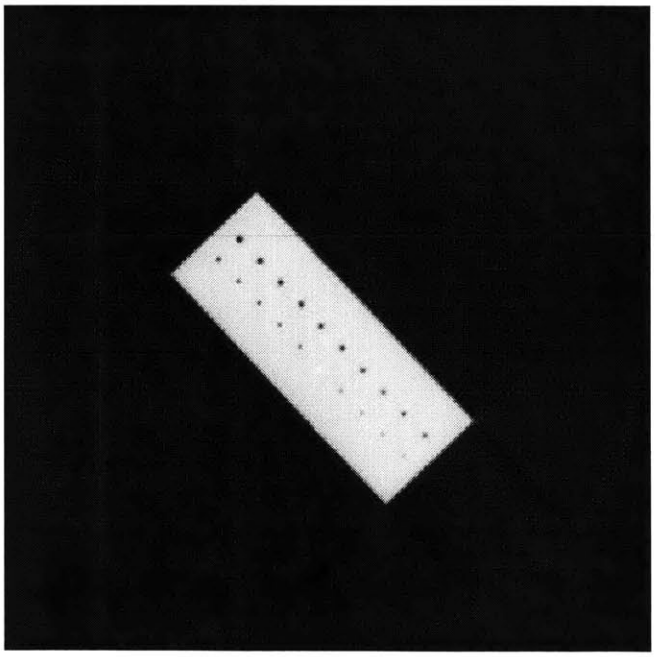

(c)

Figure 2-10: (a) The aluminum block phantom. (b) Schematic of the aluminum block phantom showing hole dimensions. (c) CT image of the aluminum block phantom.

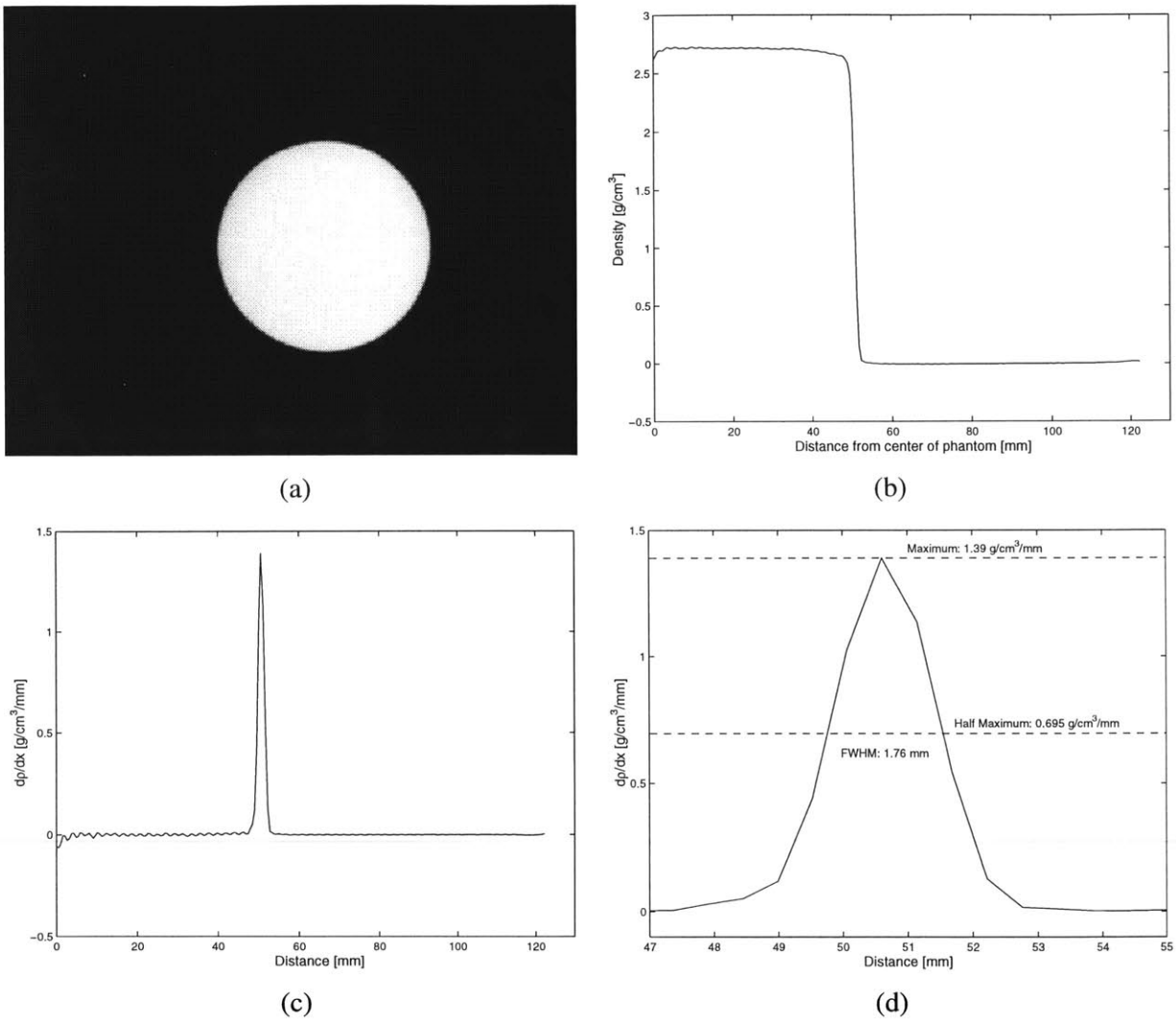

Figure 2-11: (a) CT image of aluminum cylinder phantom. (b) Edge response function (ERF) for the aluminum cylinder. (c) Line spread function (LSF) for the aluminum cylinder. (d) LSF showing the full width at half-maximum (FWHM).

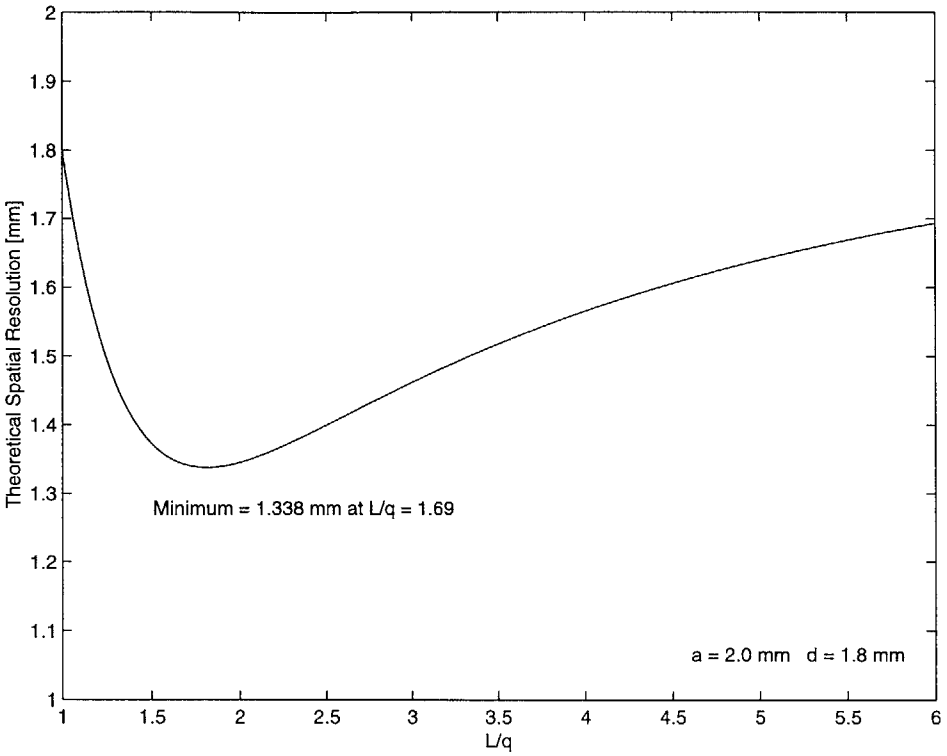

Figure 2-12: Theoretical spatial resolution for CT system for various source-detector (L) and source-object (q) distances, with x-ray spot size and detector width held fixed.

2.3.3 Vertical Spatial Resolution

The vertical spatial resolution, or CT slice thickness, is defined by the beam height at the center of the field of view. As mentioned in Section 2.2.1, the x-ray source was collimated to achieve a beam height of 10 mm, i.e. a 10 mm slice thickness. For a two-dimensional CT system, the slice thickness defines the distance over which vertical features are averaged in the resulting CT image.

The slice thickness was experimentally measured by reconstructing a CT image of a rectangular aluminum block with a cavity machined in the interior. The block measures 127 mm long by 76 mm wide by 51 mm high. The cavity is 108 mm long by 57 mm wide by 0.5 mm deep. Figure 2-13 shows the CT image of the aluminum block. The difference in density between the solid aluminum region and the cavity region is merely the depth of the cavity divided by the slice thickness. For a predicted slice thickness of 10 mm, the density difference was expected to be 5%. However, the image actually revealed a density difference of 11%. By dividing the cavity depth by this density difference, the corresponding actual slice thickness was found to be 4.5 mm. This is significantly better than the 10 mm predicted slice thickness based on the collimator design.

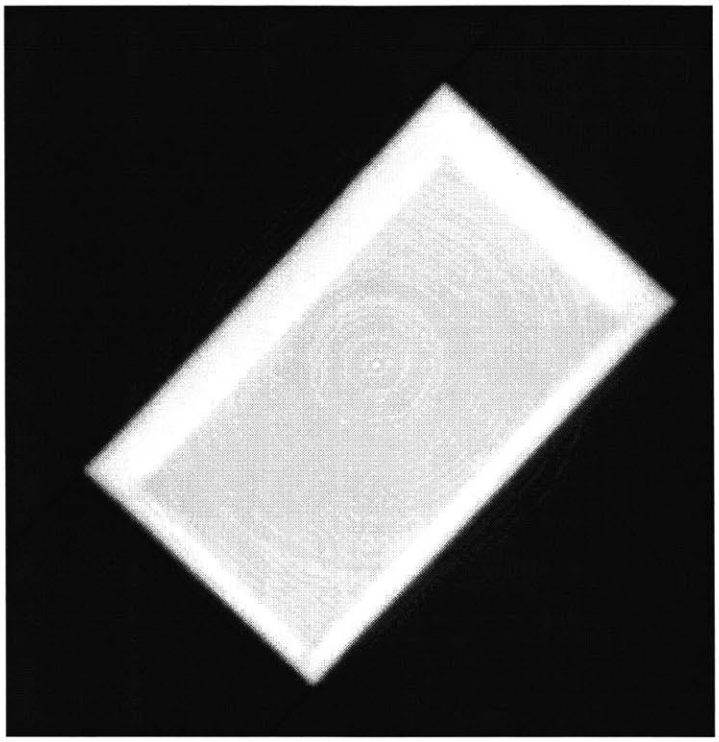

Figure 2-13: CT image of aluminum block with interior cavity.

2.3.4 Contrast Resolution/Noise

Contrast resolution is the ability of a CT system to faithfully reproduce material variations in an object. It is a function of the variation between the linear attenuation coefficients of two different materials. In the simplest sense, contrast resolution is a measure of the overall noise of an image. If the noise in an image is 2%, then the maximum density difference that can be resolved is 2%. Some form of noise is present in all CT imaging systems.

The average variation in the detected x-ray signal of this CT sensor was originally approximately 2%. Several sources caused this noise. One component was the pulse-to-pulse variations in the x-ray output of the linac. Replacing the original DC electron gun supply with a more stable controller lowered the detected signal variation to approximately 1%. A second component was a 60 Hz variation contributed by the electrical noise in the power lines. Pulsing the linac with an external trigger operating on a phase-locked circuit at approximately 180 Hz lowered the noise in the detected signal to approximately 0.7%. The final technique involved averaging the x-ray measurement over every three pulses. This reduced the noise in the detected signal to between 0.1% to 0.2%. This noise level was deemed to be acceptable.

With the variation in the detected signal having been minimized, CT scans of a cylindrical aluminum phantom were performed to determine the general contrast resolution of the system. The phantom was patterned after the experiments conducted by Kropas et al. (1991). The phantom pictured in Figure 2-14a consists of an aluminum cylinder with nine holes. Each hole is filled with a cylindrical insert material with a density roughly near 2.7 g/cm^3. Figure 2-14b shows a schematic of the phantom and the inserts, with relevant dimensions. Figure 2-14c is a CT image of the cylinder phantom. The image size is 512 by 512 pixels, which represents a scaling of 0.53 mm/pixel. The pixel intensity was scaled to correspond with density so that the aluminum cylinder has a value of 2.7 g/cm^3. Dark regions represent areas of lower density and bright regions represent areas of higher density.

To determine contrast resolution, the pixel values and their variation in the aluminum cylinder region were measured. As defined by Burstein (1990), the contrast resolution, c, in percent, is:

$$c = \frac{N}{S} \times 100 \qquad 2.12$$

where N is the noise, usually given as the standard deviation of the pixel values, and S is the signal, usually given as the average of the pixel values over a selected area. The pixel values, which correspond to density, were found to have a mean value of 2.6996 g/cm^3 with a standard deviation of 0.0302 g/cm^3. Using Equation 2.12, the contrast resolution for this image was found to be 1.1%. This is very close to the design goal of 1.0%. It should be noted that the contrast resolution is a function of x-ray intensity. As such, it does vary from scan to scan and image to image. Consequently, the 1.1% contrast resolution in this experiment is a benchmark, not an absolute.

The computed density from the CT image was measured across several cross-sections. The cross-section locations are shown in Figure 2-15a. The density versus position for the four cross-sections is plotted in Figures 2-15b through 2-15d. The difference is well identifiable with materials that have a large density difference as compared to aluminum, such as alumina, boron nitride, and graphite. For materials such as aluminum silicate and glass mica, which have a density very similar to aluminum, the difference is not as apparent because of the contrast resolution limits. Table 2-1 shows the actual measured and computed density for each of the insert materials.

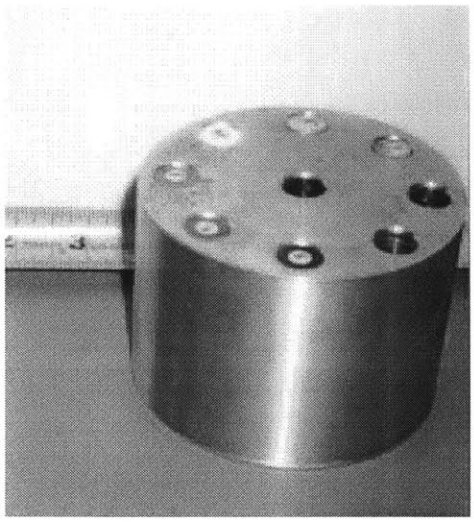

(a)

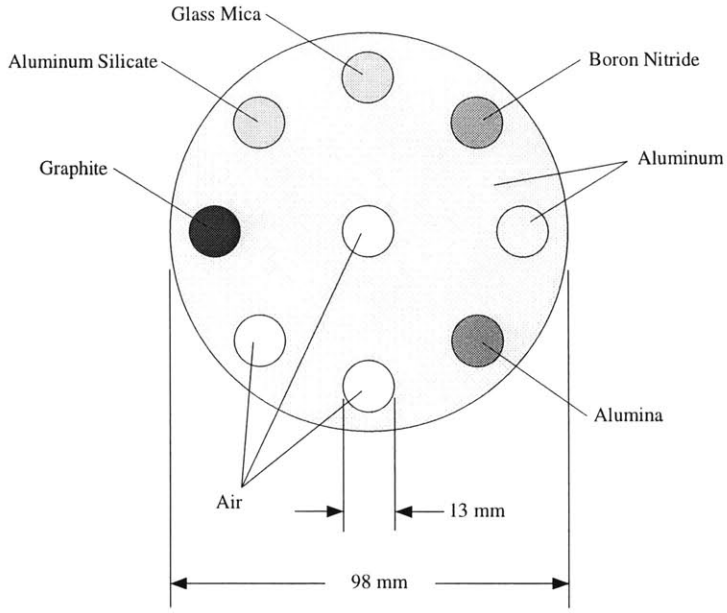

(b)

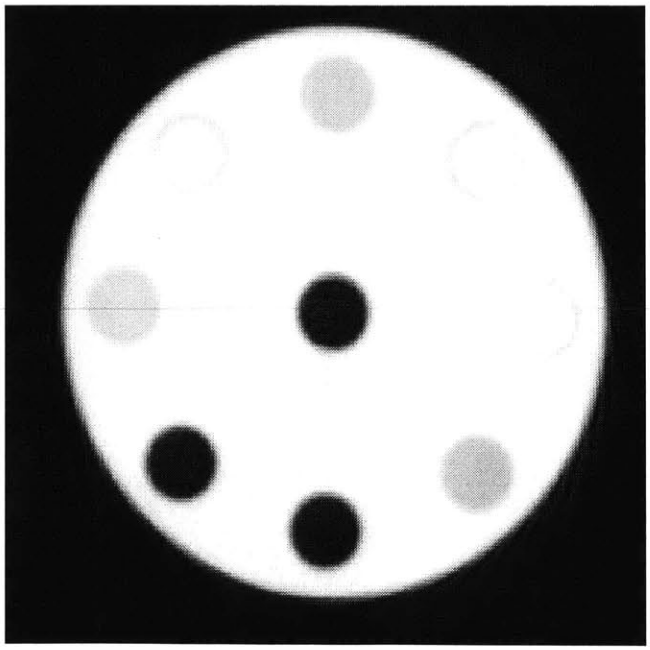

(c)

Figure 2-14: (a) The aluminum cylinder phantom with inserts. (b) Schematic of the aluminum cylinder phantom showing the various insert materials. (c) CT image of the aluminum cylinder phantom.

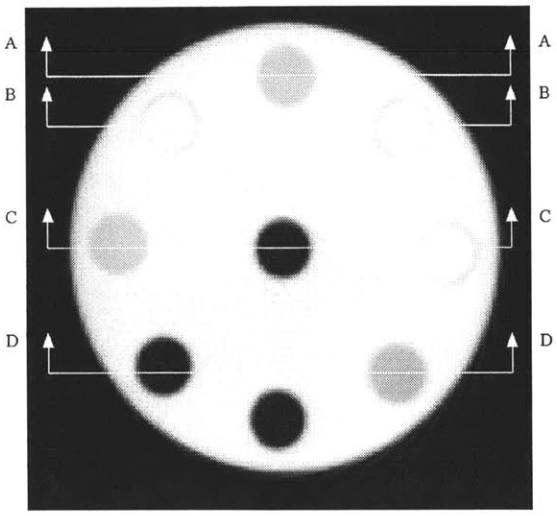

(a)

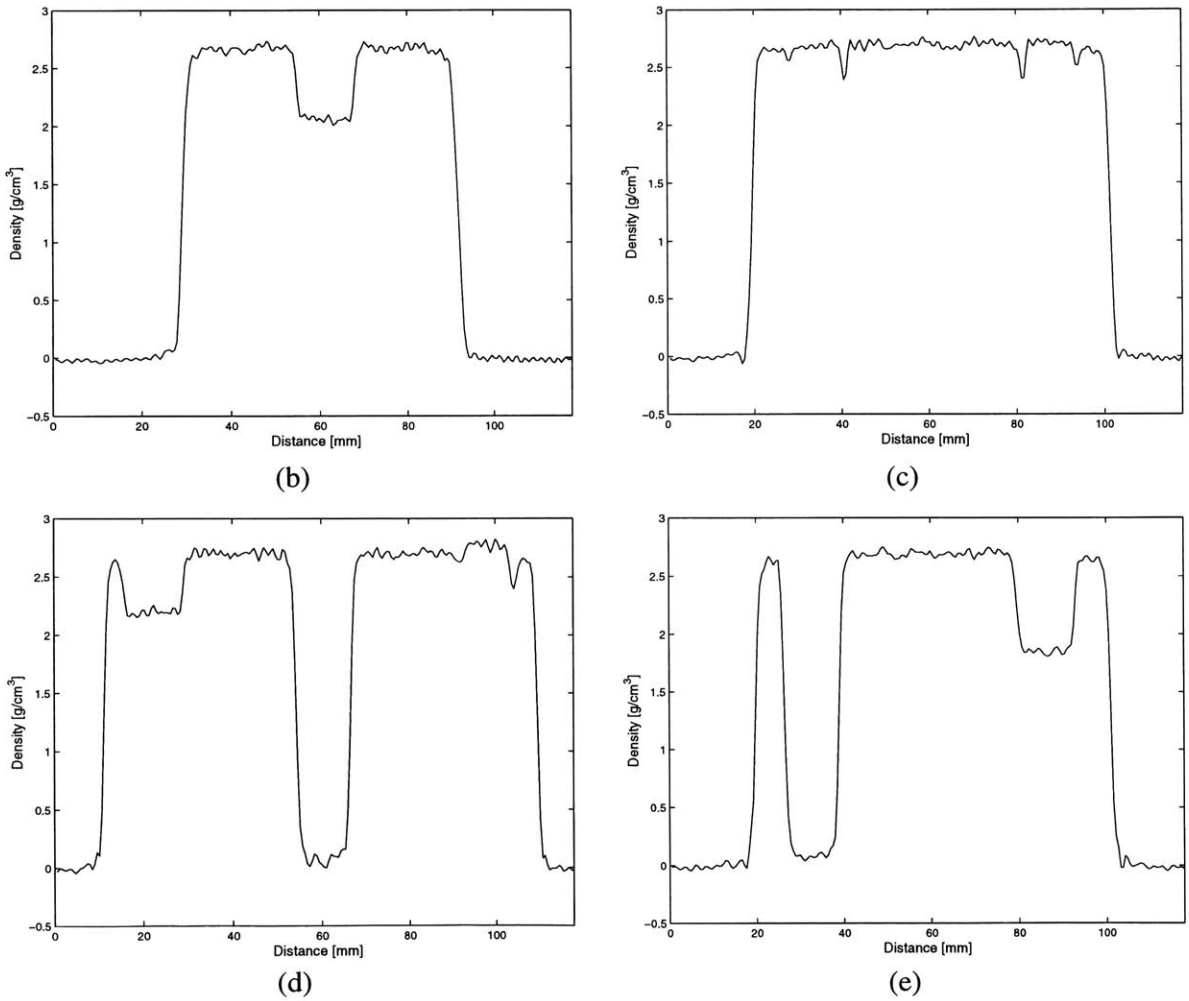

(b) (c)

(d) (e)

Figure 2-15: (a) CT image of aluminum cylinder phantom showing sections. (b) Computed density vs. position along line AA. (c) Computed density vs. position along line BB. (d) Computed density vs. position along line CC. (e) Computed density vs. position along line DD.

Table 2-1: Measured and computed densities of the various insert materials.

Material	Measured Density [g/cm^3]	Computed Density [g/cm^3]	Difference in Density from Aluminum
Alumina	2.13	2.19	21%
Aluminum	2.70	2.68	0%
Aluminum Silicate	2.70	2.77	0%
Boron Nitride	2.10	2.07	22%
Glass Mica	2.69	2.70	0.4%
Graphite	1.81	1.85	33%

2.3.5 Data Acquisition Speed

As noted earlier, the typical time required for a CT scan by this system is approximately 2 minutes. This is much longer than the design goal of 1 second. The choice of mechanical positioning system is the main reason for this underperformance. The rotary stage component of the positioning system uses a worm gear drive coupled to a stepper motor. The maximum reliable velocity at which the stage can be rotated is approximately 8°/sec. Although speeds up to 15°/sec are achievable, the performance of the rotary stage is not reliable. The worm gear component is prone to locking or jamming at higher speeds. As a result, the drive velocity was set at 8°/s so that the stage would operate reliably and consistently.

Although the current data acquisition speed does not meet the design criterion, the system does have the potential to acquire CT scans at a much higher rate. At the current rotary stage speed of 8°/s, attenuation data is collected at 2700 view angles. This represents an oversampling in the required number of views. As documented by Budinger and Gullberg (1974), if a reconstructed image is to be uniformly resolved to a resolution r of a completely unsymmetrical object of dimension D, the number of view angles required is:

$$n \geq \pi \frac{D}{r} \qquad 2.13$$

For this CT system, the field of view is approximately 268 mm. Assume a phantom of dimension D = 223 mm. Equation 2.13 predicts that at least 540 view angles are required to reconstruct an image with a resolution r = 1.3 mm. A data set of 540 view angles would correspond to a data acquisition speed of approximately 24 seconds and a rotary stage speed of 40°/s. Such speeds are feasible with an alternative positioning system, such as a high-velocity linear motor drive. This is still not near real time

performance, but nonetheless a dramatic improvement. However, one concern with operating at higher speeds is the introduction of inertial effects. These effects could be significant if the phantom is other than a solid, fixed object, such as a solidifying metal casting. Inertial effects could disrupt the phantom and distort interpretation of the CT image data. In addition, speeds higher than 40°/s may not be preferable since they may introduce artifacts because of angular undersampling, as predicted by Equation 2.13.

Figure 2-16 shows an example of how data acquisition speed affects image quality. Figure 2-16a shows a CT image of the aluminum block phantom from Section 2.3.2. The image was reconstructed with the full set of 2700 view angles acquired with the standard data acquisition speed and time, 8°/sec and 2 minutes, respectively. In Figure 2-16b, four out of every five views were removed from the complete data set. The image was reconstructed using only 540 view angles, corresponding to an acquisition speed of 40°/sec and an acquisition time of 24 seconds. One can see that there is little difference in image quality when compared to Figure 2-16a. This is because the data set of 2700 view angles is oversampled. In Figure 2-16c, the image was reconstructed using only one out of every fifteen view angles, 180 in total. This corresponds to an acquisition speed of 120°/sec and a data acquisition time of 8 seconds. Image integrity still holds, although signs of undersampling artifacts are beginning to appear. Figure 2-16d was reconstructed using only 60 view angles, representative of an acquisition speed and an acquisition time of 360°/sec and 2.7 seconds, respectively. The image is significantly degraded–both blurring and streaking are present due to angular undersampling in the data set.

There is a clear trade-off between image quality and data acquisition speed. This trade-off is a function of the number of x-ray photons that can be measured over a given period of time. Faster data acquisition speeds acquire fewer view angles, and thus x-ray photons. As a result, the FBP algorithm cannot correctly reconstruct the undersampled data. In the case of this system, data acquisition time could be reduced to approximately roughly 20 to 30 seconds by optimizing the positioning system. However, the image reconstruction algorithm is not well suited to handle data sets acquired in less than 20 seconds. Alternative algorithms, such as limited angle or laminography techniques, would be required to achieve real-time or near real-time performance.

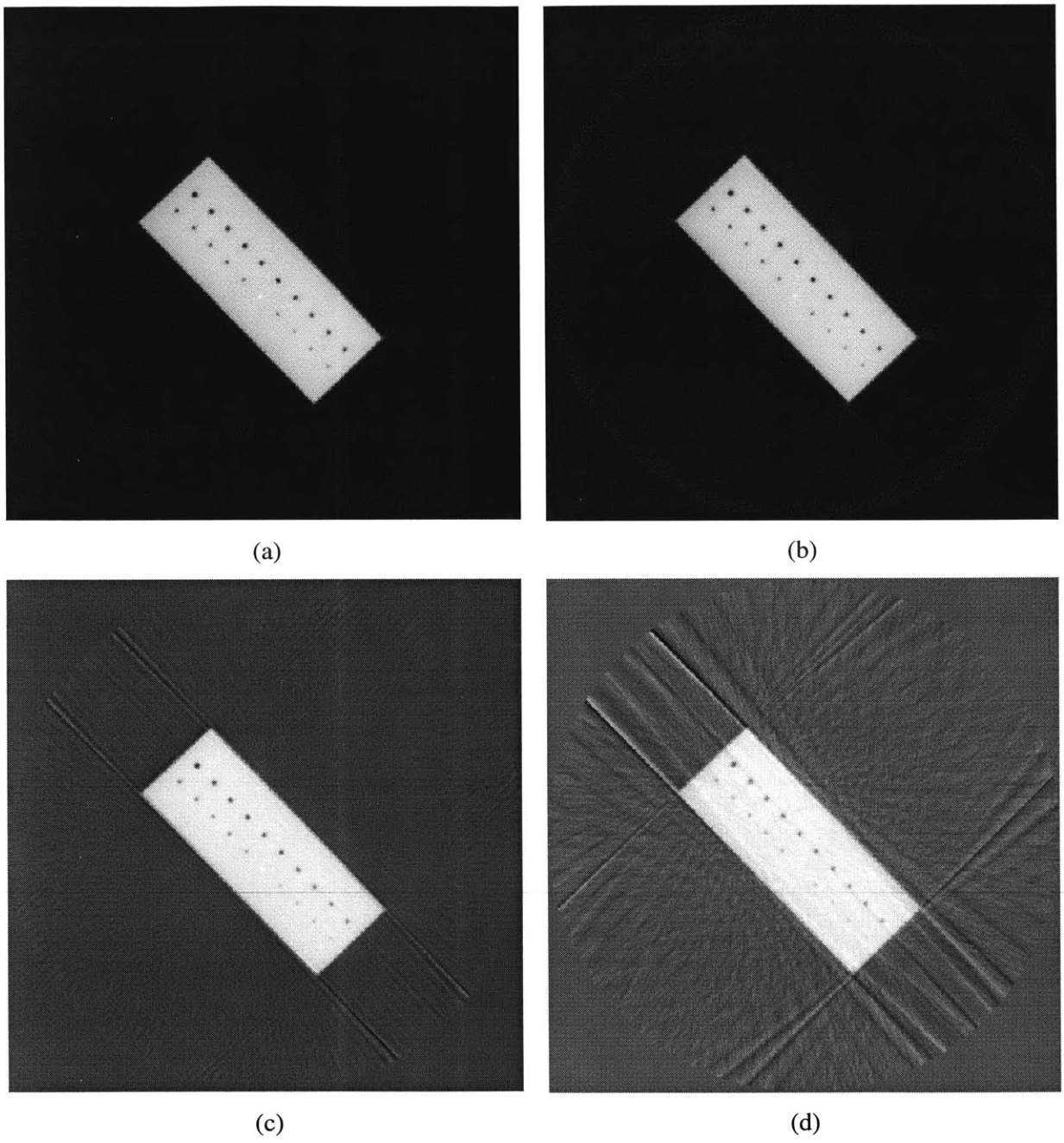

Figure 2-16: (a) CT image of block phantom reconstructed with 2700 view angles. (b) CT image of block phantom reconstructed with 540 view angles. (c) CT image of block phantom reconstructed with 180 view angles. (d) CT image of block phantom reconstructed with 60 view angles.

2.4 CT Sensor Performance Comparison

A sensor was developed to test the viability of CT as a method of detecting solidification in metals, as discussed in Section 1.4 during a prior feasibility study (Hytros, 1996). That sensor was a first-generation scanner with a Co^{60} radioisotope as the radiation source and a single NaI scintillation detector. The CT sensor documented here continues that work to develop an industrially-feasible system. Comparison of the performance of the two systems shows the magnitude of the improvement made. For the comparison, an identical phantom was scanned by both systems. The phantom was a steel cylinder with a tin-filled central cavity. The density of the steel and tin were 7.85 g/cm^3 and 7.3 g/cm^3, respectively. This is a difference of 7%. Figures 2-17a and 2-17b show the phantom and a schematic of its dimensions and composition, respectively.

The overall data acquisition took 12 days using the Co^{60}-based system. The flux from the source was very poor, only 2×10^3 photons/cm^2·s. Each individual measurement required 300 seconds to ensure that the statistical noise was insignificant. Figure 2-17c shows the reconstructed image. The spatial resolution is approximately 4 mm and the contrast resolution is approximately 3.4%. Although the steel and tin regions are discernable, the overall image quality is marginal.

In contrast, data acquisition using the linac-based system required only 2 minutes. There were two primary factors that contributed to the improved data acquisition speed. The photon flux from the linac is 8.4×10^9 photons/cm^2·s (Jureidini, 1997), six orders of magnitude stronger than the Co^{60} source. In addition, the linac-based system used an array rather than a single detector. Figure 2-17d shows the CT image acquired using the linac-based system. The differences are obvious. The spatial resolution is approximately 1.76 mm and the contrast resolution is roughly 1%. There are several reasons for the improvement, among which are better photon statistics resulting from the higher flux and better source and detector collimation.

It is evident that the current linac-based CT sensor is a dramatic improvement over the earlier Co^{60}-based system. The spatial and contrast resolutions are at or near the intended design goals. Although the data acquisition speed is not real-time, the system does operate at a reasonable rate and the possibility of future enhancement does exist. With its development and optimization having been completed, the next goal is to test the sensor's ability to identify the solid/liquid interface position during metal solidification.

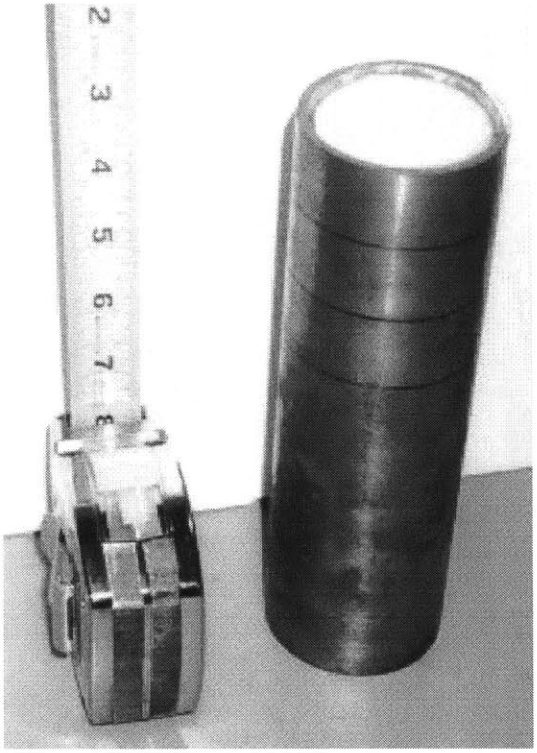

(a)

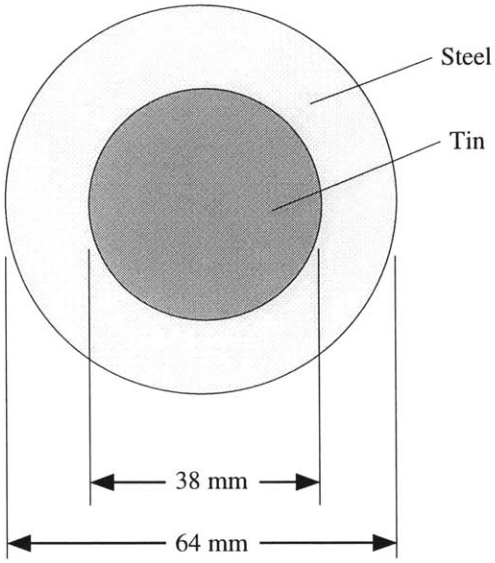

(b)

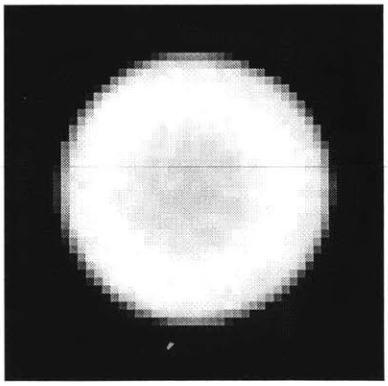

(c)

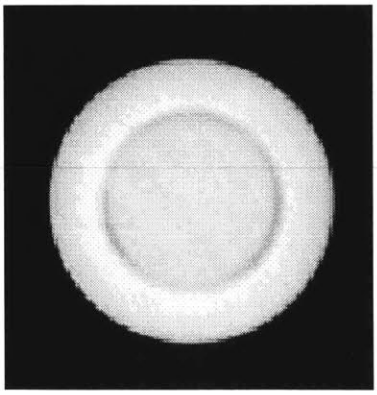

(d)

Figure 2-17: (a) The steel and tin cylinder phantom. (b) Schematic of the steel and tin cylinder phantom. (c) CT image of the steel and tin cylinder phantom using the Co^{60}-based system. (d) CT image of the steel and tin cylinder phantom using the linac-based system.

Chapter 3 Solidification Experiments: Pure Aluminum

3.1 Experiment Design

Because the goal of this work is to develop a CT-based sensor for monitoring the solidification phenomena in metals, it was necessary to construct a laboratory-scale system to simulate the casting process. This system, herein referred to as the solidification platform, contains several major components: a furnace; a crucible loaded with a charge of metal; a cooling unit; and a temperature recorder. It simulates the metal casting process by generating a solidification front inside a cast part with a cylindrical geometry. In contrast to most casting processes, however, this system produces a solidification front that originates in the interior of the metal and moves outward. This unorthodoxy simplifies the design of the solidification platform. The system was created for experiments using aluminum and aluminum alloys, although metals with similar or lower melting points can be used.

The primary component of the solidification platform was the 4700 W, 220 V furnace, model CC12-8x8M manufactured by Mellen Company, Inc. (Penacook, NH). Shown in Figure 3-1, the furnace has a top-loading design and a maximum operating temperature of 1200°C. The furnace is 489 mm high with a 508 mm OD with a bore of 280 mm depth with a 203 mm OD. The furnace uses an electric-resistance heater made of Fe-Cr-Al windings embedded in a ceramic holder. A layer of ceramic fiber insulates the exterior steel shell from the interior heating elements. A PID controller, a model UDC3000 manufactured by Honeywell Corporation (Fort Washington, PA), sets the operating temperature of the furnace. It monitors the air temperature using a K-type (chromel-alumel) thermocouple mounted inside the furnace bore, varying the power to the heating elements to maintain a constant setpoint.

A charge of aluminum is placed inside the furnace bore in a clay-graphite crucible. The cylindrical crucible is 238 mm high with a 178 mm OD and 150 mm ID. It serves as a mold during melting and solidification and accommodates up to 6 kg of aluminum. Boron-nitride ceramic coats the interior of the crucible to prevent corrosion from the molten aluminum. In addition, the crucible rests in a stainless steel carriage, which facilitates moving of the crucible in and out of the bore. Figure 3-2 shows the crucible mounted in the carriage.

A cooling unit generates and accelerates solidification of the aluminum inside the crucible. Shown in Figure 3-3, the cooling unit comprises a ceramic cover and a central airflow tube. During the course of an experiment, aluminum inside the crucible is heated in the furnace. The airflow tube is dipped into the center of the completely molten metal. The ceramic cover rests atop the crucible to provide insulation. Passing pressurized air though the tube cools the molten metal to generate an

outwardly moving solidification front. The airflow tube is annular, composed of an outer stainless steel tube (25.4 mm OD, 22.9 mm ID) and an inner stainless steel tube (15.9 mm OD, 14.1 mm ID). Air passes into the system via the inner tube and exits via the outer tube. A model V325 compressor, manufactured by Quincy Corporation (Quincy, IL) supplies the pressurized air, which is dried, filtered, and cooled to remove any contaminants. A needle valve and flow meter regulate the airflow rate. In addition, a thermowell-mounted thermometer measures the temperature of the incoming air.

The system operates in an open loop, whereby the air exiting the tube is merely vented to the atmosphere. An open-loop system is much simpler to implement than a recycled closed-loop cooling system. However, it limits the fluid media available for use. Fluids such as chilled water, argon, and helium were all considered because of their superior heat capacity over air. However, any other gas requires a closed-loop system that would have made implementation too difficult. In the case of chilled water, the risk of explosion in the event of a leak was too high.

An additional component of the cooling unit is the sixteen stainless steel thermocouple sheaths (3.2 mm OD) shown in Figure 3-3a. The sheaths are arranged in a radial pattern and pass through the ceramic insulation into the molten metal. Each sheath accommodates a K-type thermocouple (1.6 mm OD), as shown in Figure 3-3b. The thermocouples monitor the temperature within the aluminum and verify the position of the solidification front during cooling. The thermocouple temperatures are recorded using a PC-compatible computer and data acquisition board. The board is a model DAS-TC manufactured by Keithly-Metrabyte Company (Cleveland, OH).

A schematic of the complete solidification platform is shown in Figure 3-4. The system mounts on the rotary stage portion of the CT sensor's positioning system. The center of rotation of the solidification platform is about the centerline of the furnace. The solidification platform can rotate approximately 450° without interference. The x-ray beam penetrates the solidification platform at a height in line with the ends of the thermocouples, or approximately 378 mm above the surface of the optical table and 111 mm below the top of the furnace.

Figure 3-1: The electric-resistance furnace.

Figure 3-2: The clay-graphite crucible inside the stainless steel carriage.

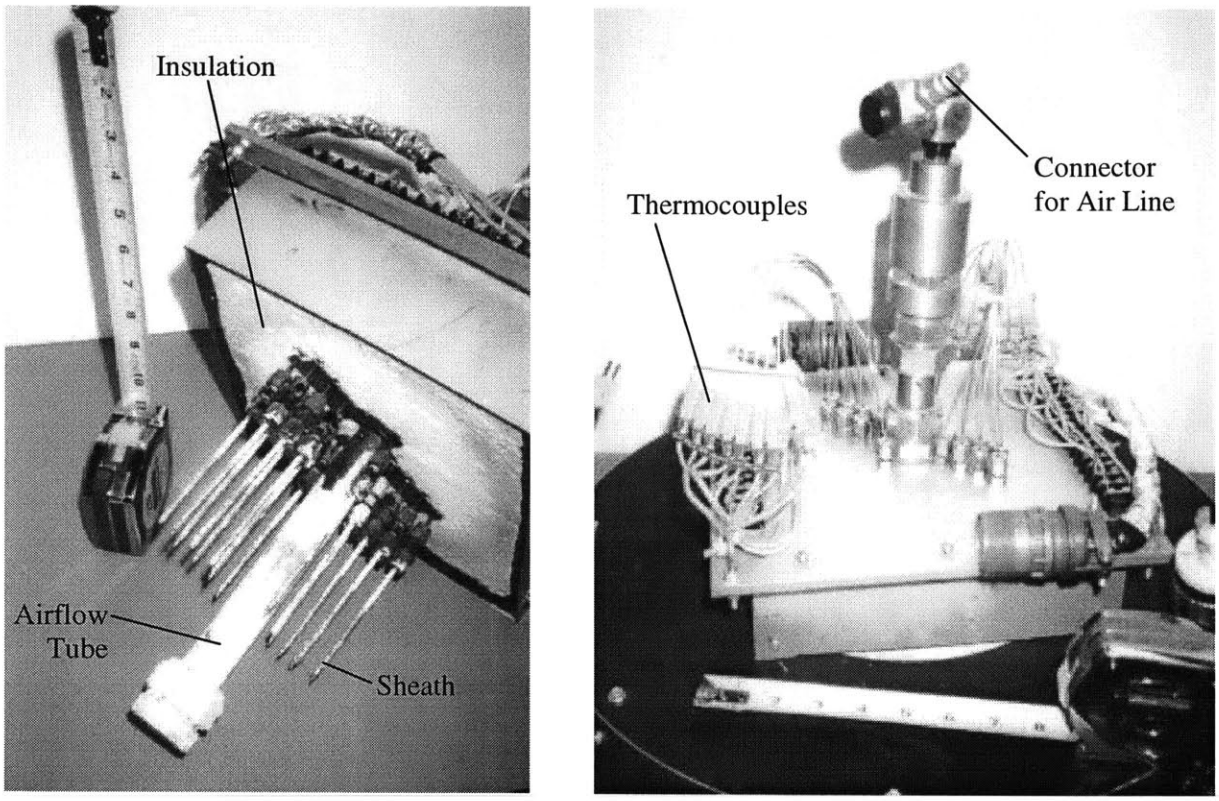

Figure 3-3: (a) Bottom view of the cooling unit. Note the central airflow tube, the thermocouple sheaths, and the ceramic insulation. (b) Top view of the cooling unit. Note the thermocouples.

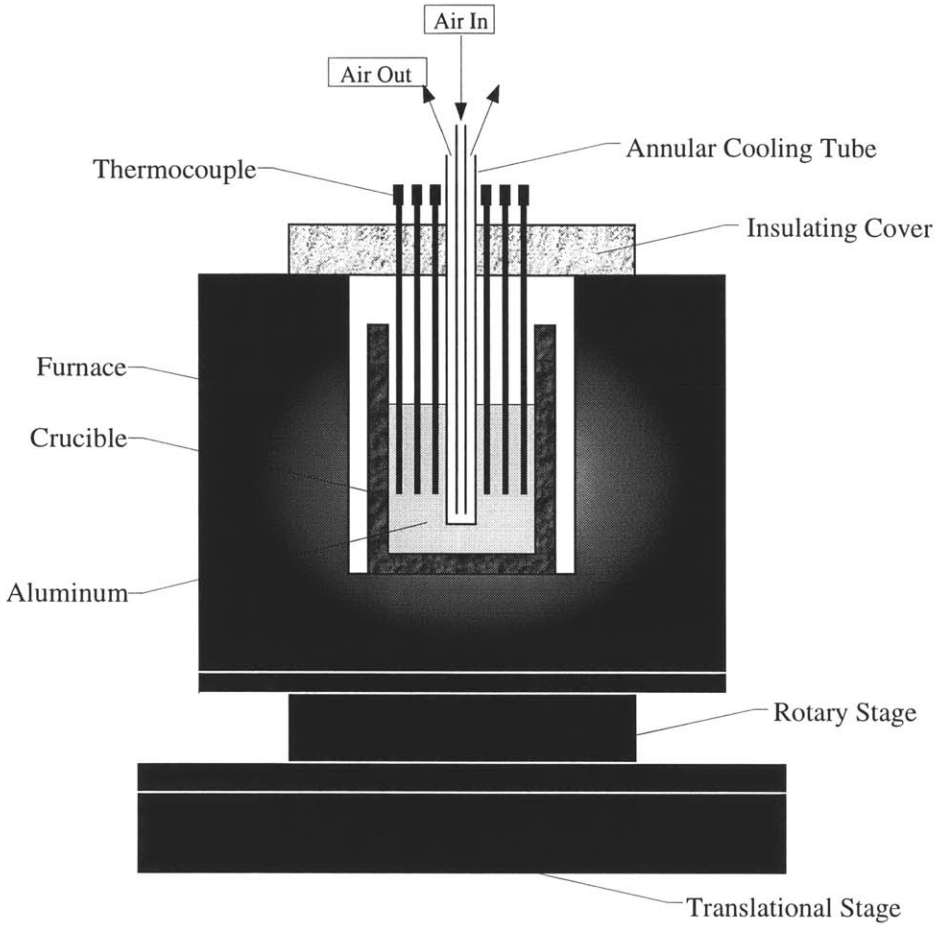

Figure 3-4: Schematic of a vertical cross-section through the solidification platform.

3.2 Solidification Model

An analytical model of the heat transfer within the system predicted the performance of the solidification platform. The goal of this model is to provide an estimate of the solidification time in a typical experiment using pure aluminum. Although many comprehensive models of the heat transfer within an ingot casting are available, these models are not appropriate for the current system. The unique manner by which the casting is forcefully cooled from its interior requires a more fundamental analysis. This simple model developed here equates the heat lost during solidification, Q_L, to the latent heat stored in the aluminum, Q_M, as outlined by Poirier and Poirier (1994):

$$Q_M = Q_L \qquad 3.1$$

The model makes several assumptions. In particular, the sources by which heat is lost from the crucible are limited to forced convection via the airflow tube, natural convection along the sides of the crucible and the top of the aluminum, and radiation from the sides of the crucible and the top of the aluminum. No other mechanisms of heat loss, such as conduction through the bottom of the crucible, are considered. The heat transfer coefficients for each of the five mechanisms of heat loss were calculated based on estimates of the experimental conditions and the solidification platform geometry. Appendix B contains a detailed analysis of the heat transfer calculations. Having determined the heat transfer coefficient for each of the five methods of heat loss, the solidification time t for a typical pure aluminum experiment is:

$$t = \frac{mH_f}{\sum_{i=1}^{5} \dot{Q}_{Li}} \tag{3.2}$$

where m is the mass of the aluminum in the crucible, H_f is the heat of fusion for pure aluminum, and $\dot{Q}_L$ is the rate of heat loss via one of the five mechanisms. The model parameters chosen were m=5 kg, H_f=3.91×10^5 J/kg, and $\dot{Q}_L$=752 J/s. Using Equation 3.2, the estimated solidification time with no superheat is:

$$t = 2600 \text{ seconds} \approx 44 \text{ minutes}$$

Assuming that the solidification front moves at a constant speed, this translates to a global average velocity of 0.024 mm/s or 1.44 mm/minute. It should be noted that this model makes many assumptions and simplifications. However, a rigorous analysis is not required. These results, although very general, provide a comprehensive estimate of the performance of the solidification platform. An expected solidification time of 44 minutes is reasonable for the sake of expedient experiments. No redesign of the solidification platform was required.

3.3 Experimental Procedure

An experiment was conducted using the solidification platform to test the ability of the CT sensor in detecting solidification front evolution. Figure 3-5 shows a schematic of the experimental setup. Pure aluminum was chosen as the test metal because of the unique manner in which it solidifies, as indicated in Figure 3-6 (Amstead et al., 1987). In a pure metal, the liquid cools until nucleation begins. From the initiation of solidification until its completion, the temperature remains constant at the solidification point, (660°C in case of pure aluminum). During solidification, latent heat balances the heat lost. Once solidification has ended, the temperature again drops with respect to time. This particular behavior produces a discrete solidification front, which is simple to detect.

For the experiment, approximately 5 kg of pure aluminum (99.99% purity) were loaded in the crucible. The crucible and carriage were lowered into the furnace and heated for roughly two hours until the aluminum was completed melted. When the melt reached approximately 800°C, the heating elements of the furnace were turned off and the cooling unit was positioned in the molten aluminum. The compressor was turned on and airflow into the tube began with a flow rate of approximately 3.3×10^{-3} m^3/s. The airflow slowly cooled the aluminum from the interior out. During this time, the temperature at each of the sixteen thermocouples was recorded once every second. In addition, the CT sensor made a series of scans.

A CT scan consisted of measuring x-ray attenuation at each detector during a 360° rotation of the furnace. Each rotation lasted one minute, during which 2700 measurements were made at each detector. After each odd numbered rotation, the furnace was shifted perpendicular to the beam direction by a distance of 0.9 mm, half the width of a detector. After each even numbered rotation, the furnace was shifted back to its original position. As a result, each odd numbered scan was taken with the solidification platform in the centered position. Correspondingly, each even numbered scan was taken with the solidification platform in a position offset by 0.9 mm. By interlacing the data from two successive scans, the result was equivalent to acquiring data over 360° using twice the number of detectors. In this case, the technique yielded a data set from 256 detectors rather than 128. This procedure yielded an image every minute with each image being a density map of the solidification platform averaged over a period of two minutes.

For example, scan #1 begins at time 0 and ends at time1. Scan #1 is taken with the solidification platform in the centered position. Scan #2 begins at time 1 and ends at time 2. Scan #2 is taken with the solidification platform in the offset position. Scan #3 begins at time 2 and ends at time 3. Scan #3 is taken with the solidification platform back in the centered position. Scan #1 and scan #2 combine to form CT image #1 and scan #2 and scan #3 combine to form CT image #2. CT image #1 is the data average of

the solidification platform between time 0 and 2, with its time average at time 1. Correspondingly, CT image #2 is the average data of the solidification platform between time 1 and 3, with its time average at time 2.

To properly correlate the temperature measurements, the thermocouple data were averaged over the same time periods at the CT image data. Furthermore, to correctly calculate the attenuation of the beam caused by the aluminum, a scan of the empty furnace had been taken prior to the experiment. This datum was also used to compensate for non-uniformities in the angular distribution of the beam and any varying detector efficiencies. With this normalization, the furnace component of the attenuation data could be effectively subtracted from the reconstructed images. As a result, the CT images do not show traces of the furnace components such as the heater elements or insulating material.[2]

The experiment lasted for approximately 70 minutes, until the entire charge of aluminum was completely solidified. At this time, CT scans and temperature measurements were stopped. The heating elements of the furnace were then turned on again to remelt the aluminum. After about 3 hours, the aluminum was completely molten and the cooling unit was removed from the crucible. The aluminum again completely resolidified inside the crucible. Once at room temperature, the aluminum had shrunk so that it could be freely removed from the crucible as a solid cylindrical billet.

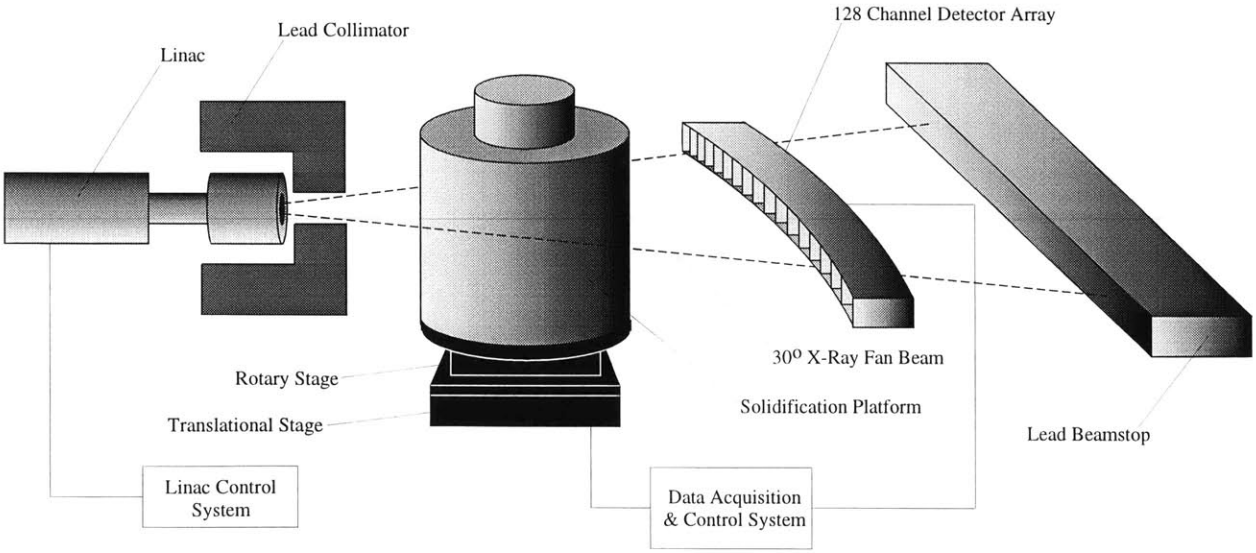

Figure 3-5: Schematic of solidification experiment and CT sensor layout.

[2] Some CT images do show traces of the furnace heater elements resulting from their thermal expansion/contraction. This is not a result of the normalization method described herein. The issue is addressed in Section 3.4.2.

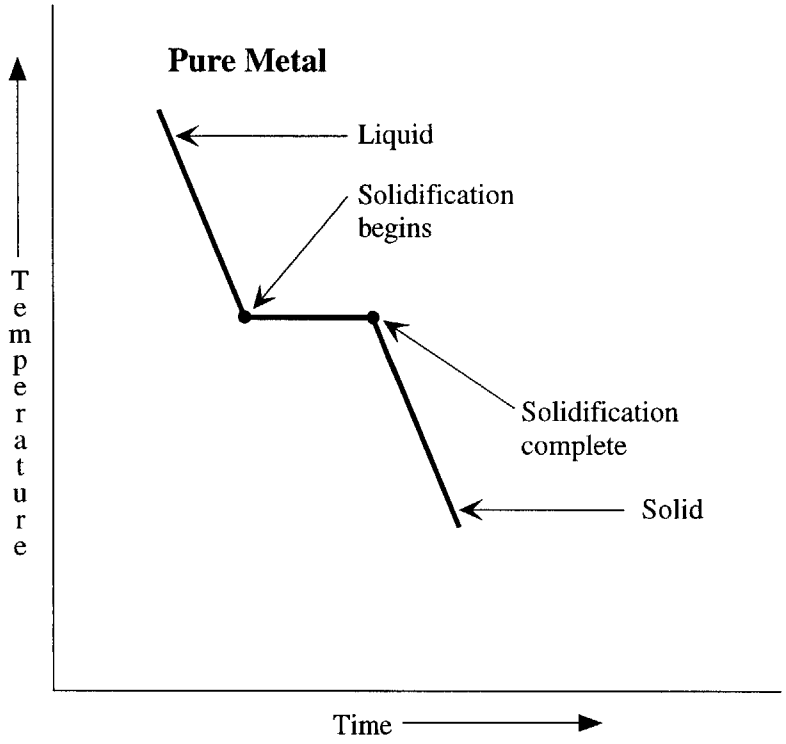

Figure 3-6: Time-temperature curve for a pure metal.

3.4 Results

The pure aluminum solidification experiment performed 27 CT scans. These scans were reconstructed into a time sequence of 54 CT images, as described in Section 3.3. Each image was 512 by 512 pixels in size. This corresponds to a scaling of 0.53 mm/pixel. The pixel values in the image were calibrated so that the computed density of liquid aluminum at 700°C was 2.357 g/cm^3 (Hatch, 1984).

3.4.1 Standard CT Image

Figure 3-7a shows a CT image from the aluminum solidification experiment. This particular image is number 32 in the sequence of 54. It was acquired 39.5 minutes after the experiment was started. The colorbar on the right relates the pixel intensity to the computed density of the materials in the image. Visible in the image are the aluminum, the graphite crucible, the stainless steel cooling tubes, the thermocouples, and the steel support rods of the crucible carriage, as illustrated in Figure 3-7b. Also visible are some traces of the furnace's ceramic heating elements located about the exterior of the crucible. In theory, the heating elements should not be present in the image. Normalizing the image using the attenuation data from an empty furnace should remove any trace of the furnace and its

components. However, the theory assumes that none of the furnace components changed position or density between the two scans. In the case of the heater elements, their position changes because of thermal expansion during the course of normal operation. As a result, their contribution to the attenuation is not completely removed during normalization, thus, they appear in the CT image.

The aluminum in this image is in a two-phase state, as indicated by the temperatures recorded by the thermocouples. At 660°C, the expected density of the liquid phase is 2.37 g/cm^3, while the expected density of the solid phase is 2.55 g/cm^3 (Zinov'ev, 1996). This is a difference of 0.18 g/cm^3. The contrast resolution was determined by calculating the mean pixel value and the standard deviation in the liquid aluminum region. They were found to be 2.373 g/cm^3 and 0.065 g/cm^3, respectively. This translates to a contrast resolution of 2.7%. This resolution was not enough to positively identify the solidification front in the CT image using an absolute density scale.

To better illustrate the effect of pixel noise, one can plot the computed density versus position, as shown in Figure 3-8a and 3-8b. The peaks in Figure 3-8b indicate the location of the dense steel rods, cooling tube, and thermocouples. Within the aluminum region however, the noise washes out any variation between the solid and liquid phases. On this absolute scale, the dynamic range is insufficient to see any density difference. Since the solidification front position was not identifiable using a standard CT image, an additional technique was required to enhance the front's visibility.

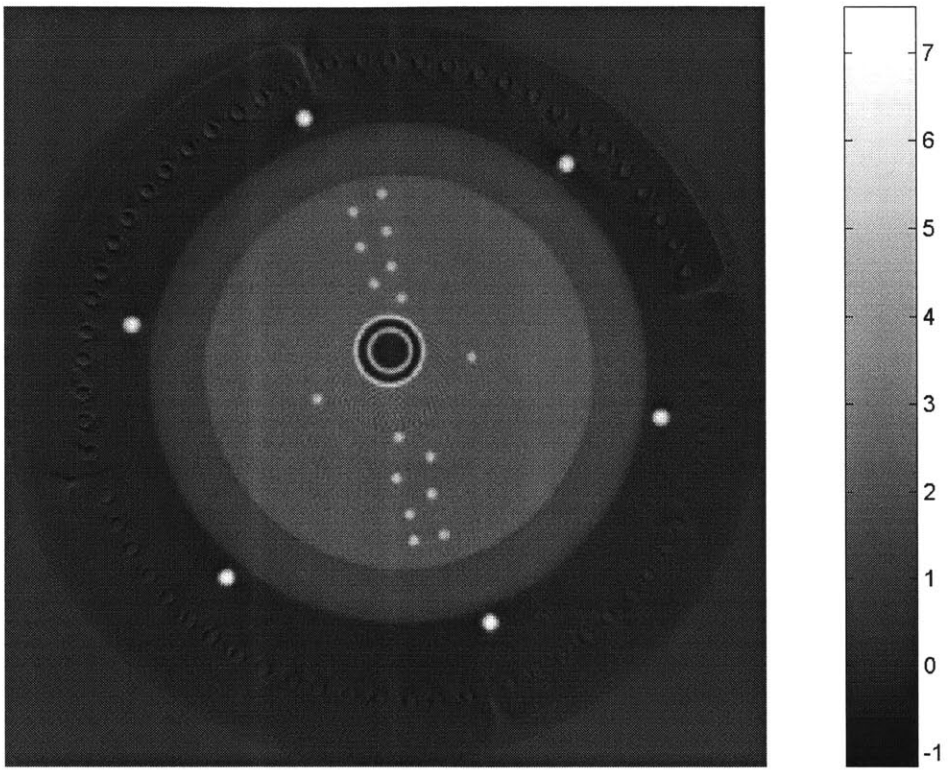

(a)

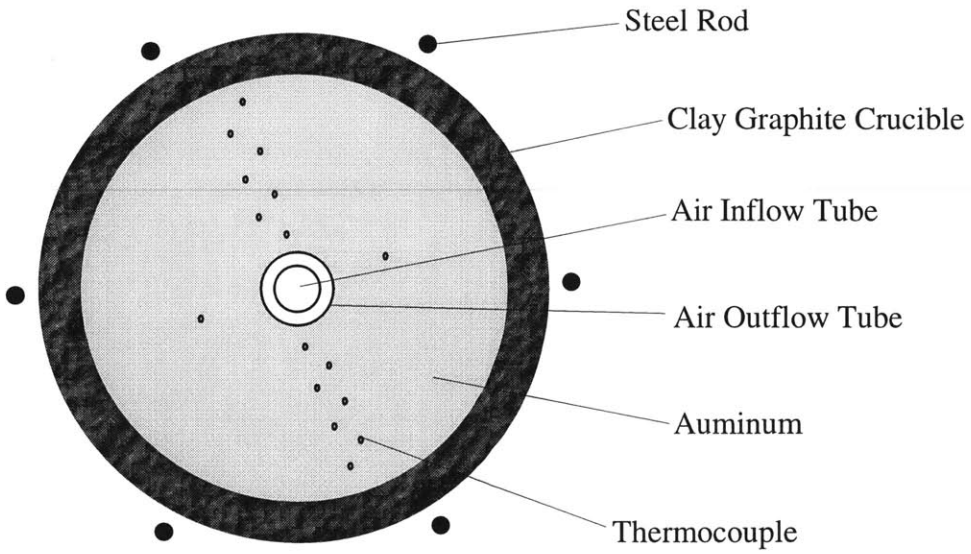

(b)

Figure 3-7: (a) CT image of the pure aluminum solidification experiment taken at time = 39.5 minutes. The pixel intensity in the CT image corresponds to the density of the material in units of g/cm^3 as represented by the colorbar. (b) Schematic of the CT image features.

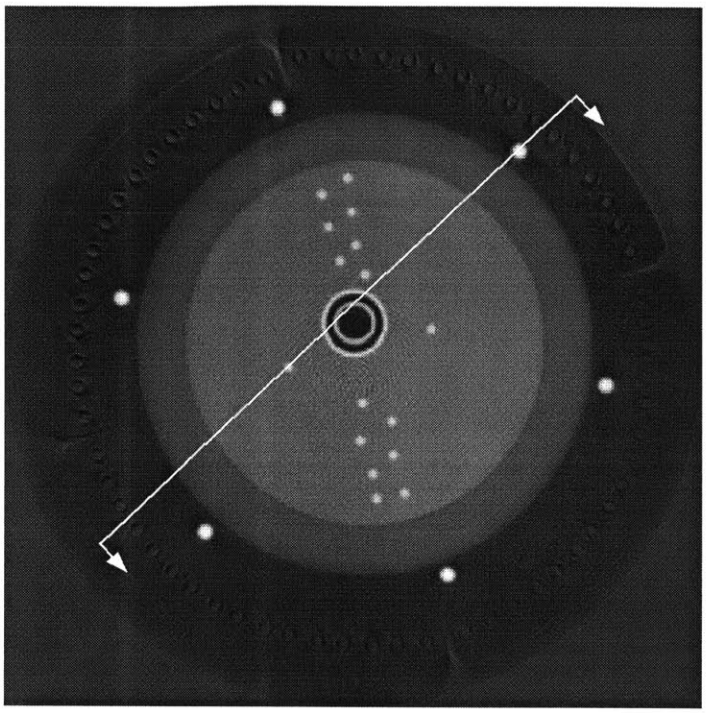

(a)

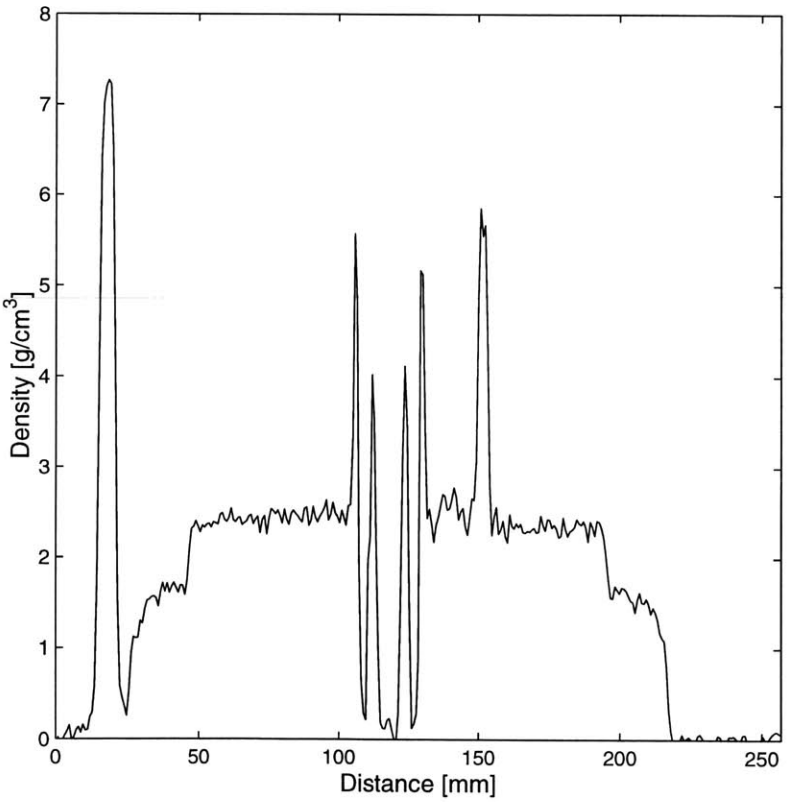

(b)

Figure 3-8: (a) CT image of solidification experiment at time = 39.5 minutes. (b) Plot of computed density vs. position taken along the line shown in (a).

3.4.2 Difference CT Image

This technique, referred to as the difference image method, enhances the visibility of the solid and liquid phases of the aluminum in the CT image. The process involves subtracting an image obtained when the aluminum is completely liquid from an image when a portion of the aluminum is solidified. The resulting image shows only the difference in density. The only structures visible in the second image are those which changed either density or position. In this case, only the density variation between the solid and liquid aluminum should be visible since all other structures in the image remain constant. The method essentially identifies the regions of the aluminum that have solidified.

The liquid image chosen for the subtraction was image number 18, acquired 22.2 minutes from the start of the solidification experiment. This was one of the last images in which the aluminum was still completely liquid. It was chosen because the temperature of the aluminum was very near the solidification temperature. Figures 3-9a and 3-9b show CT images taken at two different times during the solidification experiment, 22.2 minutes and 39.5 minutes, respectively. Although the aluminum in the first image is completely liquid, and solidifying in the second, there is no discernable difference between them on an absolute scale. When the first image is subtracted from the second, the result is the difference image shown in Figure 3-9c. The solidification front position is now visible. Figure 3-10 shows an enlarged difference CT image of the solidification experiment at time = 39.5 minutes. The colorbar on the right relates the pixel intensity to the computed density of the material in the image. The brighter pixels indicate the solidified aluminum. Ideally, objects that are constant in density and position should vanish. As mentioned earlier however, the thermocouples and steel support rods contract as they cool. As a result, their position and density change, resulting in their appearance in the difference image.

Using the difference image technique, the evolution of the solidification front over the course of the pure aluminum experiment is easily visualized. Figures 3-11a through 3-11i show nine illustrative difference images. After 23.3 minutes, the pure aluminum was still entirely liquid (Figure 3-11a). At 28.3 minutes, solidification began around the cooling tube (Figure 3-11b). The solidification continued to grow outward over the next 11 minutes (Figures 3-11c and 3-11d). After 43.1 minutes, a second solidification front formed around the exterior of the aluminum (Figure 3-11e). After 45.5 minutes, the aluminum began to shrink (Figure 3-11f). While the aluminum was still solidifying, large voids formed after 51.0 minutes (Figure 3-11g). Solidification was almost complete after 53.5 minutes (Figure 3-11h). Finally, 57.5 minutes after the start of the experiment, the aluminum was completely solid (Figure 3-11i).

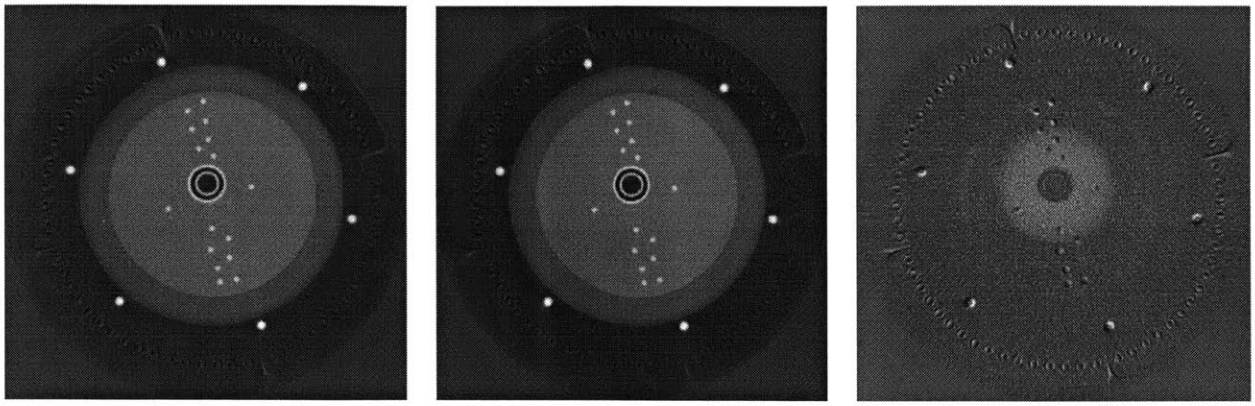

(a) Image at 22.2 minutes (b) Image at 39.5 minutes (c) Difference image

Figure 3-9: (a) CT image at time = 22.2 minutes during which the aluminum is entirely liquid. (b) CT image at time = 39.5 minutes during which the aluminum is both liquid and solid. (c) Difference image created by subtracting the CT image in (a) from the CT image in (b). Note that the location of the solidification front is now visible.

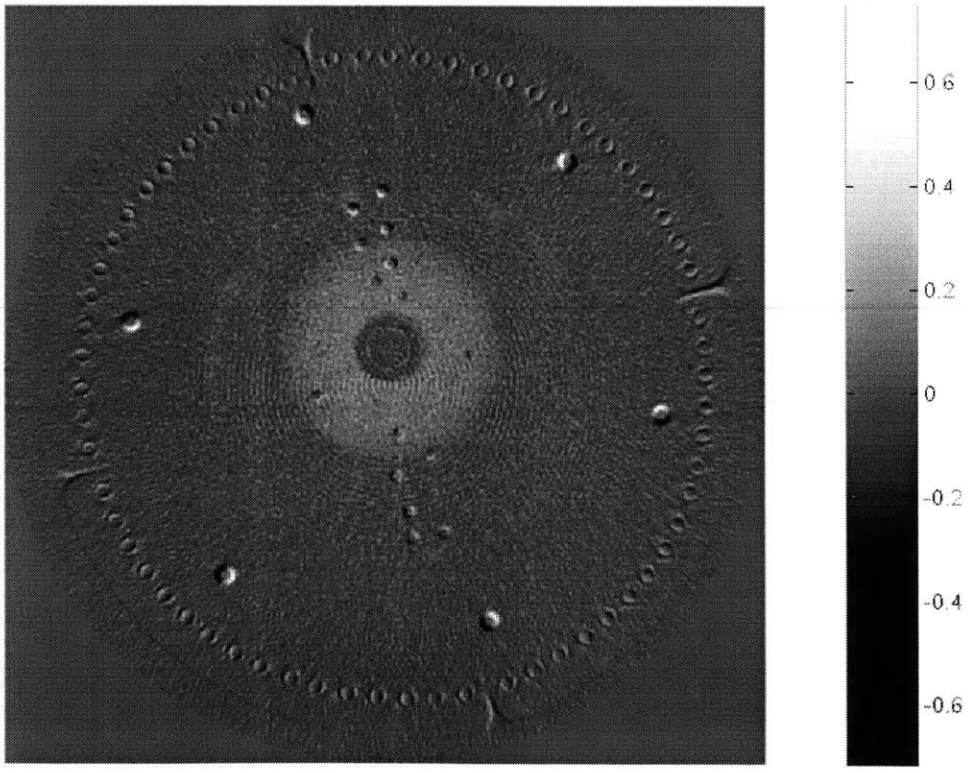

Figure 3-10: Difference image of the solidification front position in the pure aluminum at time = 39.5 minutes. The pixel intensity in the CT image corresponds to the difference in density in units of g/cm^3 as represented by the colorbar.

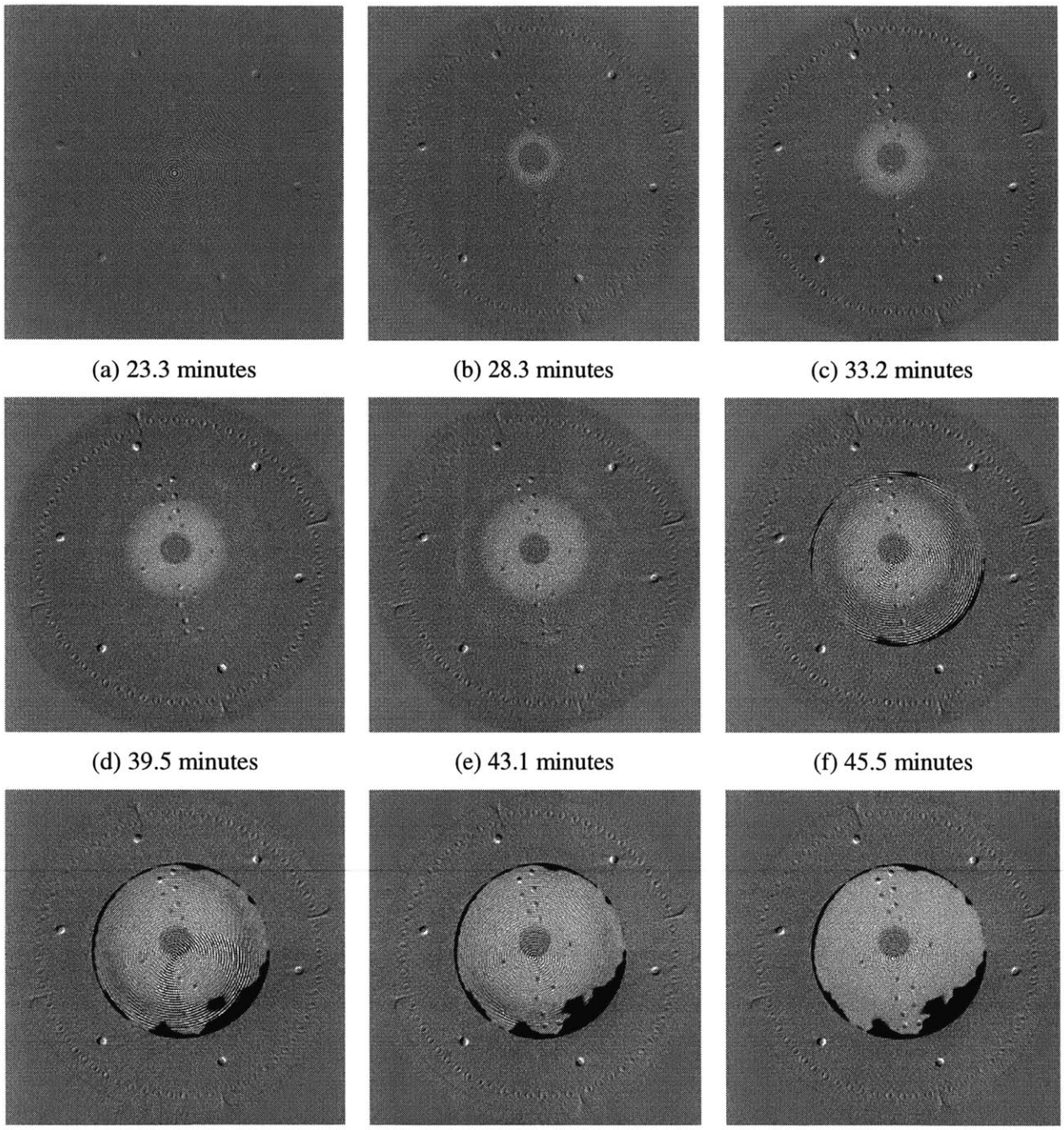

(a) 23.3 minutes (b) 28.3 minutes (c) 33.2 minutes

(d) 39.5 minutes (e) 43.1 minutes (f) 45.5 minutes

(g) 51.0 minutes (h) 53.5 minutes (i) 57.5 minutes

Figure 3-11: Nine difference images showing the evolution of the solidification front in pure aluminum over a period of 34 minutes, from (a) time=23.3 minutes to (i) time=57.5 minutes.

3.4.3 Temperature Verification

Using the difference CT method, it is possible to track the evolution of the solidification front position. However, these results mush be verified independently. Validity was checked using temperature measurements inside of the crucible. Because of the discrete solidification temperature of pure aluminum, 660°C, the liquid and solid phases are easily identified by temperature. A measurement above 660°C indicates a molten region and a measurement below 660°C indicates a solidified region. A tree of chromel-alumel thermocouples and a PC-based data acquisition system recorded the temperature at sixteen locations inside the aluminum. The measurements were recorded once every second over the course of the entire solidification experiment. For reference, the thermocouples are numbered according to the designation shown in Figure 3-12.

To verify the results, four difference images are shown in Figures 3-13a through 3-13d. The average temperature measurement recorded at each of the sixteen thermocouples is superimposed on each image. The temperature measurements were averaged over the same time period during which the CT image was acquired. For example, the CT image shown in Figure 3-13c was acquired from a time of 37.0 minutes to 39.5 minutes. The thermocouple measurements shown in the overlay were averaged during this same period. The error in each of the averaged thermocouple measurements is approximately 0.4°C.

In general, the thermocouple measurements correlate well to the results of the CT technique. In Figure 3-13a, no solidification is visible in the image. Correspondingly, the temperature everywhere within the aluminum is above 663°C. In Figure 3-13b, the aluminum is beginning to solidify around the cooling tube. Thermocouple measurements at position numbers 8, 9, 10, 11, and 16 reflect this by showing a small temperature gradient relative to the other thermocouples. In Figure 3-13c, the solidification front is well evolved. Based on the CT image, thermocouple numbers 1, 8, 9, 10, 11, 12, and 16 are located entirely within the solidified region. These seven thermocouples do read temperatures below 660°C. The remaining thermocouples, all located in the molten aluminum, measure temperatures above 660°C. Finally, as indicated by the image in Figure 3-13d, the aluminum is completely solidified. The temperature measurements confirm this result since no reading is above 660°C. Based on this comparison of CT images to independent temperature readings, the CT measurement of the solidification front evolution appears genuine. These positive results validate the use of high-energy x-ray CT as feasible solidification sensor technology

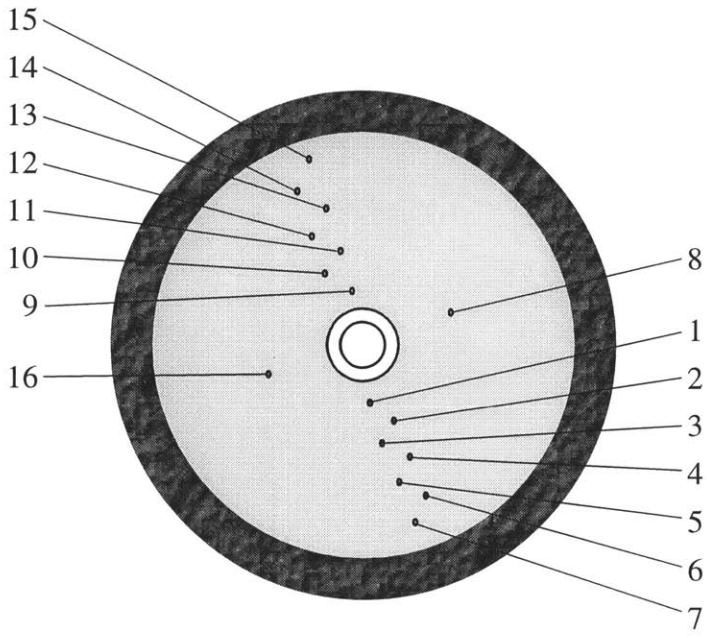

Figure 3-12: Schematic of thermocouple numbering standard.

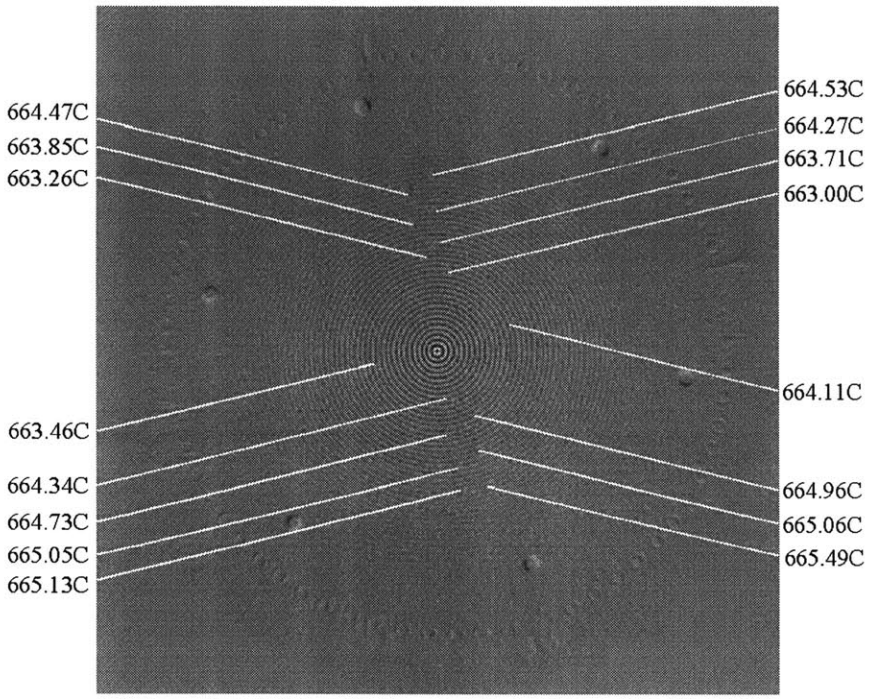

(a) Difference image at time = 23.3 minutes.

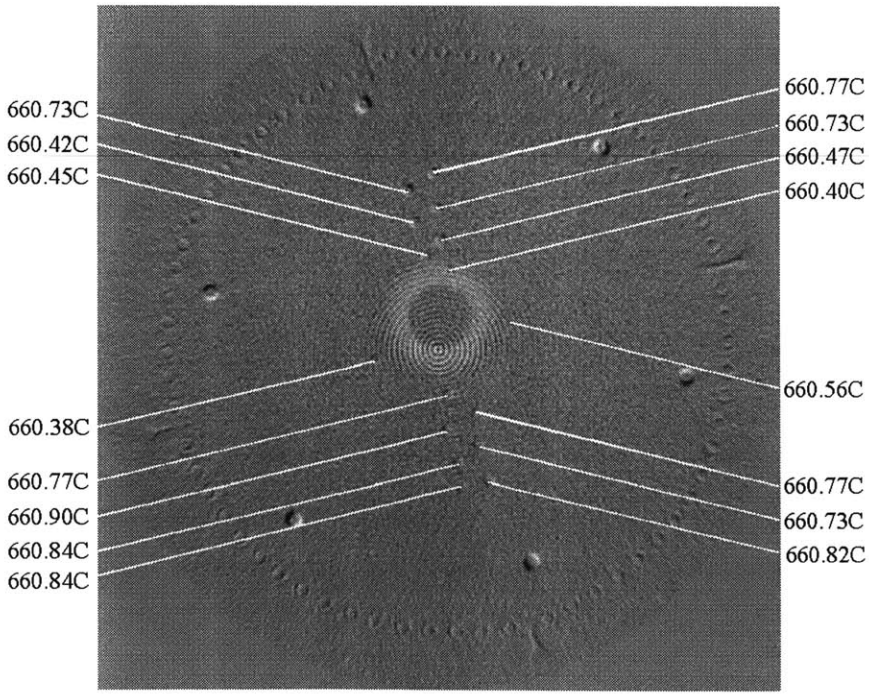

(b) Difference image at time = 28.3 minutes.

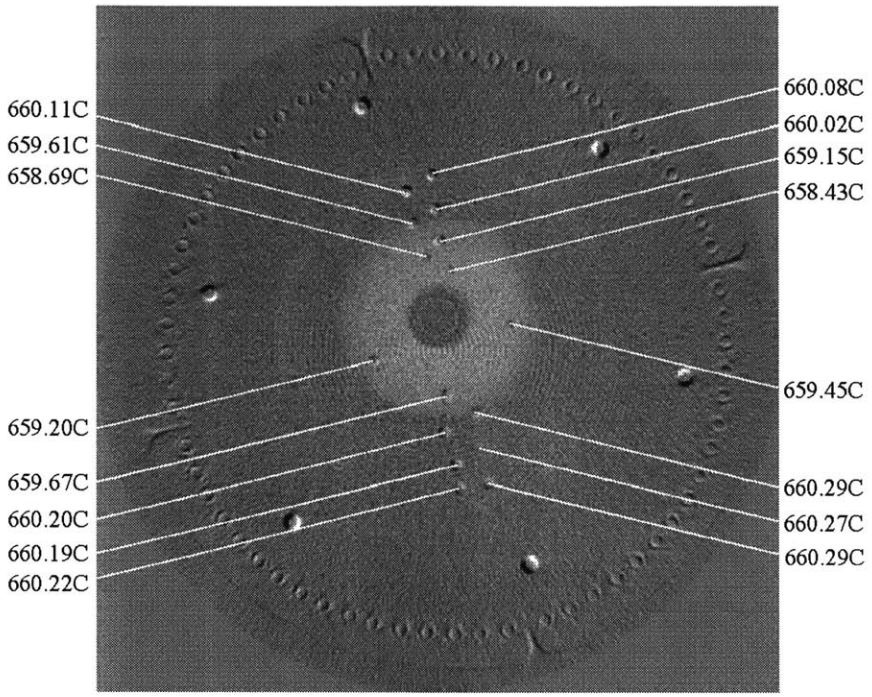

(c) Difference image at time = 39.5 minutes.

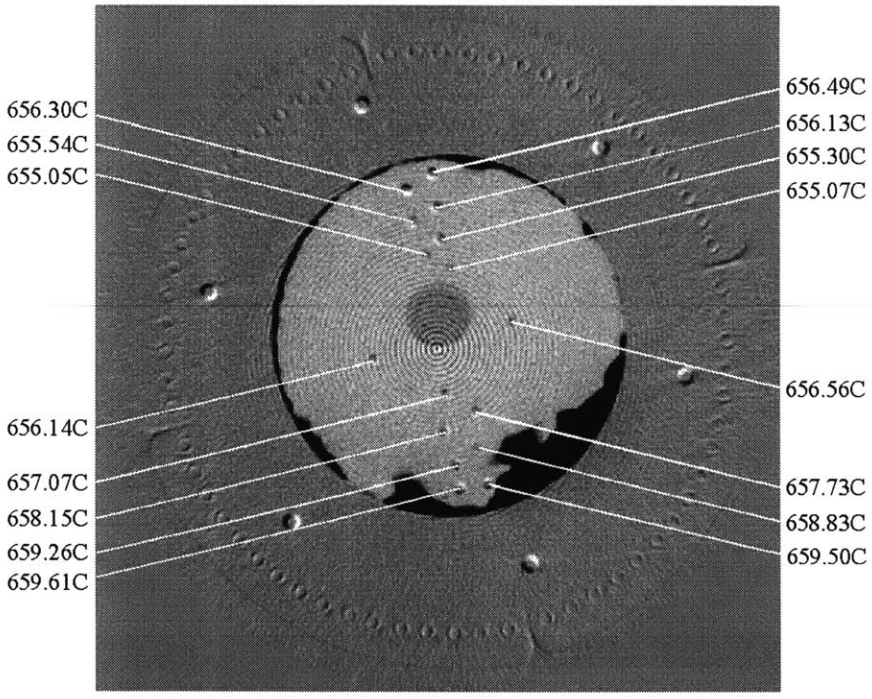

(d) Difference image at time = 57.5 minutes.

Figure 3-13: Four difference images at times (a) 23.3 minutes, (b) 28.3 minutes, (c) 39.5 minutes, (d) 57.5 minutes, overlaid with corresponding thermocouple temperature measurements.

3.4.4 Density Profile

The results of the solidification experiment show that by using CT difference images the liquid and solid phases of pure aluminum can be differentiated. This conclusion is supported by independent temperature measurements. However, the thermocouple data provide no quantitative assessment on the accuracy of computed density. This was done by comparing the density profiles of the CT images to the expected density for pure aluminum. The density profile was generated by plotting the pixel value versus position along a given cross-section through the difference image. The pixel values correspond to the difference in density between the two images, as explained in Section 3.4.2.

Figures 3-14 and 3-15 present an analysis of two difference images at distinct stages in time, 28.3 minutes and 39.5 minutes. In the figures, the first frame (a) shows the CT difference image. The second frame (b) shows the density profile plotted along the cross-section superimposed in (a). A large amount of high-frequency noise is prevalent in both of the figures. This noise originates from the ring artifacts that are universally present in the CT images from the solidification experiment. These ring artifacts are the single greatest source of error for this CT system. Typically, ring artifacts result from a misalignment in the center of rotation of the phantom or from an uncalibrated detector array (Schneberk et al., 1990). Although these factors undoubtedly play some role in the current case, they are not the dominant cause.

The rings are a function of this system's unique method of acquiring CT scans. After a series of tests, it was determined that the two primary sources of the ring artifacts and resultant high-frequency noise are temporal variations in the phantom and temporal variations in the output intensity of the linac. As stated earlier, a CT scan involves acquiring attenuation data over 360°, shifting the phantom by a half-detector width, and acquiring a second set of data over 360°. The half-detector shift produces an offset in the sinogram such that when the two data sets are combined, the result is a sinogram that appears to have been acquired with double the number of detectors. The benefit of this technique is that the spatial resolution is increased. However, if either the output intensity of the linac or the composition of the phantom changes in time, the attenuation data in the second CT scan will vary significantly from the first. The variation between the two data sets becomes extremely significant when the two sinograms are interlaced. The FBP algorithm amplifies the variation in the combined sinogram, resulting in the ring artifacts.

Using an FFT analysis, the frequency of the ring artifacts was found to range between 0.25 to 0.33 cycles/pixel (0.46 to 0.62 cycles/mm). To remove this high-frequency component, the difference images were processed using a low-pass filter (two-dimensional Gaussian). The results of this operation are shown in the third frame (c) of Figures 3-14 and 3-15. The density profile of the filtered CT image is shown in the last frame (d). Although it reduced the high-frequency noise, the low-pass filter also produced some blurring of the image features. The blurring reduces both the spatial and contrast

resolution. An analysis of both the original CT images and the filtered images was performed for comparison. Table 3-1 shows the expected density as a function of temperature for pure aluminum (Hatch, 1984; Zinov'ev, 1996). The experimental density difference was found by measuring the value of the pixels in the solid region in the CT images of Figure 3-14 and 3-15. The results are shown in Table 3-2.

In Figure 3-14, acquired at 28.3 minutes, the pure aluminum has just begun to solidify around the cooling tube. The measured density difference in the unfiltered and filtered images is 0.1072 and 0.1067 g/cm^3, respectively. In Figure 3-15, acquired at 39.5 minutes, the solidification front has evolved further. The measured density difference in the unfiltered and filtered images is 0.1346 and 0.1304 g/cm^3, respectively. At both times, the measured values are less than the expected value of 0.182 g/cm^3. In the case of the unfiltered images, this underestimation results from the high-frequency noise. The image in Figure 3-14 is more affected by this phenomenon, as indicted by the higher standard deviation in the measurement. The rings have a more prevalent effect near the center of the image. In the case of the filtered images, a blurring effect due to the filtering operation lowers the measured density. Despite the undervalued measurements of the density difference, the results are near the expected value, given the standard deviation in the measurement. Elimination of the ring artifacts would no doubt significantly enhance the results.

The density profiles shown in the (c) and (d) frames of Figures 3-14 and 3-15 provide both a visual and a quantitative measure of the distinctness of the solidification front. As mentioned in Section 3.3, the interface between the liquid phase and the solid phase of a pure metal is discrete. This interface is readily seen by the rise in the filtered density profiles. Ideally, this discrete rise should match the spatial resolution of the system, roughly 1.7 to 1.8 mm. However, the interface is actually blurred in all of the CT images. The blurring results from movement of the solidification front during data acquisition. The actual velocity proves difficult to measure accurately. The speed of the solidification front is estimated to range from 0.1 mm/s near the cooling tube to 0.01 mm/s when solidification was nearly complete. A global average velocity of 0.04 mm/s was computed based on the time required for total solidification. This is close to the predicted average velocity of 0.024 mm/s. It translates to a growth of 4.8 mm in the solidification front during a single CT scan. Given the spatial resolution of 1.76 mm, a velocity of 0.04 mm/s results in noticeable blurring. Resultantly, the interface rise measured in Figure 3-14d occurs over approximately 10 mm. The interface rise measured in Figure 3-15d occurs over approximately 15 mm.

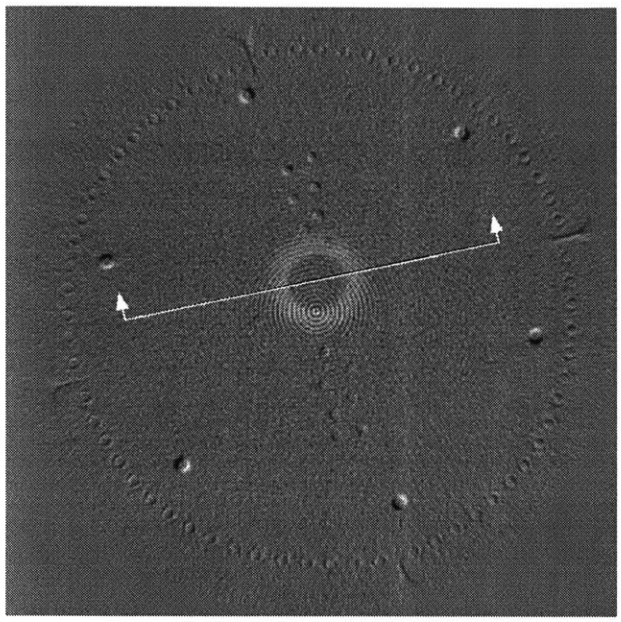

(a)

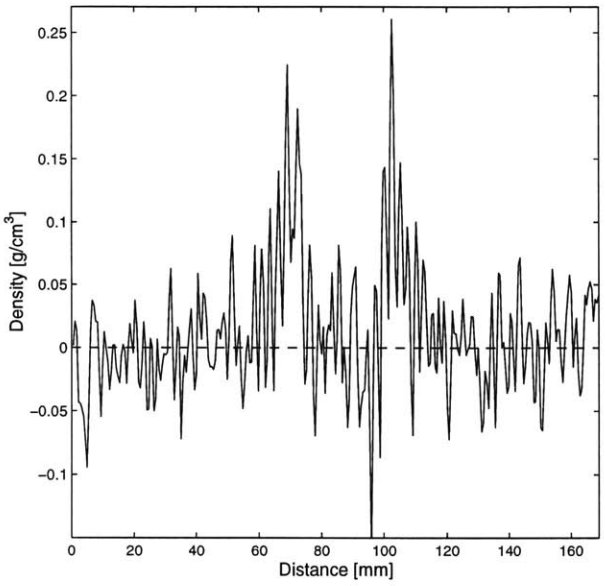

(b)

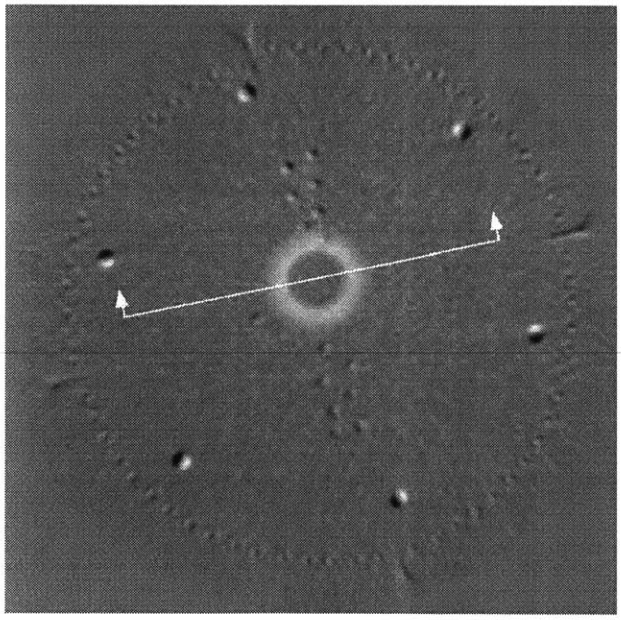

(c)

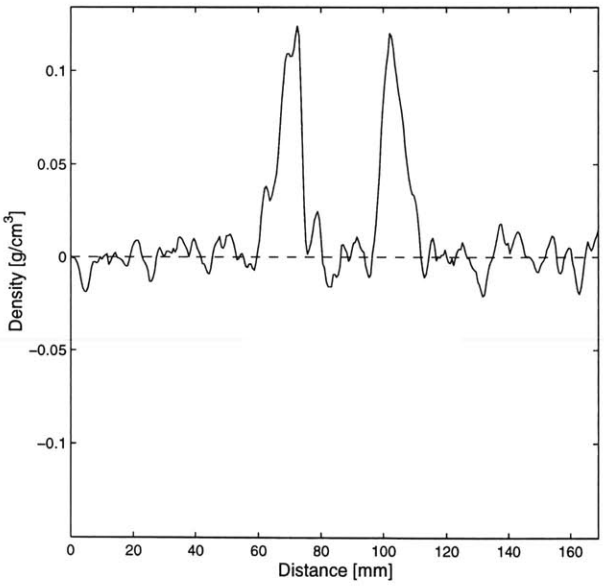

(d)

Figure 3-14: (a) Difference image at time = 28.3 minutes. (b) Computed density vs. position along line shown in (a). (c) Difference image from (a) with noise removed using a Gaussian filter. (d) Computed density vs. position along line shown in (c).

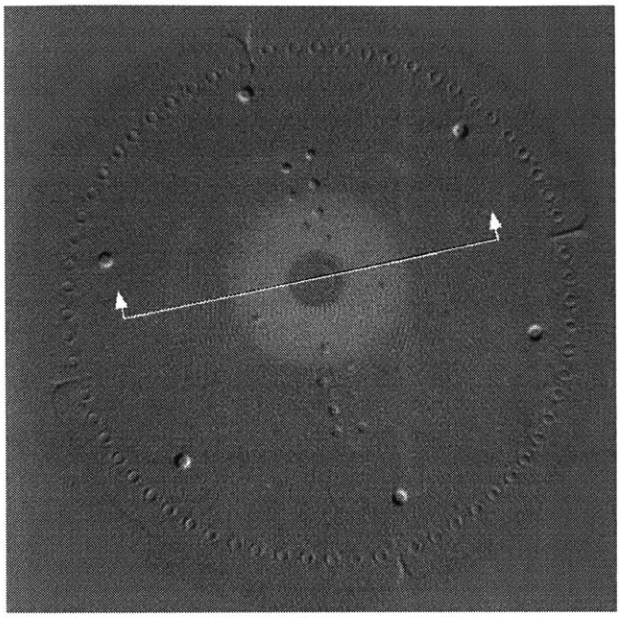

(a)

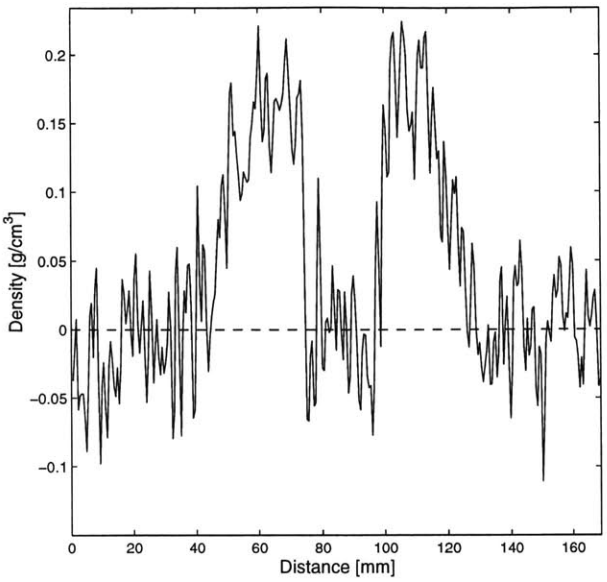

(b)

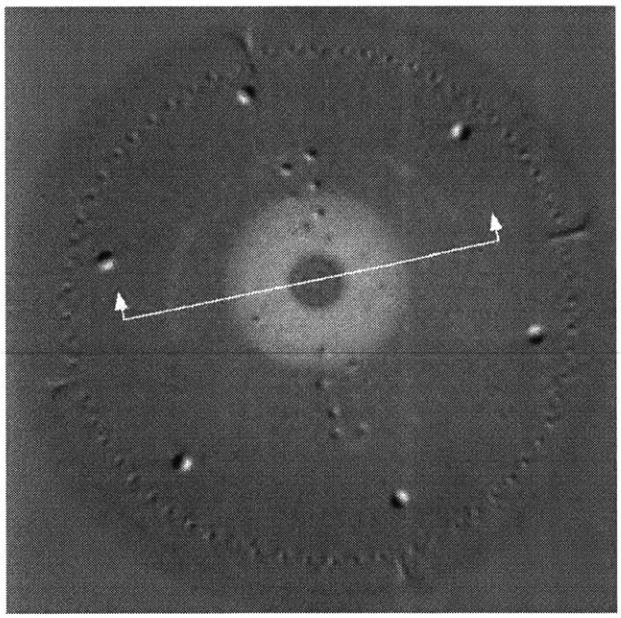

(c)

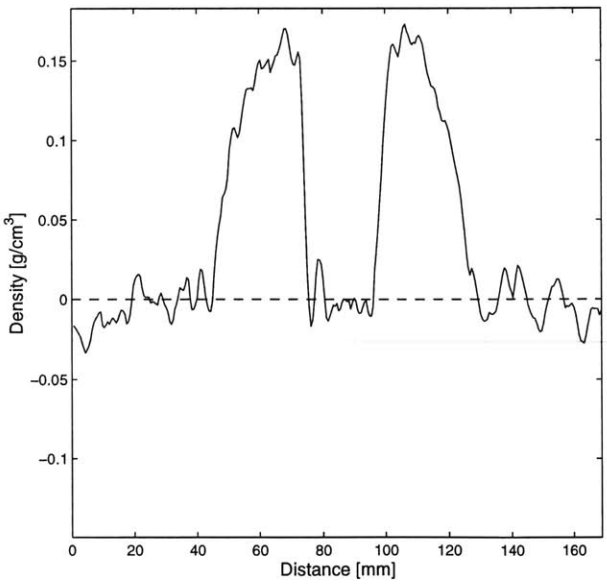

(d)

Figure 3-15: (a) Difference image at time = 39.5 minutes. (b) Computed density vs. position along line shown in (a). (c) Difference image from (a) with noise removed using a Gaussian filter. (d) Computed density vs. position along line shown in (c).

Table 3-1: Density of pure aluminum at selected temperatures.

Temperature [°C]	Density [g/cm^3]
27	2.697
127	2.675
227	2.665
327	2.652
427	2.626
527	2.595
627	2.560
660 (solid phase)	2.550
660 (liquid phase)	2.368
700	2.357
727	2.350
750	2.345
800	2.332
850	2.319
900	2.304
927	2.290

Table 3-2: Computed density difference for three difference images.

Difference Image Time [minutes]	Computed Density Difference [g/cm^3]	Standard Deviation in Measurement
28.3 (unfiltered image)	0.1072	0.0784
28.3 (filtered image)	0.1062	0.0752
39.5 (unfiltered image)	0.1346	0.0426
39.5 (filtered image)	0.1304	0.0451

3.4.5 Time Evolution of Computed Density

During the solidification experiment, the density of the pure aluminum slowly increased over time. The thermocouple measurements confirm that the solidification experiment began with the aluminum in a completely molten state at 760°C. The expected density of pure aluminum at this temperature is 2.342 g/cm^3. At the conclusion of the experiment, the aluminum was completely solid at a temperature of 650°C and an expected density of 2.553 g/cm^3. The evolution of the computed density over time was confirmed experimentally using the CT images. The analysis was performed using an absolute density scale. First, the density was measured within a small region-of-interest (ROI) in each CT image. The same ROI (size, shape, and location) was used for every image. Then, the average density within the ROI was plotted against the time step of the image. The result is an experimental measure of the density in a single small region within the aluminum, plotted over the time period of the solidification experiment. Figure 3-16a shows the location of an ROI within the CT image. It measures roughly 5 by 5 pixels (2.65 mm by 2.65 mm). The ROI lies near a thermocouple so that the temperature measurement would be as nearly as possible representative of the temperature in the ROI. Figure 3-16b shows the computed density within the ROI as a function of time. The temperature at the nearby thermocouple is also plotted.

Based on the results from the ROI analysis, the density of the pure aluminum during the course of the solidification experiment can be categorized into three regimes. A linear curve is best fit to the computed density data in each of the three regimes. The result is superimposed in Figure 3-16. In the first regime, the pure aluminum is in a molten state. From Figure 3-16b, the computed density is approximately 2.32 g/cm^3 at the start of the experiment. This result correlates well with the expected density. During the next 24 minutes, the liquid aluminum cools, as indicated by the decreasing temperature reading. The density of the aluminum slowly increases during this time. At 660°C, the computed density is 2.35 g/cm^3, again correlating well with the expected value at this temperature. At roughly time=24 minutes, the solidification front begins to pass through the ROI. During this second phase, the computed density quickly increases from 2.35 g/cm^3 to 2.50 g/cm^3. Ideally, this phase transformation should be discrete enough to occur over two data points, or roughly 1.3 minutes. Given the finite area of the ROI coupled with the blurring effect from the moving solidification front, the transformation actually occurs over a period of approximately 8 minutes. In the final phase, the solidified aluminum continues to cool, as indicated by the thermocouple measurement. The computed density slowly increases from 2.5 g/cm^3 at 32 minutes to 2.57 g/cm^3 at 66 minutes. At the conclusion of the experiment, the pure aluminum in the ROI is at approximately 646°C. The results correspond with the expected density for pure aluminum at this temperature.

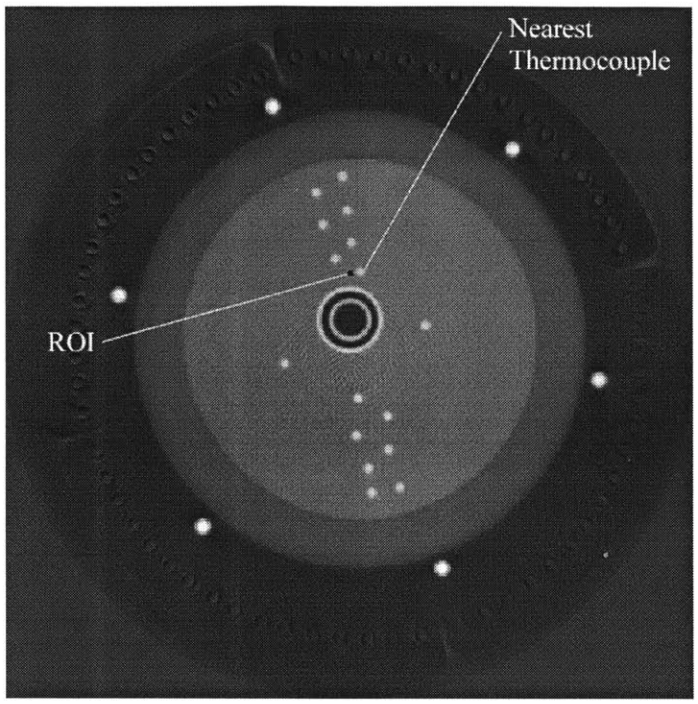

(a)

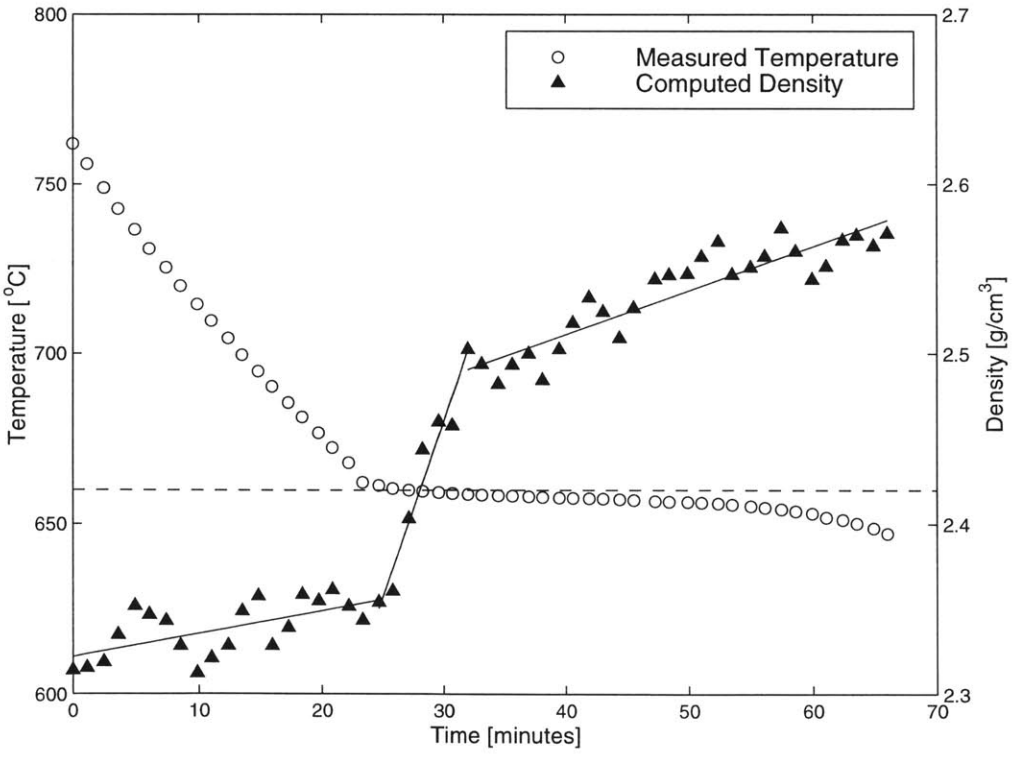

(b)

Figure 3-16: (a) Location of region of interest (ROI) in the CT image. (b) Computed density and temperature in the ROI plotted over the time of the solidification experiment.

3.5 Discussion

Based on the results of the solidification experiment, the CT sensor developed in this work can detect the position and time evolution of the liquid/solid interface during casting of pure aluminum. It is difficult to visually detect the solidification front in a CT image with an absolute density scale, since the contrast resolution is on the order of 3%. By manipulating two CT images however, the result amplifies any density change between them. In this case, by subtracting an image of partially solidified aluminum from an image of entirely molten aluminum, the solidified region is easily visible in the difference image. The shape and location of the solidification front was confirmed using temperature measurements. In addition, quantitative measurements of the computed density, in a single CT image and over the course of the entire experiment, correlate with the expected values.

Despite the success of these results, there are some notable problems with the performance of the CT sensor. The most obvious concern is the ring artifacts present to some extent in all of the CT images acquired during this experiment. These ring artifacts introduce significant high-frequency noise, which degrades the overall resolution of the images. The rings were found to occur if either the x-ray output of the linac or the composition of the phantom changes significantly during the acquisition of a CT scan. If neither occurs, then the rings are minimized or vanish completely.

In regard to the stability of the x-ray output, the problem is inherent to this particular linac. Extensive testing found that the linac is very susceptible to thermal instabilities. There are two particular cases. Upon startup, the linac requires approximately 15 to 20 minutes to achieve a state where the x-ray beam is relatively stable. During operation, the linac often drifts away from the resonance frequency required for peak output. Both situations require constant observation and adjustment of the linac output. Notwithstanding, the most significant factors that affect the x-ray output are large spikes and/or drops in the linac power supply. This is an unfortunate circumstance of the particular design of the CT system and solidification experiment. During the course of a solidification experiment, the compressor that supplies the cooling airflow to the aluminum systematically cycles on and off to replenish the reservoir pressure. While the pump is on, the entire power grid experiences a drop in voltage. This effect is reflected in the x-ray output of the linac as a periodic fluctuation. Unfortunately, this occurs during acquisition of CT scans, affecting the data. The clear solution is to isolate the power supply of the linac from the power supply of the air compressor. However, the infrastructure of the laboratory prevents this from being easily implemented.

The second major cause of the ring artifacts is variations in the composition of the phantom while the CT scan is being acquired. In particular, solidification front movement during the course of a CT scan creates variation between the two sinograms. Once the sinograms are interlaced, the variation is amplified by the FBP reconstruction, resulting in the ring artifacts. A simplified example of this effect is

shown in Figure 3-17. Unfortunately, the fundamental design of the solidification experiment prevents this effect from being eliminated or even minimized. To reduce this effect without changing the CT hardware or data acquisition routine, the solidification experiment would need to be redesigned to eliminate the moving solidification front. Resultantly, the solidification platform would require actively controlled heating and cooling to produce a stable, steady-state solid/liquid interface. Such a design was briefly examined, but an extremely long time was required to achieve a stable temperature gradient within the melt. The large thermal mass of the aluminum charge precludes use of this technique.

A second alternative for reducing or eliminating the ring artifacts is to increase the speed of data acquisition. Since both the x-ray intensity variations and the solidification front movement are functions of time, their effect should presumably be minimized if the CT scan can be acquired more rapidly. As discussed in Section 2.3.5, the data acquisition time could be reduced to roughly 30 seconds without any loss in resolution. However, an improved rotary positioning stage would be needed to replace the current equipment.

Although there is room for improvement, the solidification images of the pure aluminum are illustrative of both the qualitative and quantitative capability of this sensor.

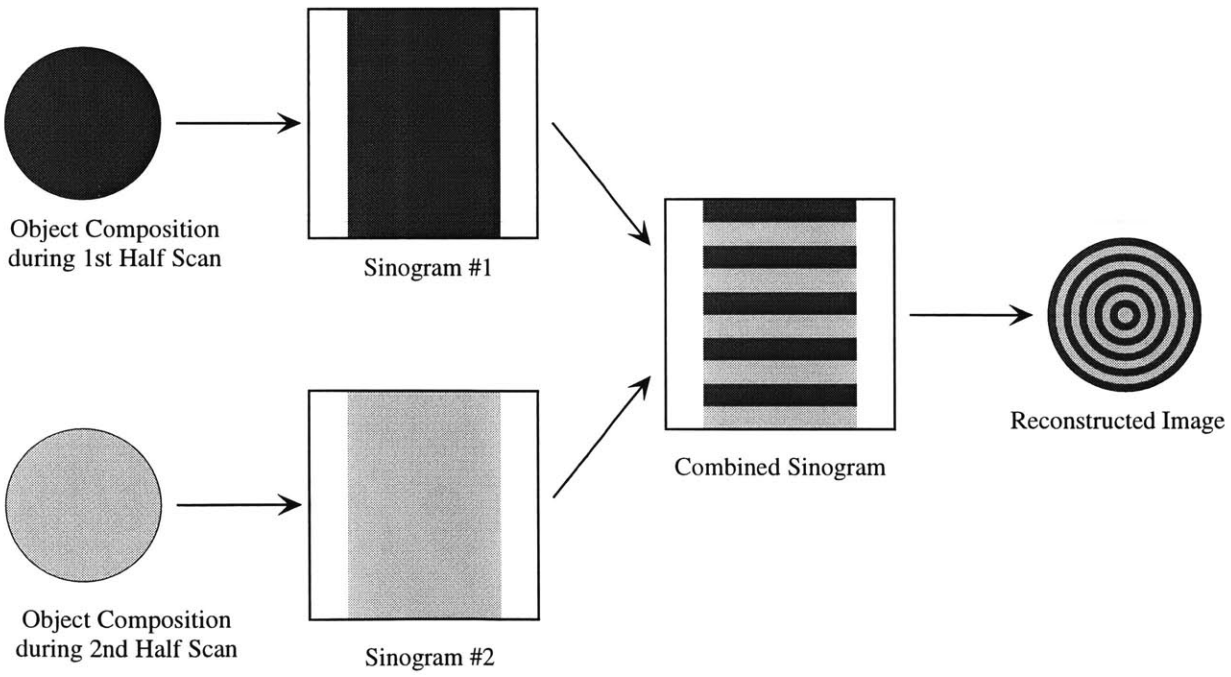

Figure 3-17: Example of how ring artifacts occur from a compositional variation in object density during data acquisition.

Chapter 4 Solidification Experiments: Aluminum Alloys

4.1 Experiment Design

On both qualitative and quantitative levels, the CT sensor is successful in tracking the liquid/solid interface as it evolves in a pure aluminum casting. However, aluminum in its pure form does not enjoy widespread commercial usage. It is soft and ductile, and when annealed, exhibits only about one-fifth the strength of hot-rolled steel. Pure aluminum is most commonly used in electrical conduction applications as a replacement for copper. Industrially, one of the many grades of aluminum alloy is most often chosen for structural applications. Aluminum alloys excel over pure aluminum because of increased strength with the advantages of corrosion resistance, light weight, and good conductivity. Because of the economic importance of aluminum alloys, a significant benefit would result from understanding and improving their properties during manufacture. A viable CT-based solidification sensor must not only be able to function when casting pure aluminum, but more importantly, be able to monitor the complex mechanics of a solidifying aluminum alloy.

Unlike a pure metal, an alloy solidifies over a range of temperatures. A comparison of the time-temperature curve for a pure metal and an alloy is shown in Figure 4-1. Solidification begins when the temperature reaches the liquidus temperature and continues until the solidus temperature. This temperature range is referred to as the mushy zone. As shown in Figure 4-2, the mushy zone is a region of varying density between the molten and solid phases of the metal. The exact composition of the mushy zone is dependent on the particular alloy and can be determined from the alloy's phase diagram. For complicated alloys consisting of four or more alloying elements, the phase diagram is not readily reproducible. However, in simple alloys, such as a binary system where only one alloying element is added, the phase diagram can be readily visualized. Given a binary alloy, the desired solidification conditions can be easily produced by varying the concentration of the two elements.

Three experiments were conducted to test the performance of the CT sensor on aluminum alloy solidification. The first two experiments used two binary aluminum-copper alloys. The first Al-Cu alloy was hypoeutectic and would exhibit a large mushy zone during solidification. The second Al-Cu alloy was at the eutectic point and would exhibit no mushy zone during solidification. The third solidification experiment used a commercial grade aluminum alloy, 6061. The 6061 alloy is composed of four alloying elements: magnesium, silicon, copper, and chromium. The alloy exhibits a large mushy zone during solidification, approximately 70°C. These three alloys were chosen because they feature three different

compositions and three different solidification behaviors. They provided a good range of test conditions for the CT sensor.

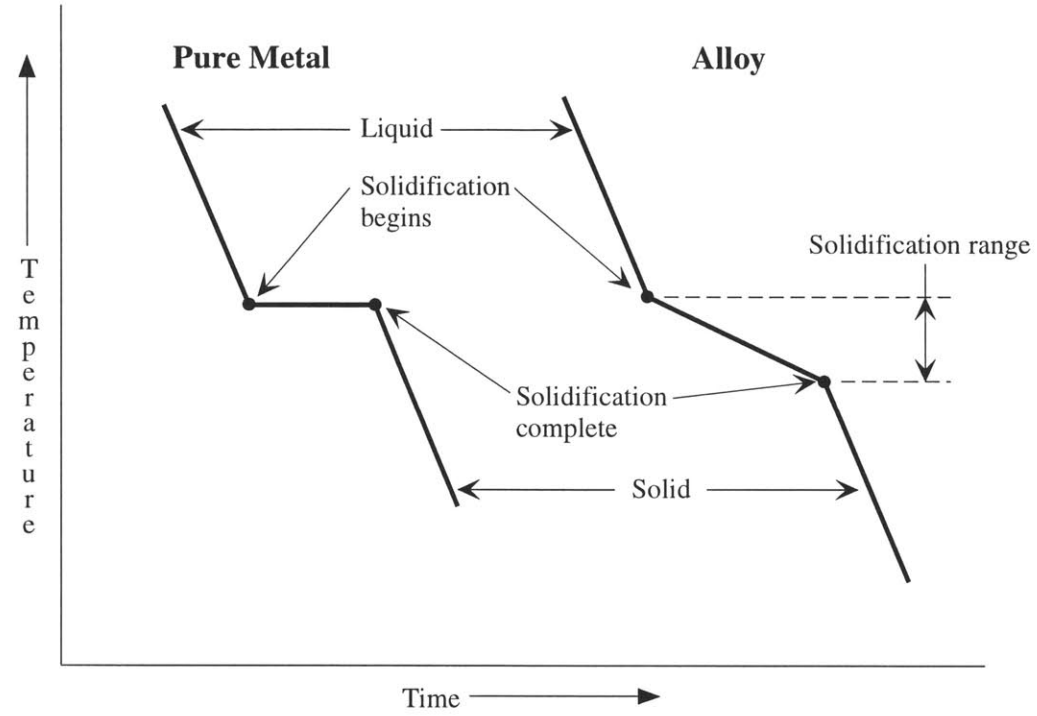

Figure 4-1: Time-temperature curve for a pure metal and an alloy.

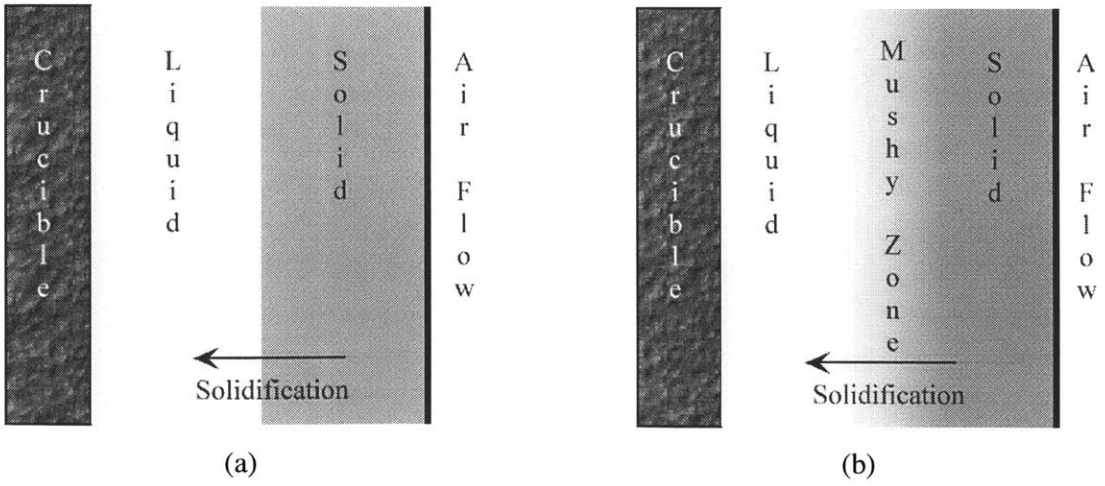

Figure 4-2: (a) Solidification behavior of a pure metal. (b) Solidification behavior of an alloy.

4.2 Binary Aluminum Alloys

Binary alloys are often used in laboratory experiments because the solidification mechanism can be readily altered by changing the amount of the two constituents. For example, Diao and Tsai (1993) used Al-Cu alloys to model the solute redistribution in the mushy zone. Glicksman et al. (1992) used various Al-Cu alloys to model microstructural phase coarsening kinetics. In the present work, an Al-Cu binary system was chosen because its solidification behavior is ideal for testing the CT sensor. The phase diagram for an Al-Cu binary system is shown in Figure 4-3. As mentioned previously, two Al-Cu compositions were used, hypoeutectic and eutectic.

In the hypoeutectic case (5.7wt.%<Cu<33.2wt.%), the alloy solidifies from the liquid state by passing through the mushy zone. The mushy zone consists of the liquid phase plus the α-phase solid. For the Al-Cu system, the α-phase solid is pure aluminum. When the temperature reaches the eutectic horizontal, 527°C, the remaining alloy solidifies as the eutectic microconstituent, a combination of the α-phase solid and $CuAl_2$, the θ-phase solid. The exact proportion of the α- and θ-phases is dependent on the original Al-Cu concentration. The final solidified microstructure consists of pure aluminum crystals surrounded by the eutectic microconstituent. In the eutectic case (Cu=33.2wt.%), the alloy solidifies at a discrete temperature, 527°C. At this temperature, both the α-phase and the θ-phase solidify simultaneously from the liquid, producing a microstructure consisting of roughly equal portions of Al and $CuAl_2$.

For the solidification experiment, the two binary aluminum alloys were produced by combining pure aluminum (99.7% pure) with an aluminum-copper master alloy (50%-50% by weight). The components were melted and mixed in an induction furnace. The intended concentration of the hypoeutectic alloy was 15% copper by weight, roughly midway between the solid-solubility point and the eutectic point of the Al-Cu phase diagram. For the purpose of the experiment, a wide mushy zone would result due to the large temperature difference between the liquidus and solidus point, approximately 80°C. The intended concentration of the eutectic alloy was 33% copper by weight, at the eutectic point of the Al-Cu phase diagram. This would result in a discrete solidification temperature and no mushy zone.

After the two binary alloys had been produced, a 20g sample was extracted from each for compositional analysis. X-ray fluorescence spectroscopy revealed that the actual composition of the hypoeutectic alloy by weight was 88.35% aluminum, 11.23% copper, and 0.42% miscellaneous elements. The actual composition of the eutectic alloy by weight was 69.97% aluminum, 29.74% copper, and 0.29% miscellaneous elements. Although the actual copper concentrations were approximately 3-4% lower than the target values, the final compositions were acceptable for the purpose of these experiments.

The two binary alloy solidification experiments were conducted similarly to the pure aluminum experiment discussed in Section 3.3. For each experiment, approximately 5 kg of the particular Al-Cu alloy was melted in the crucible. Unlike the pure aluminum experiment however, only a single thermocouple monitored the temperature in the melt. During the course of the experiment, a CT image was acquired approximately once every minute and the thermocouple reading was recorded once every second.

The experiments lasted between 120 and 140 minutes. The experiments were terminated when the aluminum alloy solidified and reached a temperature of approximately 450°C, well below the eutectic temperature of 547°C. During the course of the hypoeutectic solidification experiment, 114 CT images were acquired. For the eutectic solidification experiment, 96 CT images were acquired. A single CT image was also acquired once each of the aluminum alloys had reached room temperature.

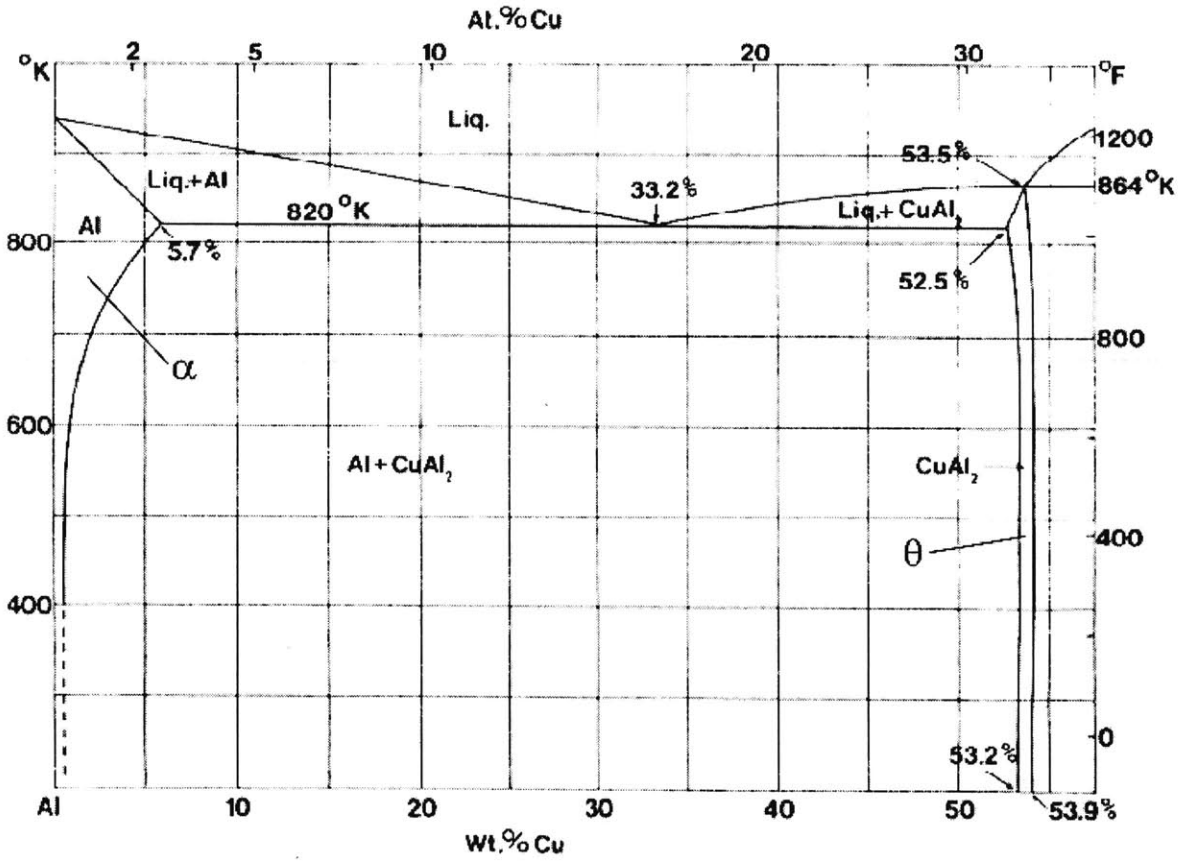

Figure 4-3: Binary phase diagram for aluminum and copper (Mondolfo, 1976).

4.2.1 CT Results – Hypoeutectic Alloy

Figure 4-4 shows a selection of CT images from the hypoeutectic aluminum solidification experiment. The nine images were acquired over 138 minutes. The difference image technique amplified any density changes. Each image is 512 by 512 pixels in size, corresponding to a scaling of 0.53 mm/pixel. The solidification behavior of the hypoeutectic alloy shown in Figure 4-4 differs dramatically from that of the pure aluminum shown in Figure 3-11. This is to be expected. Unlike pure aluminum, the hypoeutectic alloy solidifies over a range of temperatures. As seen in the phase diagram in Figure 4-3, Al-11.2wt.%Cu solidifies over a range from approximately 630°C to 527°C. Over this region, the alloy experiences a slow increase in density as it evolves through the mushy zone. The density change from liquid to mushy zone to solid is so gradual that the CT images do not show any visible solidification front. Instead, the CT images indicate a very progressive increase in density over time. This is manifested as a gradual brightening in pixel intensity over time. The change is quite obvious when Figure 4-4i is compared to Figure 4-4a. However, if the time interval between two images is short, such as the 17 minutes between Figures 4-4c and 4-4d, any density change is difficult to identify.

Qualitatively, the large mushy zone present in the solidification of some hypoeutectic alloys poses a problem. Mere visual inspection of a CT image does not provide much significant information about the solidification process. However, quantitative information can be extracted by employing a region-of-interest (ROI) analysis. Using an absolute density scale, a small ROI was defined near the thermocouple position in each image, as shown in Figure 4-5a. The density within this ROI was then measured. The same region of interest (size, shape, and location) was used for every image. The result is an experimental measure of the density in a single small region within the aluminum, plotted over the time period of the solidification experiment. The ROI lies near the thermocouple so that the temperature measurement would be as nearly as possible representative of the temperature in the ROI. Figure 4-5b shows the computed density within the ROI as a function of time. The temperature at the thermocouple is also plotted.

By plotting the results of the ROI analysis, the gradual density change that the hypoeutectic underwent during solidification is easily seen. The density rises linearly from a value of 2.7 g/cm^3 at 780°C to a final value of 2.97 g/cm^3 at 440°C. The density values are near those expected for an Al-11.2wt.%Cu alloy (Mondolfo, 1976). A second ROI analysis determined how the solidification front moved within the casting. Three ROIs were defined within the CT image–one near the cooling tube, one in the interior of the alloy, and one near the crucible wall. The locations of the three ROIs are shown in Figure 4-6a. The density within each ROI was measured for each CT image. The results are shown in Figure 4-6b. It was expected that the hypoeutectic sample would solidify preferentially from the interior

of the casting towards the exterior of the crucible, as the pure aluminum experiment had done. However, as indicated in Figure 4-6b, the density increase in each ROI began nearly simultaneously. This implies that the entire alloy, or at least the section observed via CT imaging, solidified uniformly.

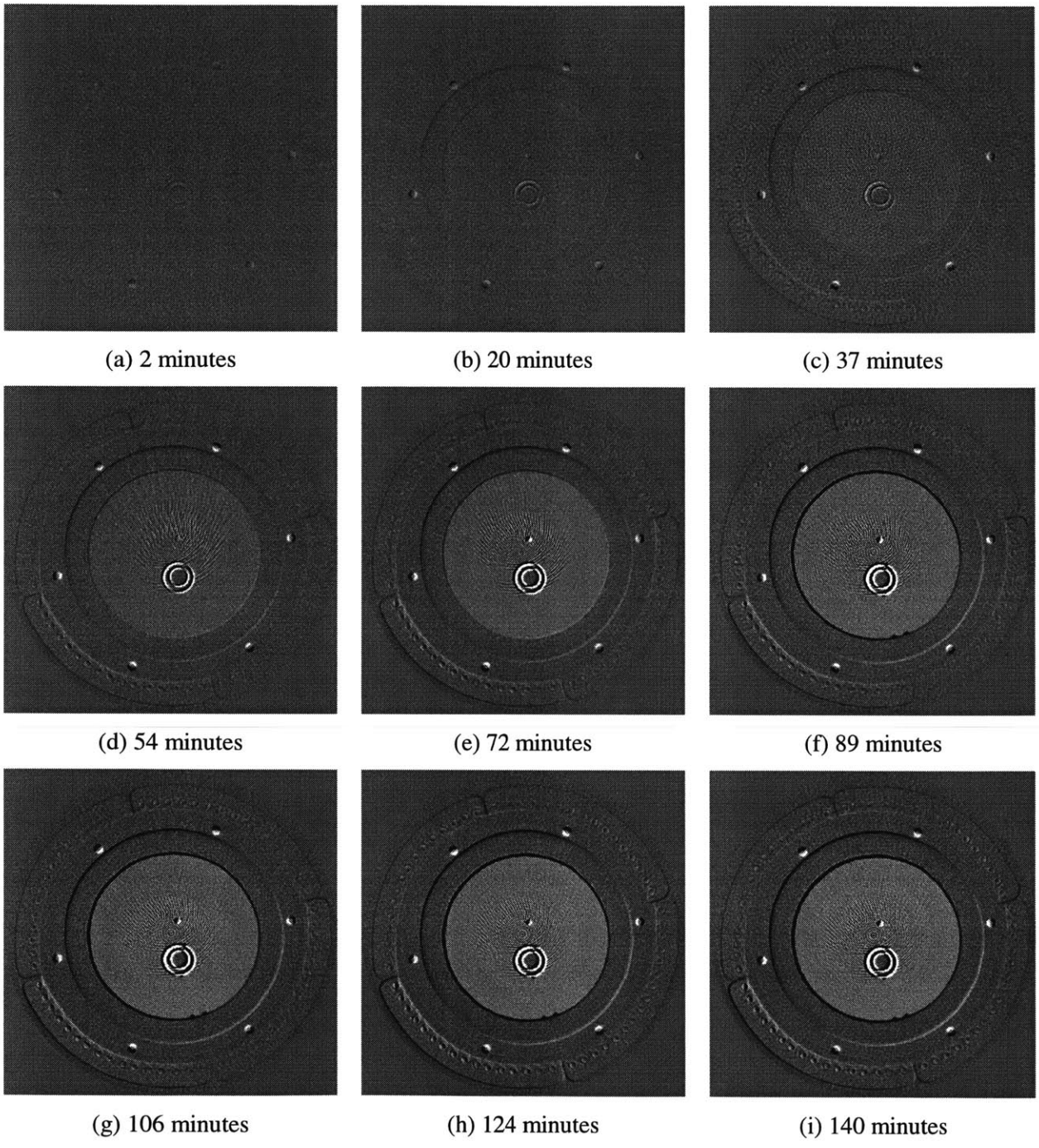

(a) 2 minutes (b) 20 minutes (c) 37 minutes

(d) 54 minutes (e) 72 minutes (f) 89 minutes

(g) 106 minutes (h) 124 minutes (i) 140 minutes

Figure 4-4: Nine difference images showing the evolution of solidification in the hypoeutectic aluminum over a period of 138 minutes, from (a) time=2 minutes to (i) time=140 minutes.

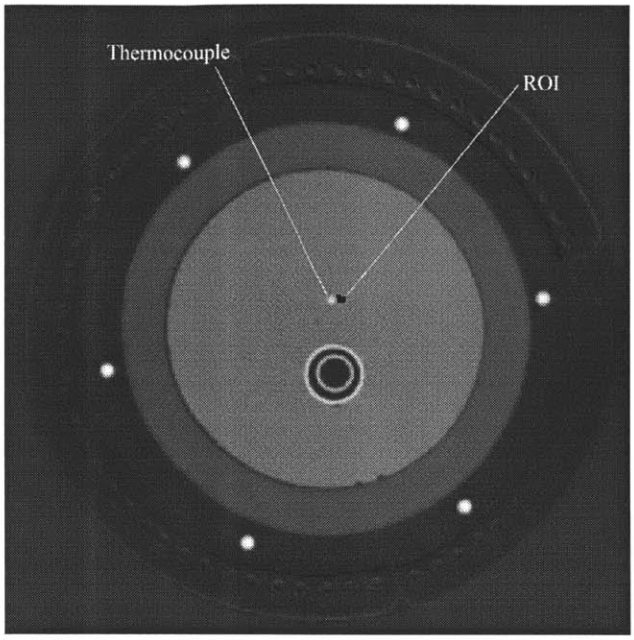

(a)

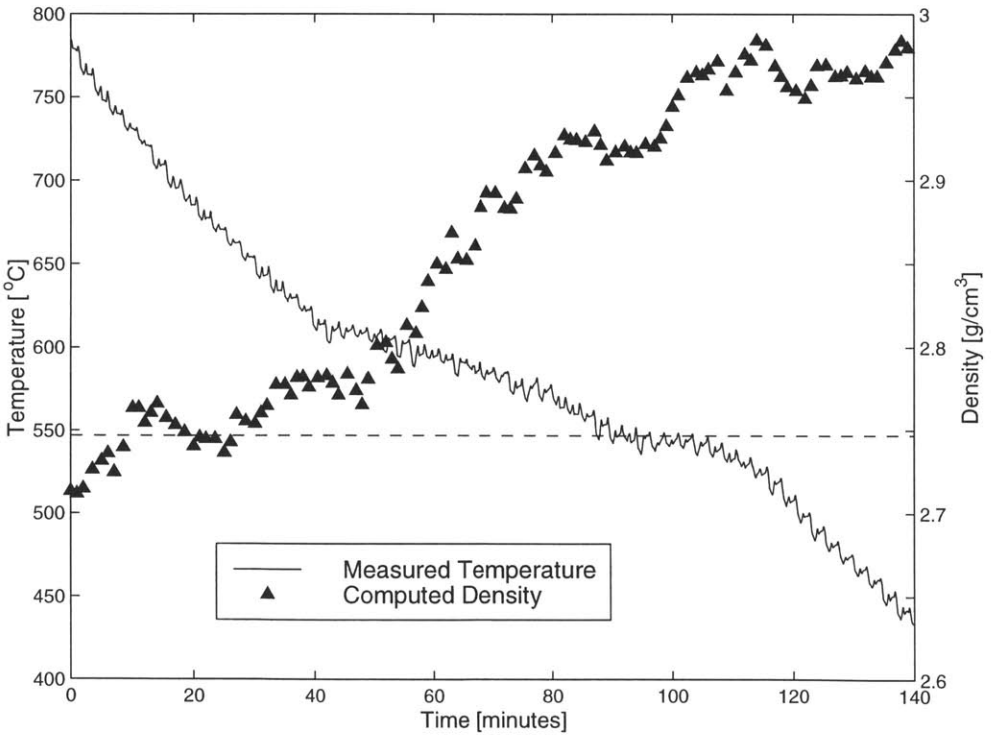

(b)

Figure 4-5: (a) Location of region of interest (ROI) in the CT image. (b) Computed density and temperature in the ROI plotted over the time of the hypoeutectic solidification experiment.

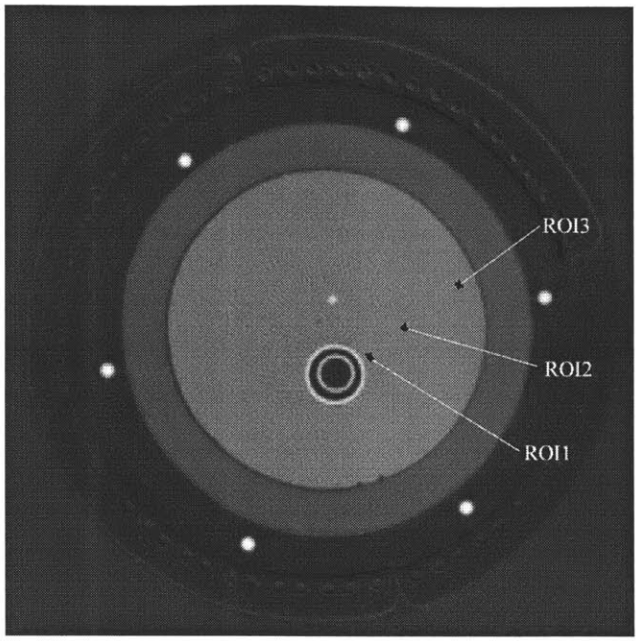

(a)

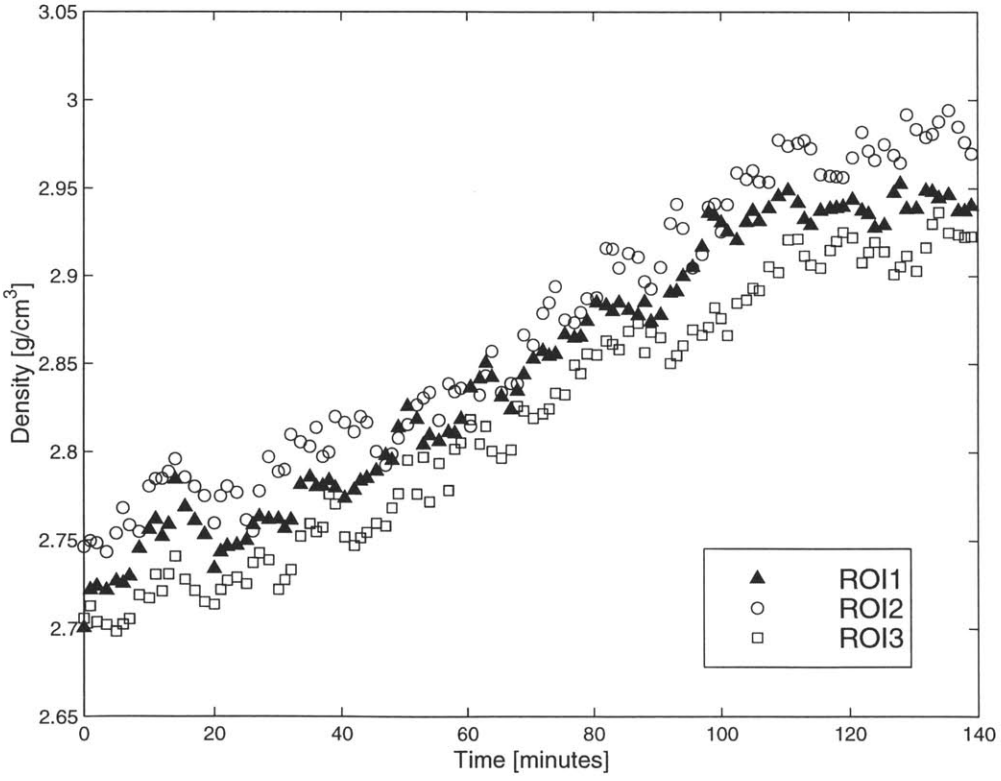

(b)

Figure 4-6: (a) Location of three ROIs in the CT image. (b) Computed density in each of the three ROIs plotted over the time of the hypoeutectic solidification experiment.

4.2.2 Micrograph Results – Hypoeutectic Alloy

A metallographic analysis of the post-solidification microstructure was performed to validate the density measurements derived from the CT image of the hypoeutectic alloy. This required cooling the aluminum alloy to room temperature after the solidification experiment. A CT image was then acquired and reconstructed. That CT image is shown in Figure 4-7. The casting was removed from the crucible and a slice was extracted along the same horizontal plane as that of the CT image. This sample was then sectioned into four pieces to facilitate the metallographic analysis. Figure 4-8 shows a photograph of the hypoeutectic aluminum sample cut from the casting.

For the metallographic analysis, one wedge of the sectioned aluminum sample was polished to a 3 μm surface finish and etched using Poulton's Reagent (60% HCl, 30% HNO_3, 5% HF, 5% H_2O). The sample was then examined under a microscope at a magnification of 82.5x. Micrographs were taken at six radial positions along the etched sample, as indicated in the photograph in Figure 4-9. Figure 4-10 shows the six micrographs. The resultant microstructure of the aluminum sample is consistent with that expected from a hypoeutectic alloy. In each micrograph, the geometric crystal shape of the primary α-phase (pure Al), indicated by the dark regions, is clearly visible. The eutectic microconstituent, composed of the secondary α-phase and the θ-phase ($CuAl_2$), indicted by the light regions, is also apparent.

An experimental measurement of the density variation in the alloy was made by calculating the amount of each phase present in each of the micrographs. For a binary alloy consisting of an α and θ phase, the relative amount of the α-phase in a specimen can be expressed in terms of the mass ratio, M (Raynor, 1970):

$$M = \frac{V_\alpha \rho_\alpha}{(V_\alpha + V_\theta)\rho_s} \tag{4.1}$$

where V_α is the volumetric amount of the α-phase constituent, V_θ is the volumetric amount of the θ-phase constituent, ρ_α is the density of the α-phase, and ρ_s is the density of the binary specimen. Similarly, the relative amount of the θ-phase can be expressed as:

$$1 - M = \frac{V_\theta \rho_\theta}{(V_\alpha + V_\theta)\rho_s} \tag{4.2}$$

where ρ_θ is the density of the θ-phase. Adding Equations. 4.1 and 4.2 yields:

$$\frac{V_\alpha \rho_\alpha}{(V_\alpha + V_\theta)\rho_s} + \frac{V_\theta \rho_\theta}{(V_\alpha + V_\theta)\rho_s} = 1 \tag{4.3}$$

The total volume of the specimen, V_s, is:

$$V_s = V_\alpha + V_\theta \tag{4.4}$$

Substituting Equation 4.3 into Equation 4.4 yields:

$$\frac{V_\alpha \rho_\alpha}{V_s \rho_s} + \frac{V_\theta \rho_\theta}{V_s \rho_s} = 1 \tag{4.5}$$

Quantitative observations of planar metallographic samples have shown that the volume ratio is equal to the area ratio (Rostoker and Dvorak, 1965):

$$\frac{V_\alpha}{V_s} = \frac{A_\alpha}{A_s} \tag{4.6}$$

where A_α is the planar area of the α-phase in the micrograph and A_s is the total area of the micrograph. Substituting Equation 4.6 into Equation 4.5 yields:

$$A_\alpha \rho_\alpha + A_\theta \rho_\theta = A_s \rho_s \tag{4.7}$$

or

$$\rho_\alpha f_\alpha + \rho_\theta f_\theta = \rho_s \tag{4.8}$$

where f_α and f_θ are the fractional area of the α- and θ-phases in the micrograph, respectively. For an Al-Cu binary alloy, the density of the α-phase (pure Al) is 2.70 g/cm^3. The density of the θ-phase ($CuAl_2$) is 4.34 g/cm^3 (Mondolfo, 1976). In the present analysis, the fractional area of the two phases was determined by taking a binary threshold of each micrograph and measuring the area of the resulting black and white regions. Having measured the fractional area for α- and θ-phases, the density of the aluminum alloy was then determined using Equation 4.8. Table 4-1 shows these results. Based on this micrograph analysis, the density across the aluminum alloy was found to be relatively uniform with a difference of only 0.073 g/cm^3 between the highest and lowest measurement. The expected density for an Al-11.2wt.%Cu alloy is 2.95 g/cm^3 (Mondolfo, 1976).

Table 4-1: Results of micrograph analysis on the hypoeutectic aluminum sample.

Position No.	Radial Distance [mm]	Al-phase Fractional Area	$CuAl_2$-phase Fractional Area	Specimen Density [g/cm^3]
1	14.5	0.867	0.133	2.919
2	24.3	0.911	0.089	2.846
3	32.0	0.887	0.113	2.885
4	39.0	0.889	0.111	2.881
5	45.7	0.878	0.122	2.899
6	52.8	0.908	0.092	2.850

Density as a function of radial position in the CT image was measured for comparison. The center of the airflow tube was used as the center of the sample. The average density was calculated inside a ROI measuring 4 pixels by 8 pixels (2.1 mm by 4.2 mm). The center of the ROI was moved radially outward, from the center of the airflow tube to the outside of the crucible, in one pixel increments (0.53 mm). The measurement was performed over the same area in the CT image as that of the sectioned sample used for the metallographic analysis. The density as a function of radial position is shown in Figure 4-11. The density measurement from the CT image is relatively uniform across the sample, in agreement with the result from the micrograph analysis. Any variations are attributable to the ring artifacts discussed in Section 3.5.

As an additional verification of the uniformity of the sample, hardness measurements were performed on the sectioned sample using the Rockwell F standard (1.58 mm dia. ball, 60 kg load). Two hardness measurements were recorded at each of the six locations where a micrograph was taken. The first hardness measurement was taken at the same position as the micrograph. The second measurement was taken at a position offset tangentially by approximately 3 mm. The measurements were then converted to the Brinell hardness scale (ASTM Standards, 1997). Figure 4-12 shows the hardness of the alloy sample as a function of radial position.

The hardness of a material had been subject to a variety of definitions. Hardness may not be a fundamental property of a material, but rather a function of other properties such as yield strength, work hardening, tensile strength, modulus of elasticity, etc. (Avallone and Baumeister, 1987). In the context of this work, hardness measurements are loosely related to the density of the aluminum alloy. In particular, if a significant density difference was present due to variations in the copper concentration, hardness measurements reflect this fact. However, hardness measurements performed on the hypoeutectic specimen were relatively uniform across the sample. These results corroborate the density results from the CT image and micrograph analyses.

It is worthwhile to note that during non-equilibrium solidification of hypoeutectic alloys, a compositional variation as a function of position is often encountered. This variation occurs because of improper diffusion in the growth of the α-phase crystals. The result is a rejection of the eutectic microconstituent that leads to an elevated copper concentration in areas that solidify last (Guy, 1959). However, this condition was not encountered in the present case. Based on a qualitative comparison of the six micrographs, there is little apparent variation in the sample microstructure as a function of position. The microstructure at a radial position of 14.5 mm is very similar to that at 52.8 mm. This indicates that solidification was relatively uniform and occurred slowly enough to allow for proper solute diffusion in the growing crystals. However, this characteristic cannot be generalized to the entire casting since only one sample slice was examined.

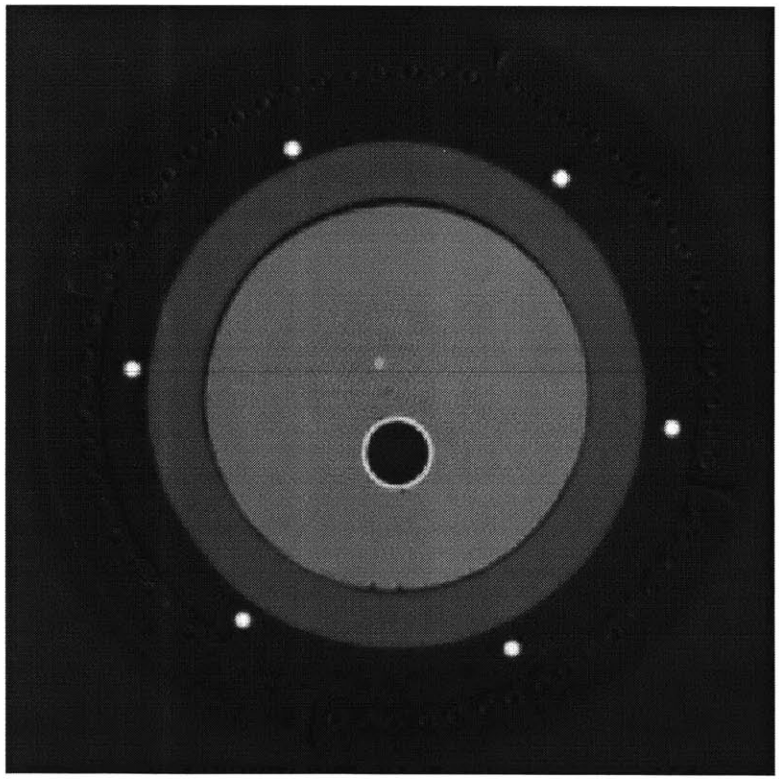

Figure 4-7: CT image of the hypoeutectic aluminum at room temperature.

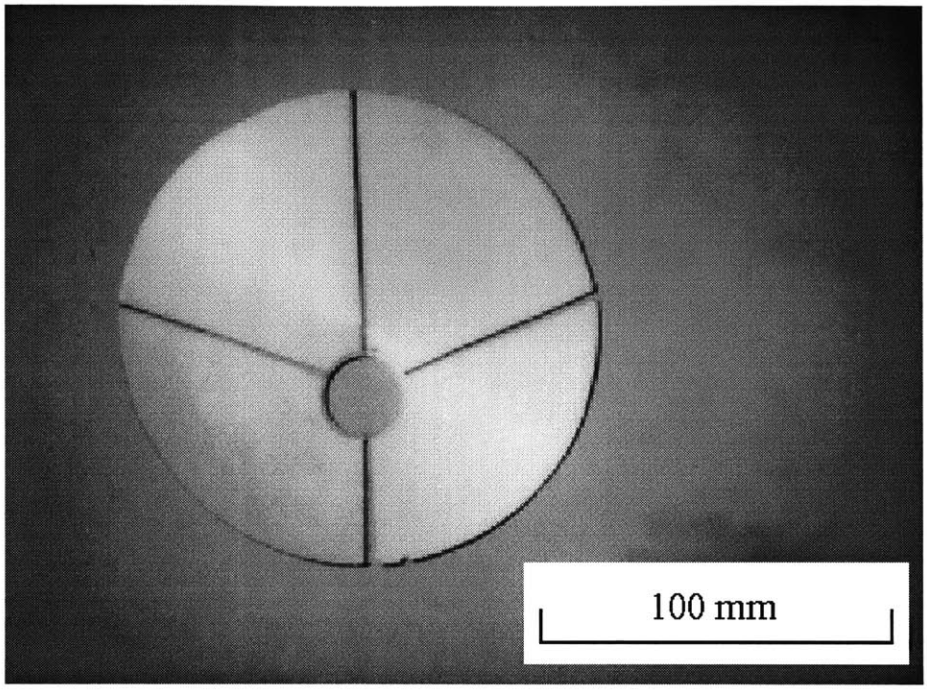

Figure 4-8: Photograph of the hypoeutectic aluminum sample sectioned at the same plane as the CT image. The sample has been cut into four pieces for micrograph analysis.

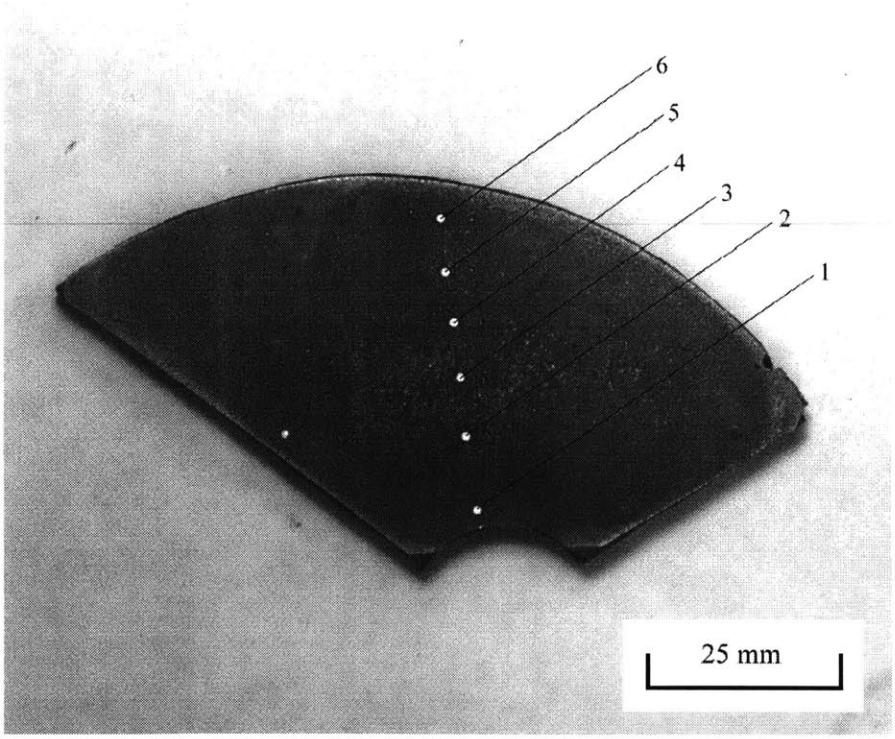

Figure 4-9: Etched sample of the hypoeutectic aluminum. The numbered positions indicate the location where micrographs were taken.

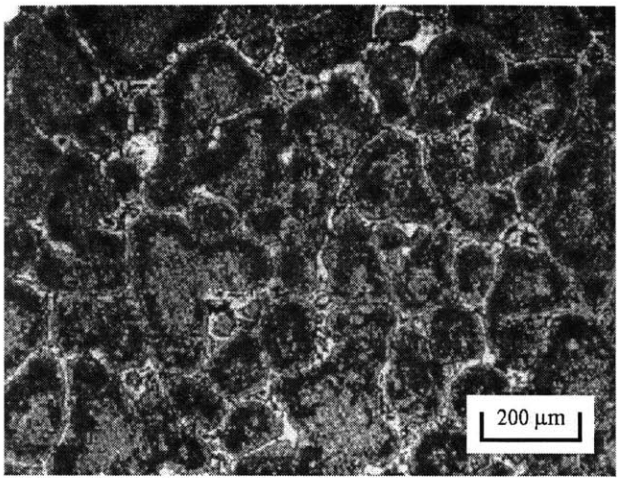

(a) 14.5 mm from center

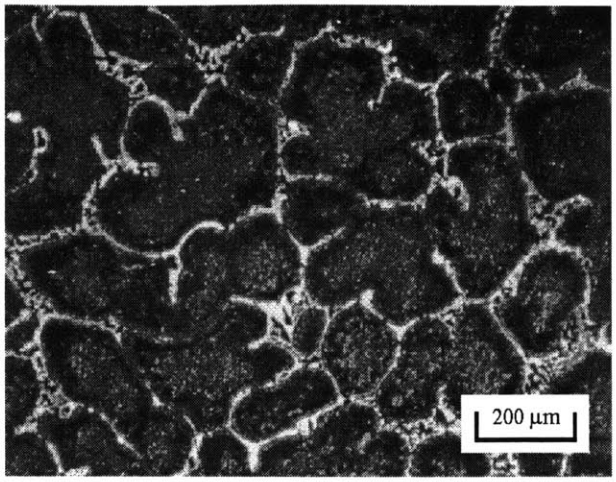

(b) 24.3 mm from center

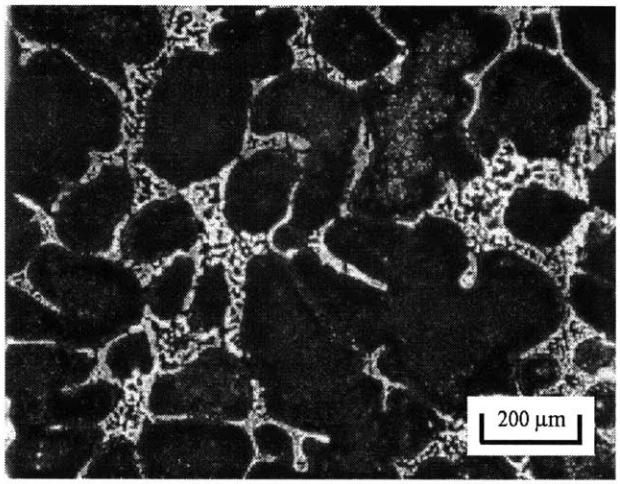

(c) 32.0 mm from center

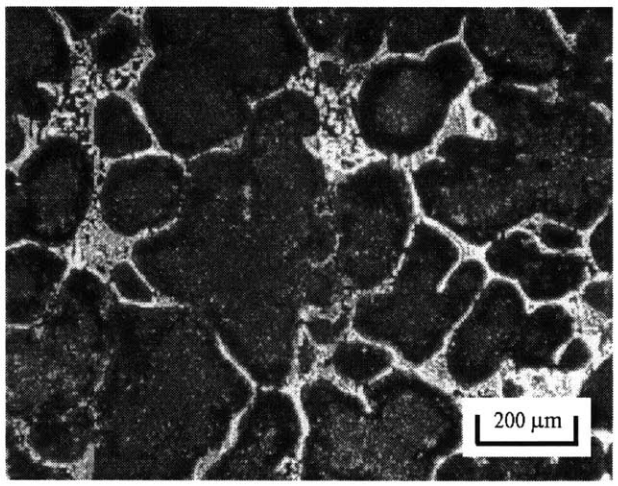

(d) 39.0 mm from center

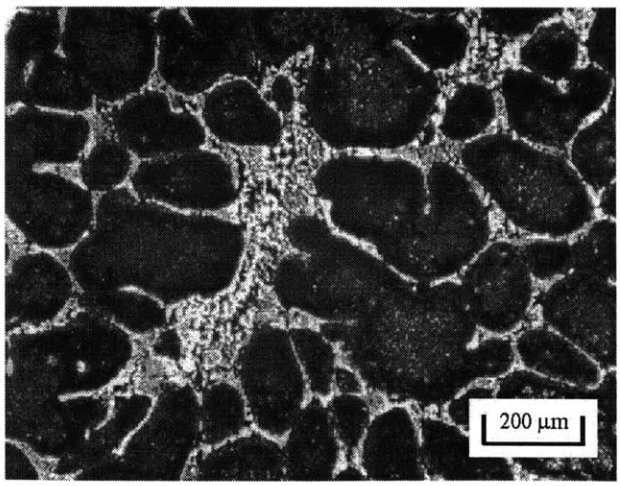

(e) 45.7 mm from center

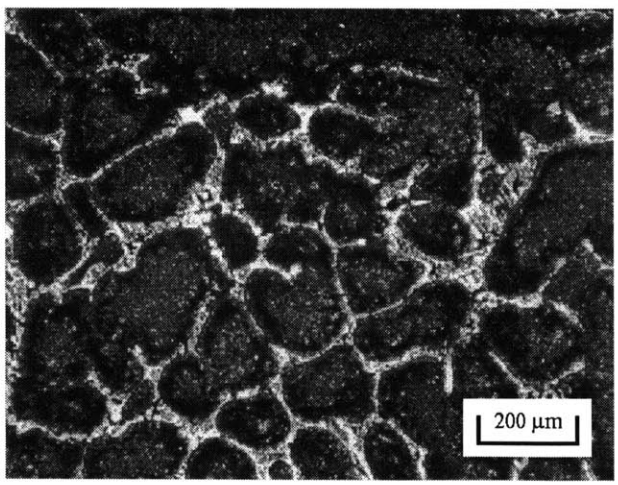

(f) 52.8 mm from center

Figure 4-10: (a)-(f) Micrographs of the hypoeutectic sample taken at six different positions from the center of the airflow tube.

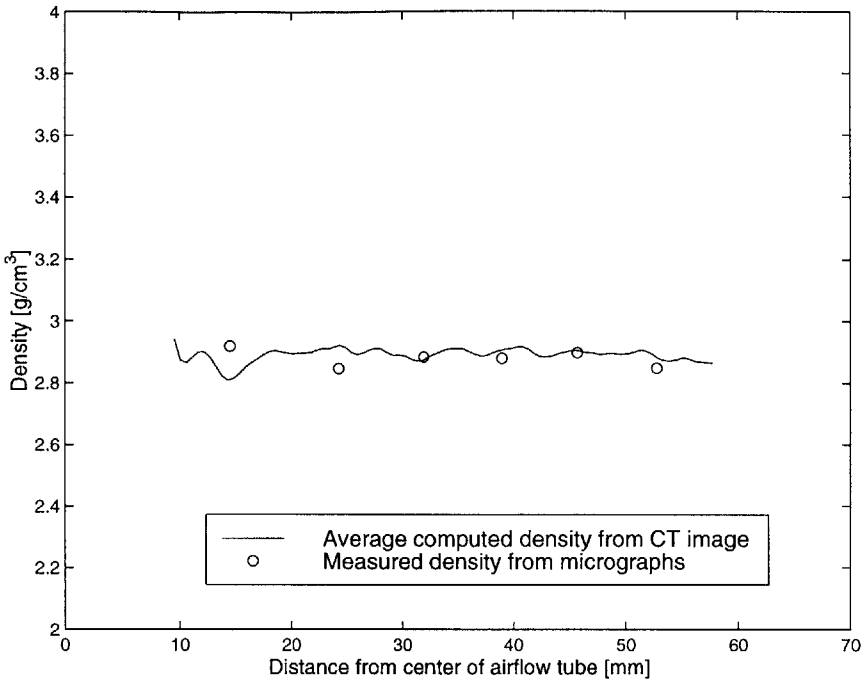

Figure 4-11: Density vs. radial position across the hypoeutectic aluminum sample.

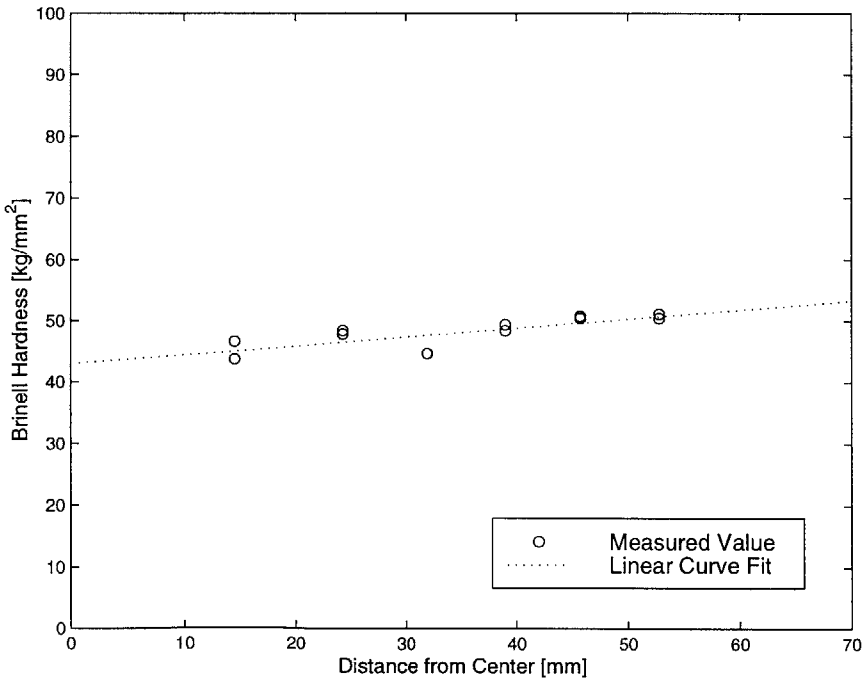

Figure 4-12: Hardness vs. radial position across the hypoeutectic aluminum sample.

4.2.3 CT Results – Eutectic Alloy

Figure 4-13 shows a selection of CT images from the eutectic aluminum solidification experiment. The nine images were acquired over 70.1 minutes. Each image is 512 by 512 pixels in size, corresponding to a scaling of 0.53 mm/pixel. Qualitatively, the eutectic alloy solidified similarly to that of pure aluminum. A discrete solidification front developed around the cooling tube after 48.3 minutes (Figure 4-13a). A secondary solidification front formed around the exterior of the casting and began moving inward (Figure 4-13b). The dual solidification fronts continued to grow over the next 13 minutes (Figures 4-13c and 4-13d). A large void began to form as the two solidification fronts converged (Figure 4-13e). The void continued to grow and enlarge (Figure 4-13f). After 78.2 minutes, solidification was almost complete (Figure 4-13h). Finally, after 119.2 minutes, the eutectic was completely solid (Figure 4-13i).

These results are not unusual; a eutectic alloy is expected to solidify at a discrete temperature. No mushy zone is present. In the case of an Al-Cu binary alloy, the eutectic temperature is 527°C. Although the CT images do provide qualitative information regarding the evolution of the solidification front, additional quantitative information can be extracted by employing a region-of-interest (ROI) analysis as performed in Sections 3.4.5 and 4.2.2. In a manner identical to that of the hypoeutectic alloy, a small ROI was defined near the thermocouple position, shown in Figure 4-14a. The density within this ROI was measured for each CT image. Figure 4-14b shows the computed density within the ROI as a function of time. The temperature measurement recorded at the thermocouple is also plotted.

Again, the discrete solidification front present in eutectic solidification produces a behavior similar to that of pure aluminum. Over the course of the solidification experiment, the density was categorized into three regimes. In the liquid regime, the alloy was in a molten state with a computed density ranging between 3.22 g/cm^3 and 3.27 g/cm^3. During the transition regime, the solidification front passed through the ROI and the computed density quickly increased from 3.27 g/cm^3 to 3.46 g/cm^3. The transition took approximately 12 minutes. In the solid phase, the alloy continued to cool and the computed density slowly increased from 3.46 g/cm^3 at 70 minutes to 3.50 g/cm^3 at 120 minutes. The computed density values correspond with the expected density for an Al-29.7wt.%Cu alloy (Mondolfo, 1976).

As with the analysis in the hypoeutectic case, a second ROI analysis was used to determine how the solidification front moved within the casting. Because of the dual solidification fronts, two ROIs, rather than three, were defined within the CT image. The first is near the cooling tube and the second is in the interior of the alloy. The locations of the two ROIs are shown in Figure 4-15a. The density within each ROI was measured for each CT image. The results are shown in Figure 4-15b. As expected, this ROI analysis shows that the solidification front moved through ROI1 first. The primary solidification

front was moving from the interior of the casting outwards toward the crucible. The front began to pass through ROI1 at 45 minutes and was finished at 55 minutes. The solidification front then passed through ROI2, beginning at 60 minutes and finishing at 75 minutes. As with the pure aluminum, this phase transformation should be so discrete as to occur over two data points, or roughly 1.3 minutes. However, the phase transformation actually occurred over 10 minutes and 15 minutes for ROI1 and ROI2, respectively. As mentioned earlier, the moving solidification front caused a blurring of its position in the CT image. This fact, when coupled with an ROI of finite area, produced a longer transition period than expected. In addition, the alloy used in this experiment was not a pure eutectic (Al-33.2wt.%Cu). The copper concentration was actually 29.7wt.%, which made the alloy slightly hypoeutectic. As such, a small mushy zone could have been present. This would further explain the continuous rather than discrete rise in density as the solidification front passed through the ROIs.

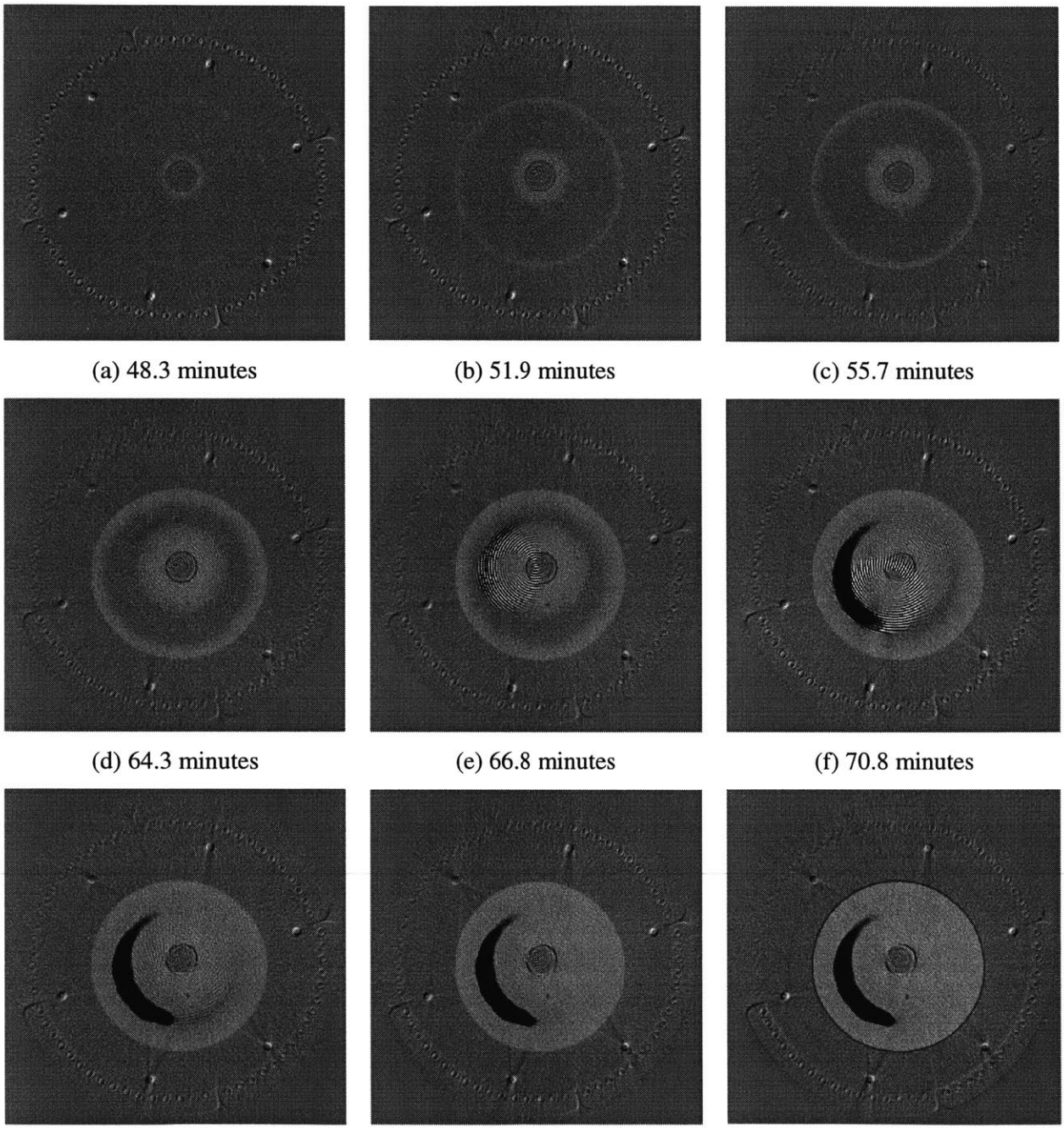

(a) 48.3 minutes (b) 51.9 minutes (c) 55.7 minutes

(d) 64.3 minutes (e) 66.8 minutes (f) 70.8 minutes

(g) 73.2 minutes (h) 78.2 minutes (i) 119.2 minutes

Figure 4-13: Nine difference images showing the evolution of the solidification front in the eutectic aluminum over a period of 70.9 minutes, from (a) time=48.3 minutes to (i) time=119.2 minutes.

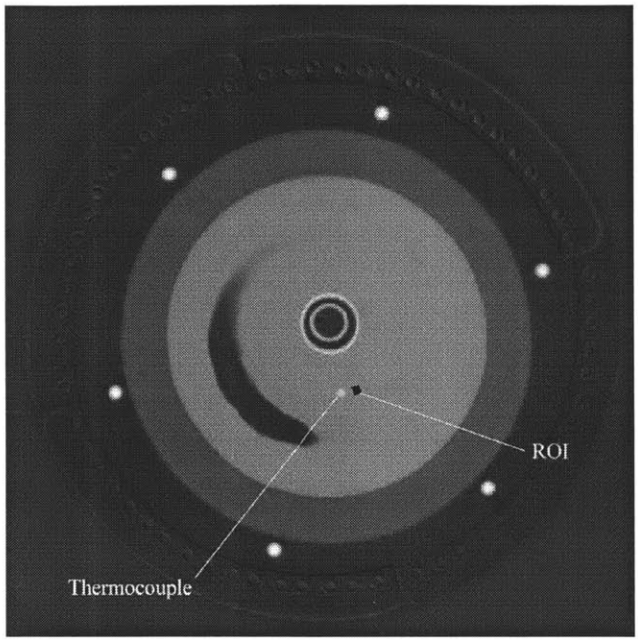

(a)

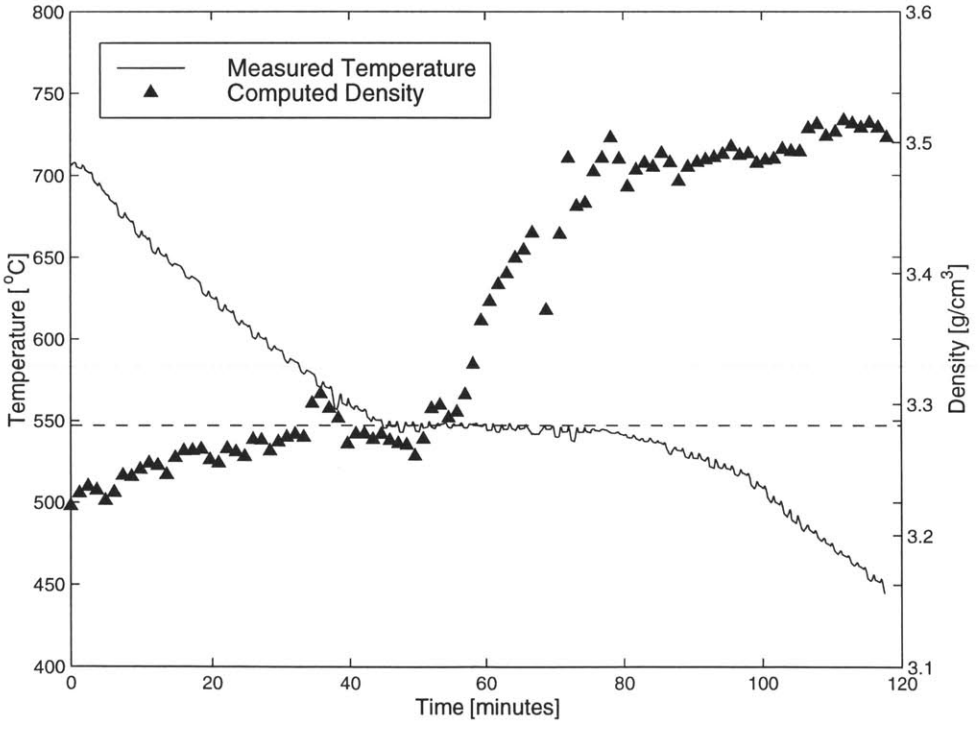

(b)

Figure 4-14: (a) Location of region of interest (ROI) in the CT image. (b) Computed density and temperature in the ROI plotted over the time of the eutectic solidification experiment.

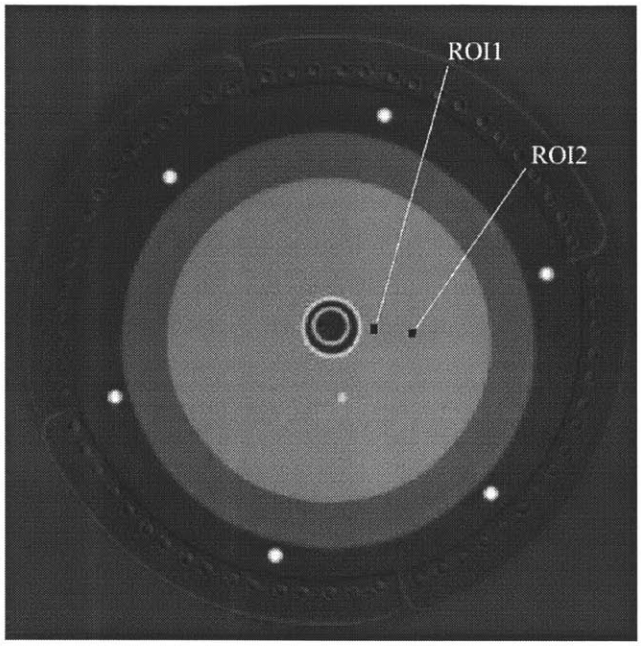

(a)

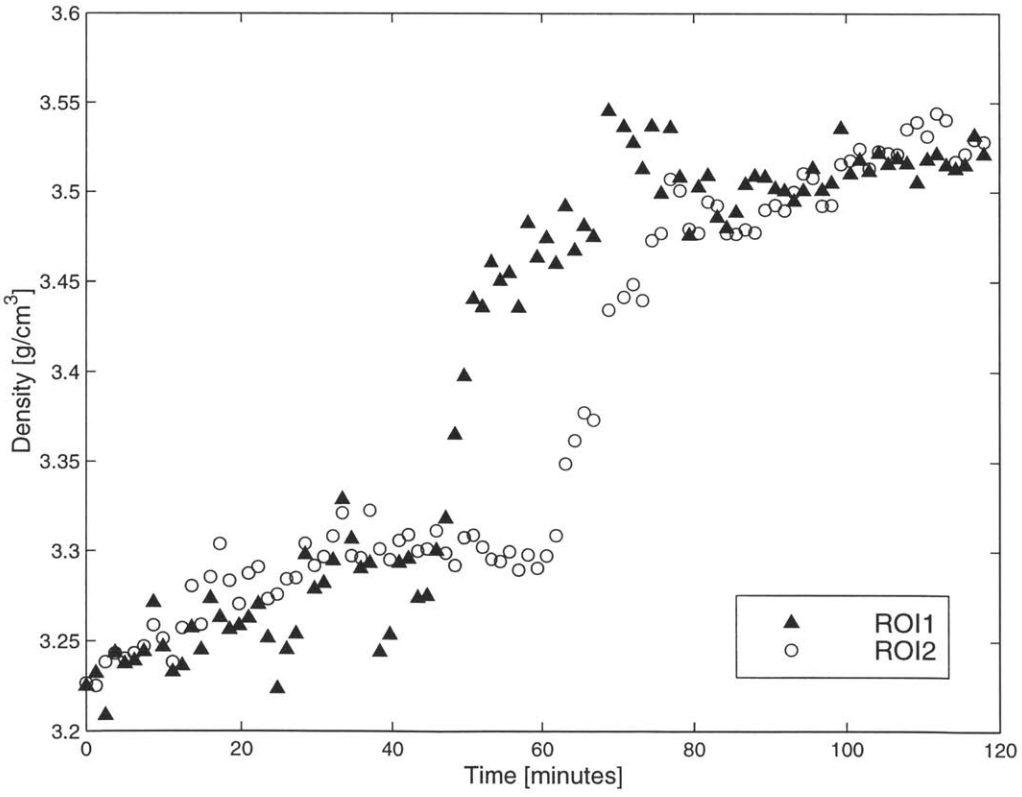

(b)

Figure 4-15: (a) Location of two ROIs in the CT image. (b) Computed density in the two ROIs plotted over the time of the eutectic solidification experiment.

4.2.4 Micrograph Results – Eutectic Alloy

A metallographic analysis of the post-solidification microstructure was performed exactly as in the hypoeutectic case to validate the density measurements derived from the CT image of the eutectic alloy. The CT image of the solidified alloy at room temperature is shown in Figure 4-16. A photograph of the eutectic aluminum sample cut from the casting is shown in Figure 4-17. Micrographs were again acquired at six radial positions along the etched sample, as indicated in the photograph in Figure 4-18. Figure 4-19 shows the six micrographs. The resultant microstructure of the alloy sample is typical of a eutectic alloy. All six micrographs show a colony structure of lamellar eutectic elements. Lamellar solidification is the most common mechanism in Al-Cu alloys because both phases occur in approximately equal volume fractions (Lemkey and Kraft, 1985). Colony structures typically arise under non-unidirectional solidification conditions and during cellular freezing caused by constitutional undercooling (Lemkey and Kraft, 1985). As determined from the CT images of the solidification front evolution, non-unidirectional solidification did occur in this alloy. In addition, constitutional undercooling is typically fueled by impurities in the alloy, which in the present alloy contribute 0.29% by weight.

As with the hypoeutectic case, the fractional area of the two phases was determined by taking a binary threshold of each micrograph and measuring the area of the resulting black and white regions. The density of the eutectic alloy was then determined using Equation 4.8. Table 4-2 shows these results. Based on the micrograph analysis, the density across the alloy was again found to be relatively uniform with a difference of only 0.042 g/cm^3 between the highest and lowest measurement. The expected density for an Al-29.7wt.%Cu alloy is 3.45 g/cm^3 (Mondolfo, 1976).

Table 4-2: Results of micrograph analysis on the eutectic aluminum sample.

Position No.	Radial Distance [mm]	Al-phase Fractional Area	$CuAl_2$-phase Fractional Area	Specimen Density [g/cm^3]
1	16.3	0.485	0.515	3.544
2	25.7	0.504	0.496	3.513
3	38.0	0.506	0.494	3.510
4	43.2	0.511	0.489	3.502
5	51.5	0.494	0.506	3.529
6	59.9	0.502	0.498	3.516

For comparison, the density as a function of radial position was measured in the CT image. The ROI method used to measure the average density was identical to the procedure described in the hypoeutectic case. The measurement was performed over the same area in the CT image as that of the sectioned sample used for the metallographic analysis. Figure 4-20 shows the density as a function of radial position. Again, the density measurement from the CT image is relatively uniform across the sample, in agreement with the micrograph analysis. In addition, the uniform hardness measured across the sample corroborates this result. Figure 4-21 shows the hardness measurements recorded at six radial positions across the alloy sample.

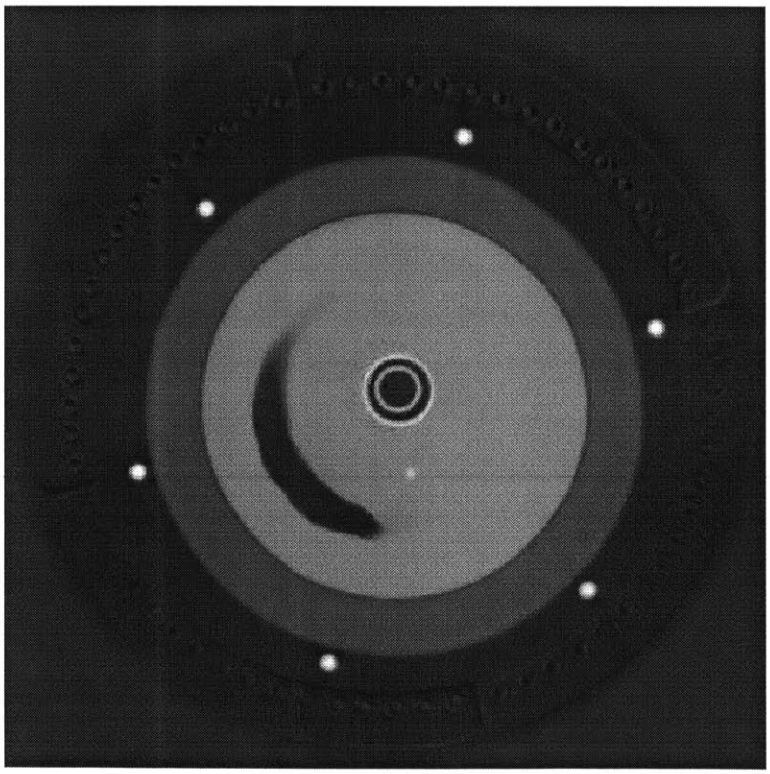

Figure 4-16: CT image of the eutectic aluminum at room temperature.

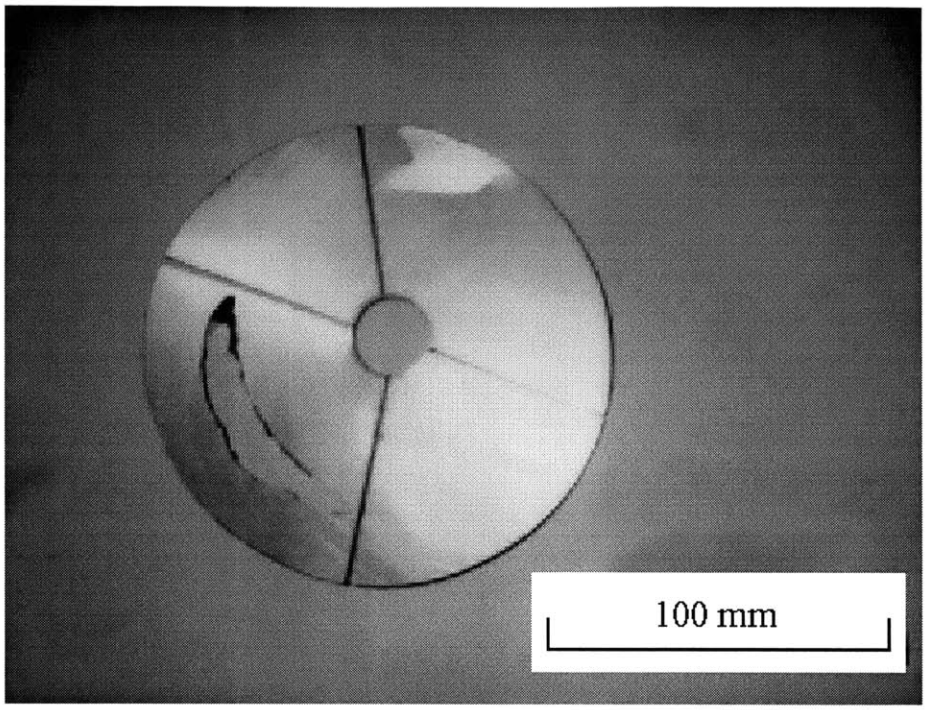

Figure 4-17: Photograph of the eutectic aluminum sample sectioned at the same plane as the CT image. The sample has been cut into four pieces for micrograph analysis.

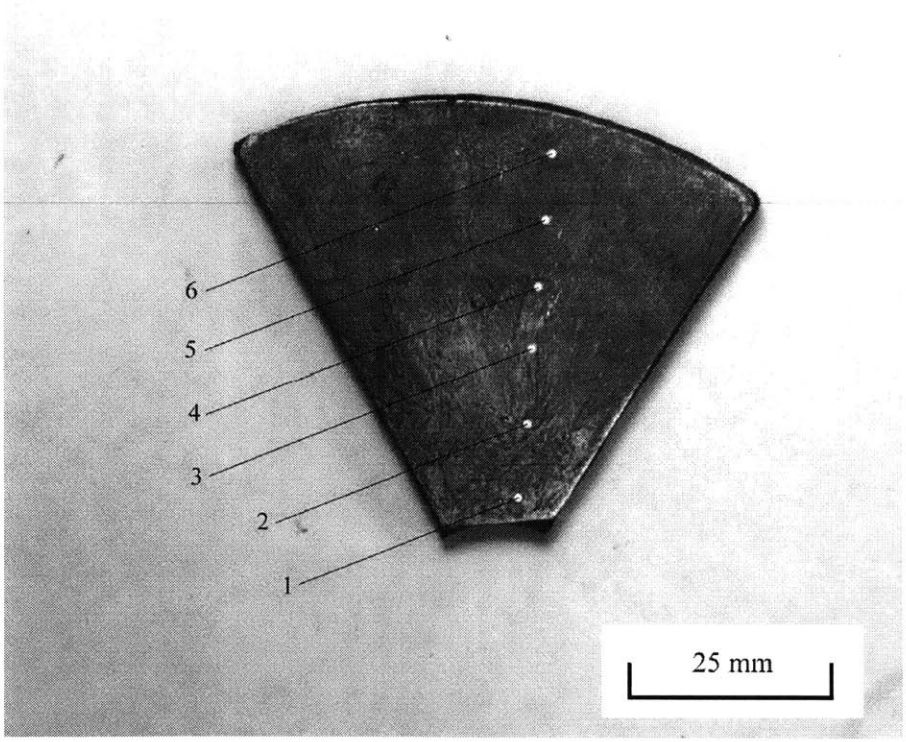

Figure 4-18: Etched sample of the eutectic aluminum. The numbered positions indicate the location where micrographs were taken.

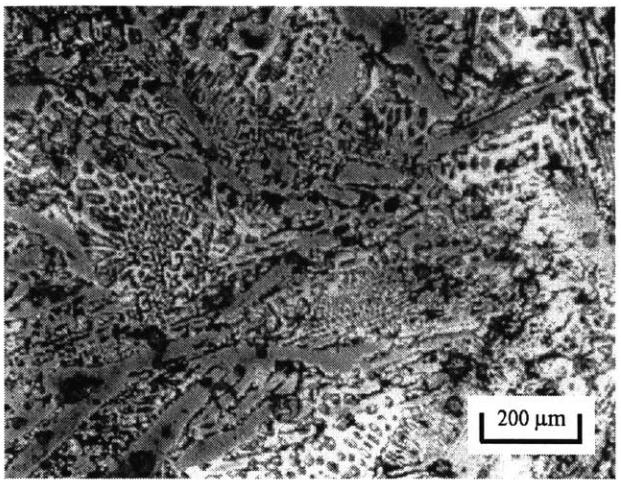

(a) 16.3 mm from center

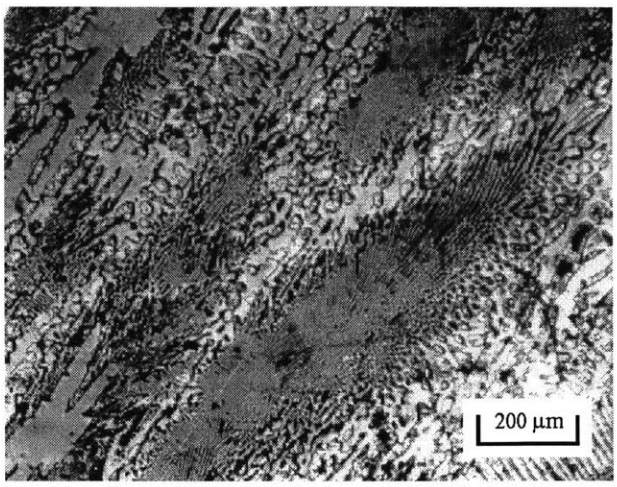

(b) 25.7 mm from center

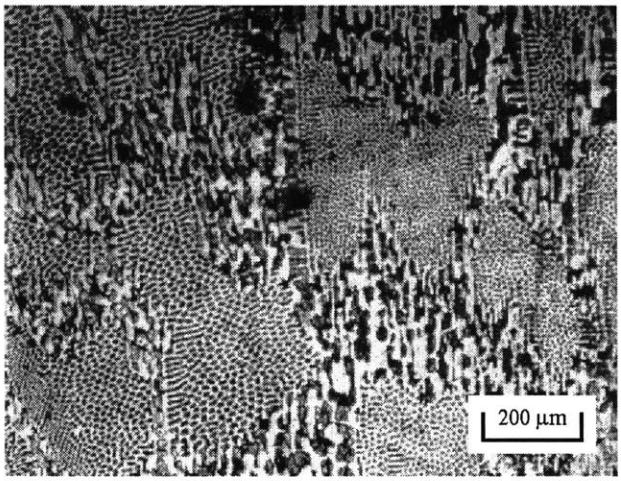

(c) 38.0 mm from center

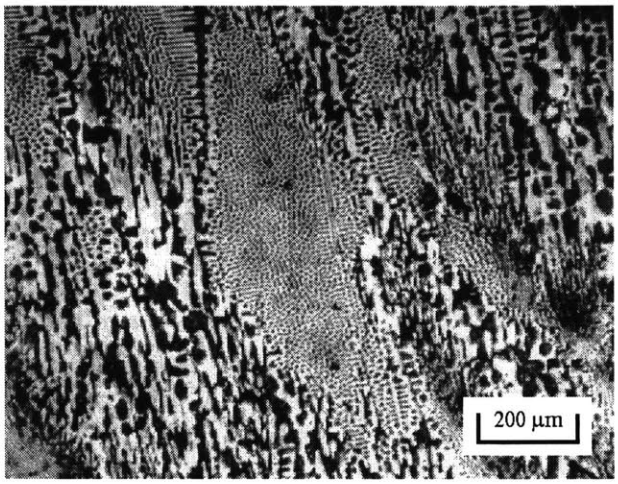

(d) 43.2 mm from center

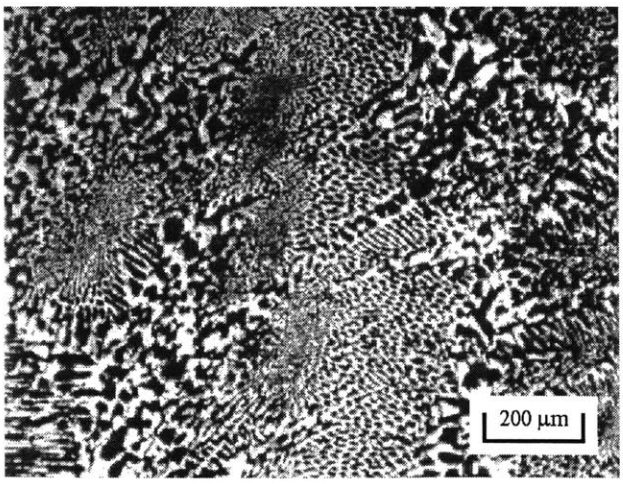

(e) 51.5 mm from center

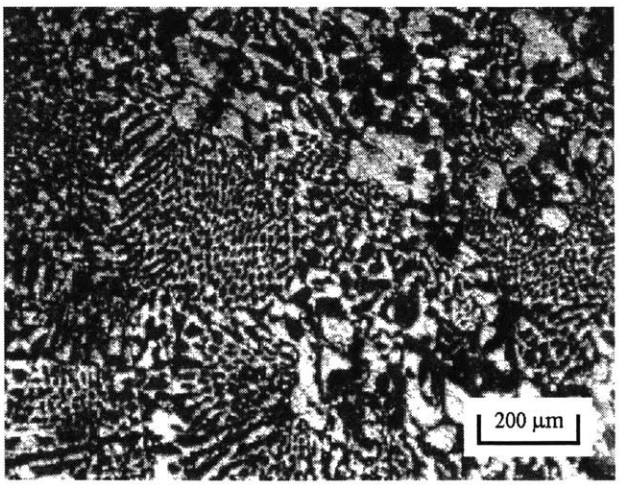

(f) 59.9 mm from center

Figure 4-19: (a)-(f) Micrographs of the eutectic sample taken at six different positions from the center of the airflow tube.

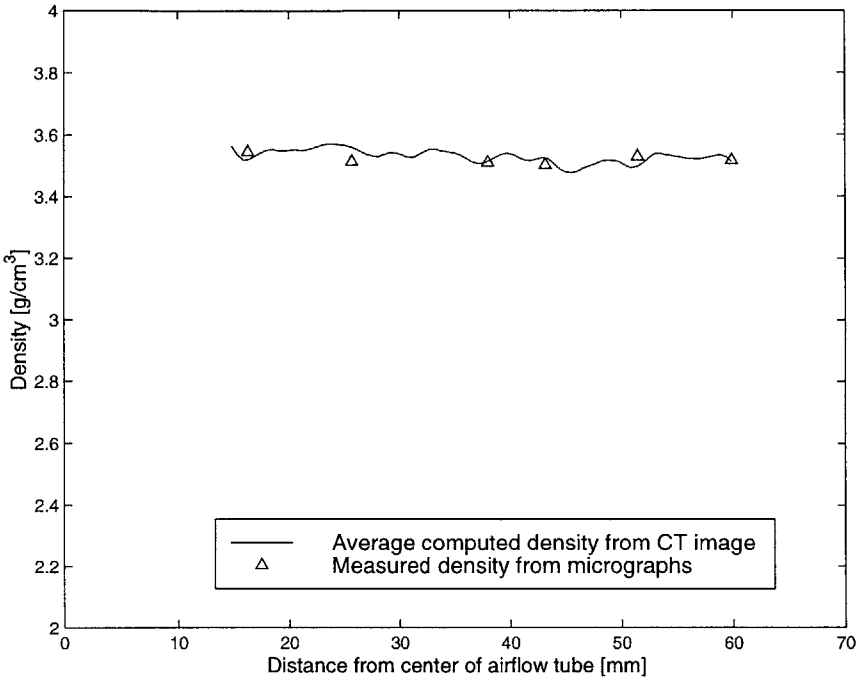

Figure 4-20: Density vs. radial position across the eutectic aluminum sample.

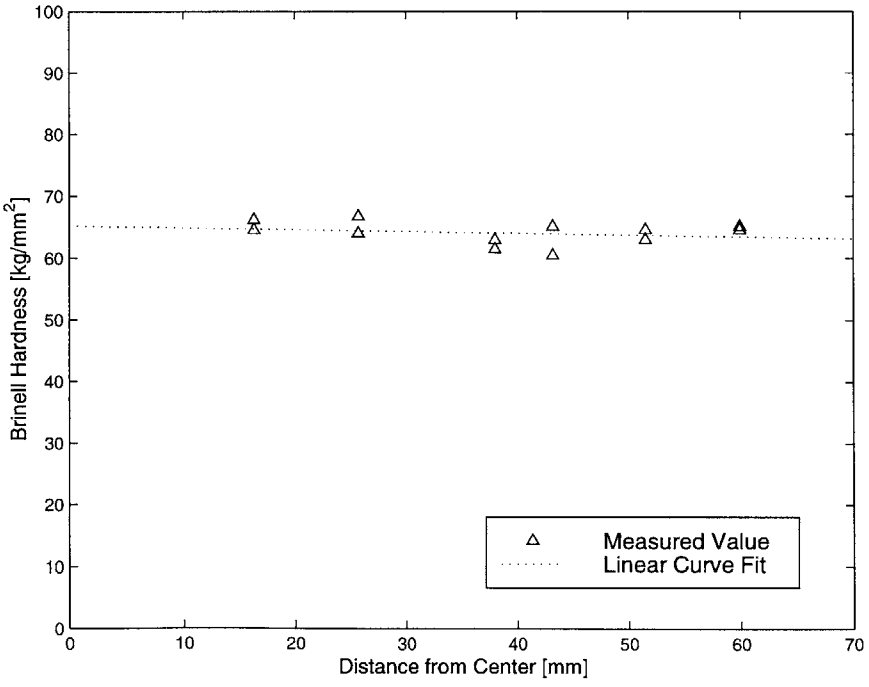

Figure 4-21: Hardness vs. radial position across the eutectic aluminum sample.

4.3 Commercial 6061 Aluminum Alloy

In the binary alloy solidification experiments, the Al-Cu composition was specifically chosen to achieve certain characteristics. Under that controlled set of conditions, the resulting solidification behavior and final microstructure were more or less expected. For this experiment however, a standard commercial aluminum alloy was picked essentially "off-the-shelf." The alloy chosen for this experiment was 6061 grade aluminum with a T6 temper designation. It is one of the most popular wrought alloys for use in heavy-duty structural components requiring good corrosion resistance and weldability. Applications include automobile, truck and railroad structures, furniture, and pipelines. The 6061 grade is typically produced in large quantities via direct-chill semi-continuous casting. The baseline composition of 6061 alloy is 1.0%Mg-0.6%Si-0.30%Cu-0.20%Cr with aluminum as the remainder. Its density at 20°C is 2.70 g/cm^3. The liquidus and solidus temperatures are 652°C and 582°C, respectively (Hatch, 1984). A commercial aluminum alloy, in particular 6061 grade, was chosen precisely because it is a common and important aluminum alloy. One major criterion in evaluating a comprehensive solidification sensor is its ability to perform successfully with real-world alloys in which the solidification phenomena are quite complex.

The 6061 alloy solidification experiment was similar to the previous three solidification experiments discussed in Sections 3.3 and 4.2. For the experiment, approximately 5 kg of 6061 alloy was melted in the crucible. Two thermocouples were used to monitor the temperature in the melt, one near the airflow tube and one near the crucible wall. The maximum temperature gradient achieved across the thermocouples was roughly 4°C. During the course of the experiment, a CT image was acquired approximately once every minute and the thermocouple readings were recorded once every second. The experiment lasted 150 minutes. It was terminated when the 6061 alloy solidified and reached a temperature of approximately 470°C, well below its solidus temperature. A total of 120 CT images were acquired. A single CT image was also acquired once the alloy had reached room temperature.

4.3.1 CT Results – Solidification Front Evolution

Figure 4-22 shows nine CT difference images from the solidification experiment using the 6061 aluminum alloy. The images shown were acquired over 106.5 minutes. Each image is 512 by 512 pixels in size, corresponding to a scaling of 0.53 mm/pixel. In a qualitative sense, the solidification behavior of the 6061 alloy lies between that of the Al-Cu hypoeutectic and the Al-Cu eutectic alloy. Unlike the hypoeutectic alloy case, a solidification front *is* distinguishable in these images. However, the 6061 alloy has a wide mushy zone spanning approximately 70°C. As a result, the solidification front position does not appear sharp as it was in the pure aluminum and eutectic alloy experiments. Instead, it is very diffuse.

After 40.9 minutes, solidification in the 6061 alloy has not yet begun (Figure 4-22a). However, after 49.5 minutes, a very faint solidification front is apparent around the cooling tube (Figure 4-22b). The solidification front continues to grow over the next 15 minutes (Figures 4-22c, 4-22d, and 4-22e). The casting begins to shrink after 69.2 minutes (Figure 4-22f). Small voids begin to form inside the aluminum after 80.4 minutes (Figure 4-22g). After 95.3 minutes, the alloy continues to solidify with more voids forming in its interior (Figure 4-22h). After 147.4 minutes, the 6061 alloy is completely solid with many small voids present in its interior (Figure 4-22i).

For comparison with the previous experiments, quantitative information regarding the evolution of the solidification was again acquired using a ROI analysis. The locations of two ROIs within the CT image are shown in Figure 4-23a. Figure 4-23b shows the computed density within the two ROIs as a function of time. The density evolution within the 6061 alloy is readily apparent. For ROI1, the density was observed to rise from a value of 2.38 g/cm^3 at time=0 minutes to a final value of 2.7 g/cm^3 at time=150 minutes. The density measured in ROI2 lagged in comparison to ROI1. This was expected since the alloy solidified from the interior. The density was observed to rise from a value of 2.36 g/cm^3 at time=0 minutes to a final value of 2.65 g/cm^3 at time=150 minutes.

The density evolution in the 6061 alloy is somewhat different than that noted in the previous three experiments. It can be divided into only two regimes. The first regime occurs when the alloy is still predominantly liquid. In this regime, the density slowly increases in a linear fashion. For ROI1, this regime occurred from time=0 minutes until time=50 minutes. In the second regime, the alloy enters the mushy condition and experiences a dramatic increase in the rate of density change. However, this density change is not linear. It follows a roughly exponential growth until it reaches an asymptote at the solid density (2.7 g/cm^3). For ROI1, the second regime occurred from time=50 minutes until the conclusion of the experiment.

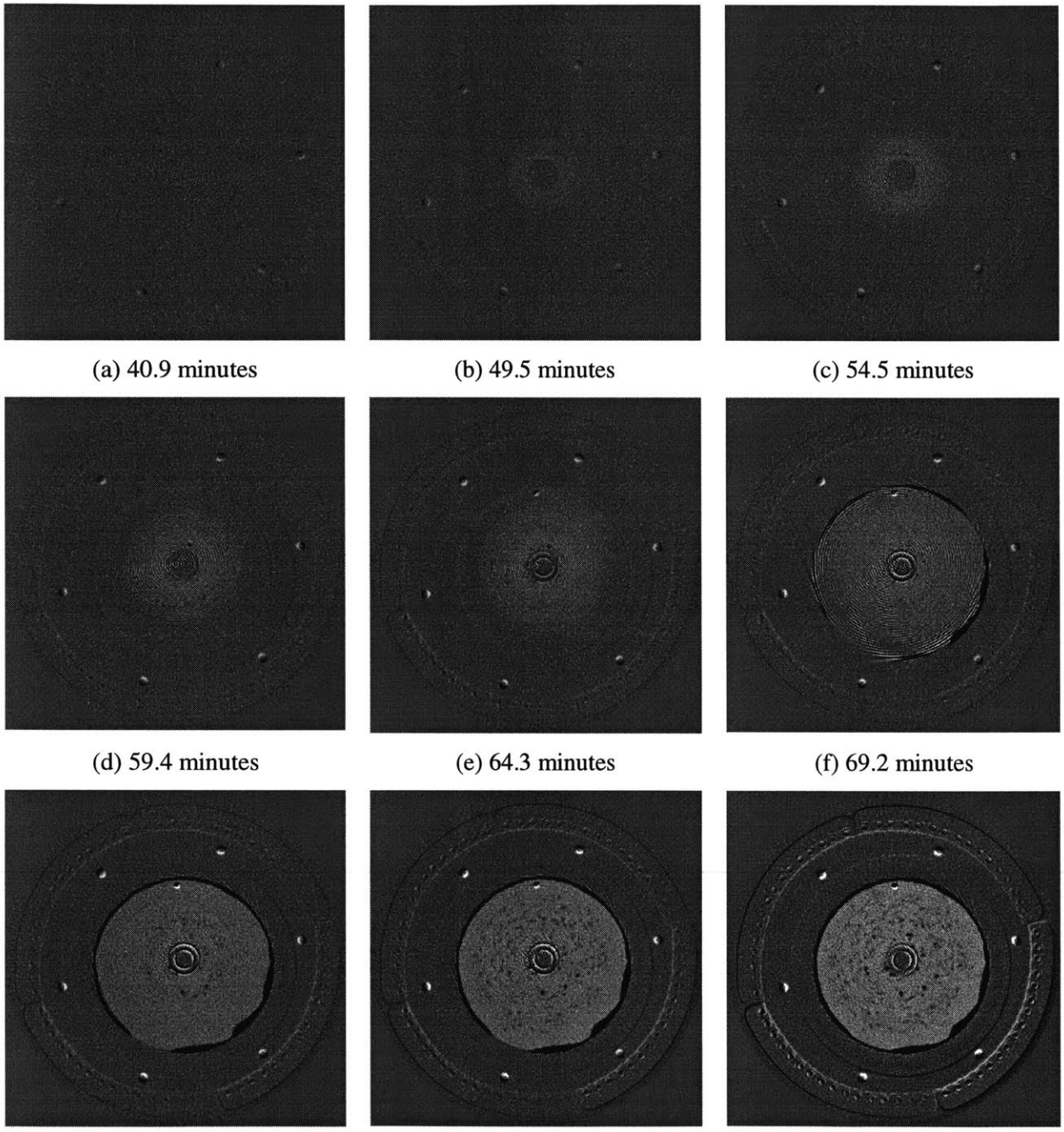

(a) 40.9 minutes (b) 49.5 minutes (c) 54.5 minutes

(d) 59.4 minutes (e) 64.3 minutes (f) 69.2 minutes

(g) 80.4 minutes (h) 95.3 minutes (i) 147.4 minutes

Figure 4-22: Nine difference images showing the evolution of solidification in the 6061 alloy over a period of 106.5 minutes, from (a) time=40.9 minutes to (i) time=147.4 minutes.

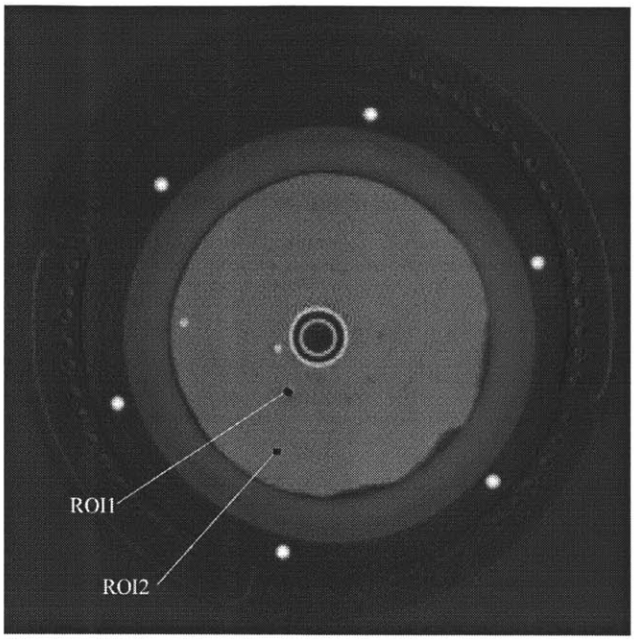

(a)

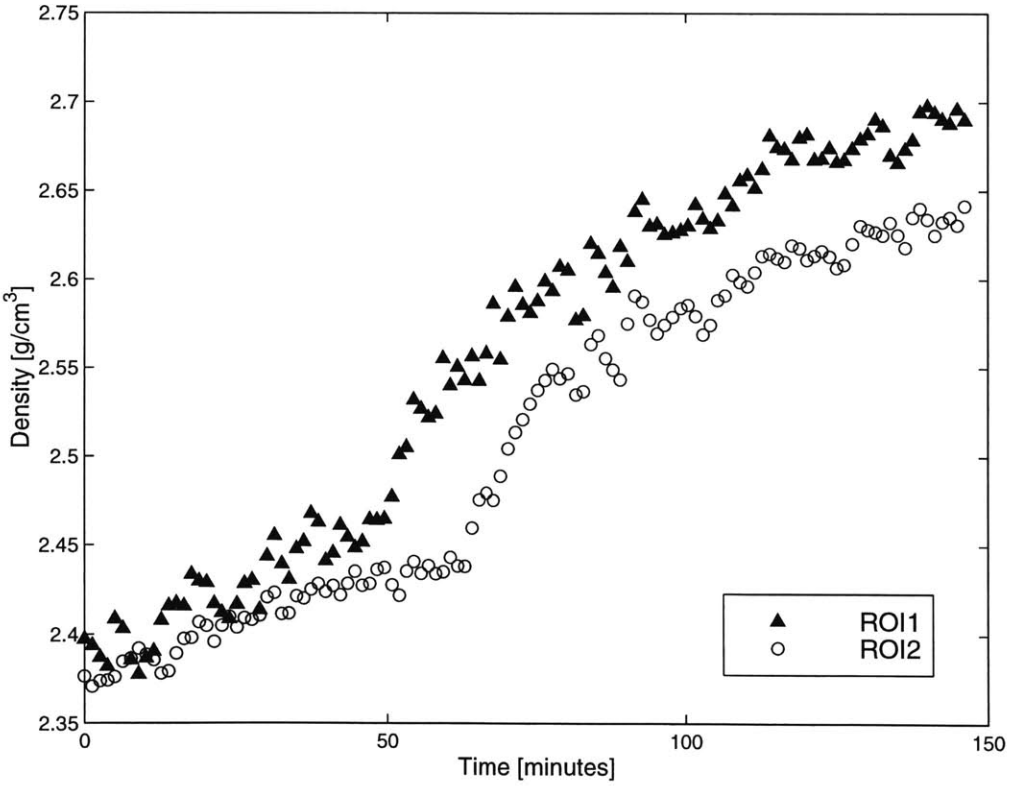

(b)

Figure 4-23: (a) Location of two ROIs in the CT image. (b) Computed density in both of the ROIs plotted over the time of the 6061 alloy solidification experiment.

4.3.2 CT Results – Void Detection

One of the main defects associated with casting is gas porosity and/or void formation (Piwonka and Flemings, 1966). Voids in a casting are problematic because they alter the physical and structural properties of the metal. Significant research has been devoted to understanding and predicting the mechanics of voids and porosity (Kubo and Pehlke, 1985; Poirier et al., 1987). One reason for void formation is because liquid metals show a strong affinity for dissolving gases. Aluminum, in particular, is very reactive with hydrogen. As the liquid metal solidifies, these gases are trapped in the solid, forming voids. Voids may also result from shrinkage porosity. This condition is caused by a dendritic growth tendency that seals off and prevents liquid from feeding between the dendrite branches and cells (Clark and Varney, 1958). Irrespective of their formation mechanism, a large number of voids were detected in the CT images of the solidification of the 6061 alloy. In-process void detection is a vital ancillary capability of a comprehensive solidification sensor. The accuracy of these results was evaluated.

Figure 4-24 shows a CT difference image of the solidified 6061 alloy. The locations of nine voids are marked with the letters A through I. The voids appear as dark spots inside the aluminum. The location of the two thermocouples is marked with 'TC'. As explained in Section 2.3.3, the CT image beam height was roughly 4.5 mm at the center of the object. As a result, the voids in Figure 4-24 may reside anywhere within the volume defined by the CT image plane and the 4.5 mm beam height. Figure 4-25 shows a schematic of some example void positions. Some voids may lie entirely within the beam (void 1) while some may be larger than the beam height (void 2). Others may be only partially inside the beam (void 3). Depending on the exact size, shape and location of the void relative to the x-ray beam, its representation in the CT image may be well visible, blurred, or even non-existent, subject to the specific partial volume effects.

To confirm the existence of the voids in the CT image, the 6061 sample was cut along roughly the same plane as that of the CT image. A precise cut was difficult because of the tapered cylindrical geometry of the casting. The sectioned surface was machined on a lathe and a photograph was taken. The result is shown in Figure 4-26a. The casting was then machined again. Approximately 1 mm of material was machined off the surface and a second photograph was taken. The result is shown in Figure 4-26b. This process was repeated twice more. Each time, approximately 1 mm of material was machined away. The resulting photographs are shown in Figures 4-26c and 4-26d, respectively. The notable voids found in the 6061 casting are marked with the letters A through H in the four photographs in Figure 4-26. Depending on their size and depth, some voids appear in more than one section. 'TC' indicates the position of the two thermocouples. This designation attempts to correlate the voids identified in the CT image to the actual voids in the casting.

Correlation of the CT image to the aluminum sections was performed by visual inspection. In Figure 4-26a, six voids (A,B,C,D,E,F) are visible which also are seen in the CT image. Six voids (B,C,D,E,F,G) are also visible in both Figure 4-26b and the CT image. In Figure 4-26c, only four voids (D,E,F,G) are visible which correlate to the CT image. Finally, only two voids (F,H) are visible in both Figure 4-26d and the CT image. Although this verification technique was very qualitative, it is obvious that there is a good correlation between the CT image and the actual location of the voids in the solidified casting. Theoretically, the smallest void able to be detected is limited only by the spatial resolution of the system. In this case, the smallest void size would be 1.76 mm. However, the detection ability benefits greatly from the high contrast between aluminum and the composition of the void, i.e. air. As a result, some voids smaller than 1.76 mm are detectable. Because the CT sensor is only capable of two-dimensional imaging, depth information about the voids in the casting cannot be determined. However, a narrower x-ray beam height coupled with a three-dimensional CT imaging scheme would easily produce a CT model showing a complete volumetric void distribution.

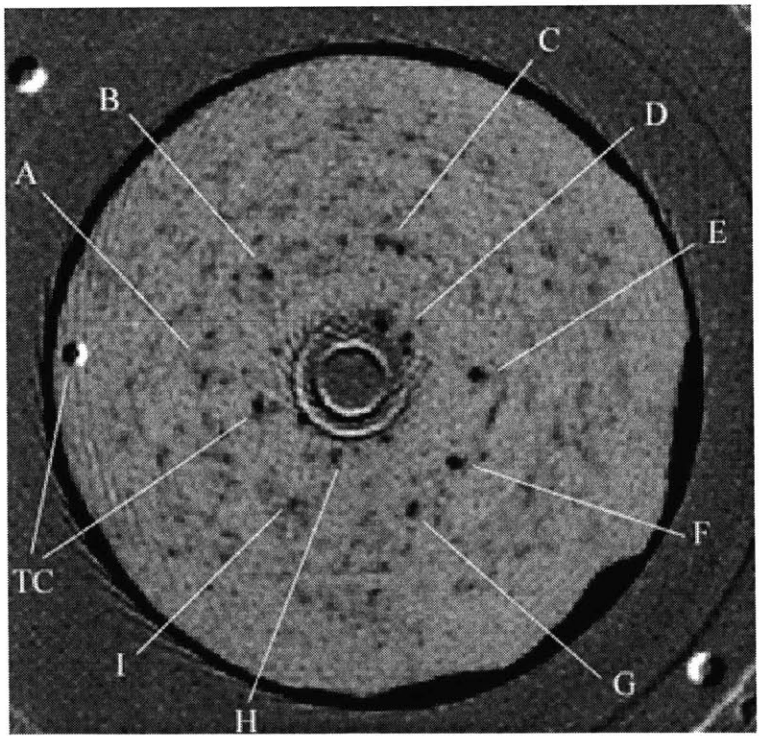

Figure 4-24: CT image of the 6061 aluminum sample. Major voids are marked.

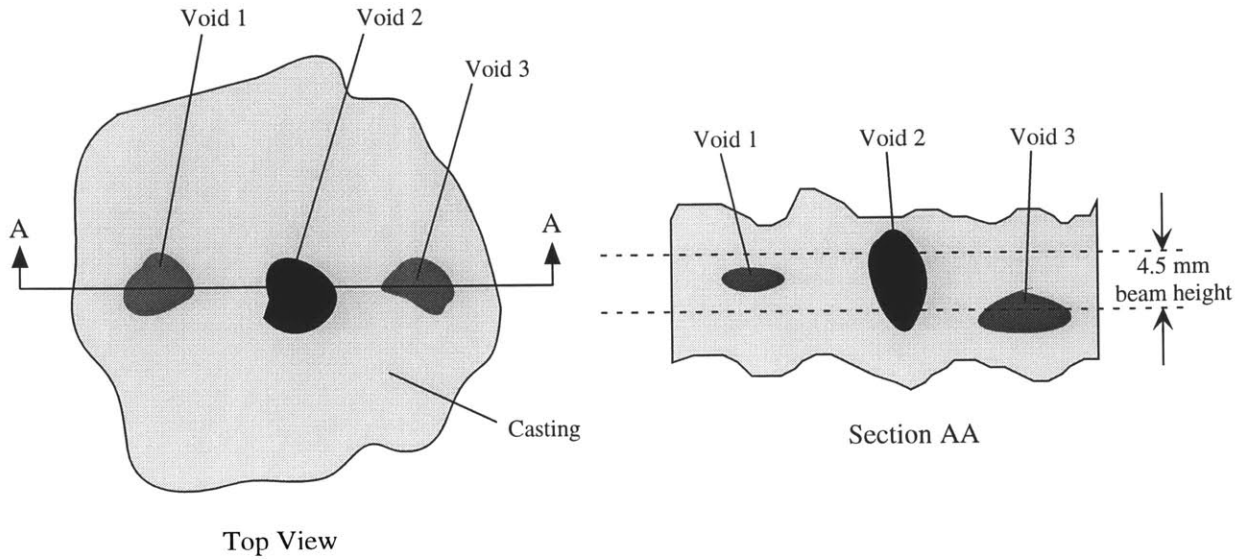

Figure 4-25: Schematic illustrating the different positions a void may have within the x-ray beam.

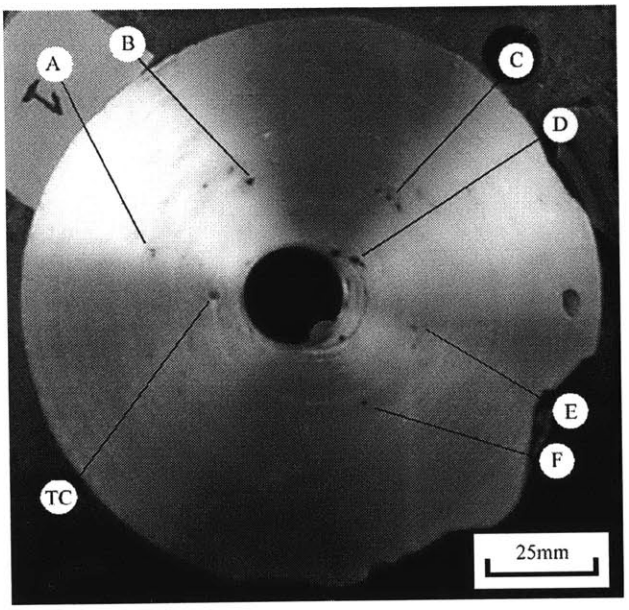

(a) Slice Plane No. 1

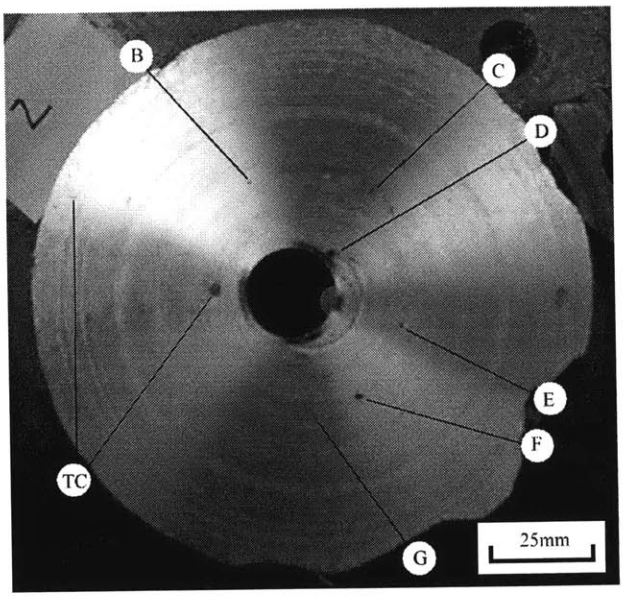

(b) Slice Plane No, 2

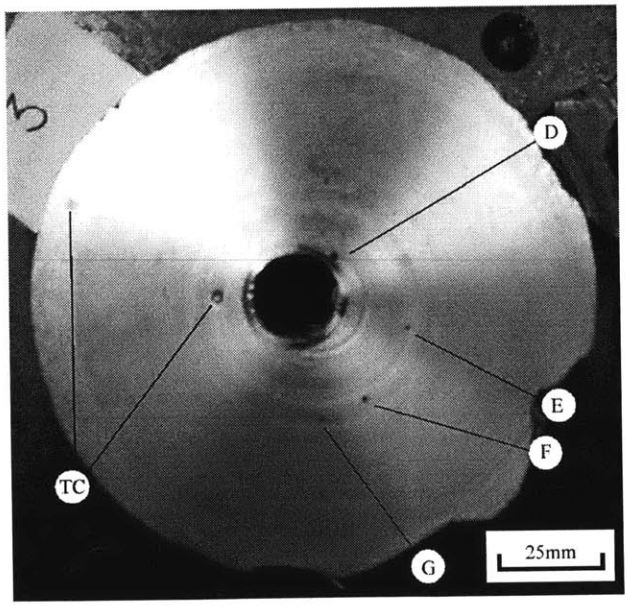

(c) Slice Plane No. 3

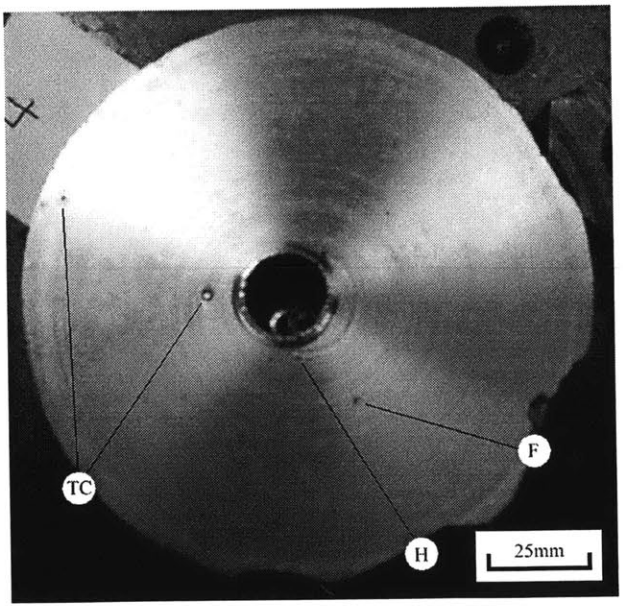

(d) Slice Plane No. 4

Figure 4-26: (a)-(d) Four pictures of the 6061 aluminum sample taken at four different slice planes. Each progressive image is approximately 1 mm below the surface of the previous image. Major voids are marked.

4.4 Discussion

4.4.1 Mushy Zone

Having established the ability of the CT sensor to detect the solidification front using the pure aluminum experiment, the aluminum alloy experiments tested its limits. This was a vital step because solidification of alloys is where most scientific and commercial interest lies. Alloys are troublesome because of their complex mushy zone. Specifically, the subtle density variations in the mushy zone pose a problem because of the high sensitivity needed for adequate characterization. In this series of experiments, the solidification behavior in the alloys was significantly more difficult to identify because of the presence of a mushy zone. The effect was most obvious in the solidification of the Al-11.2wt.%Cu because of the large difference between the liquid and solidus temperatures. The mushy zone was so large that the gradient between liquid, mushy zone, and solid could not be seen in across a single CT image. If the casting size or temperature gradient were larger, the entire range from liquid to mushy zone to solid could have possibly existed at one moment in time. However, the small casting size coupled with the small temperature gradient did not permit for this simultaneous condition. When a collection of CT images taken over the course of the experiment was examined, the information was quite limited. Only a progressive, homogenous increase in density could be seen.

This fact notwithstanding, the CT images still do provide useful data regarding the solidification of alloys. This was realized by using the ROI analysis technique. When plotted over time, the density in one small region is essentially a profile through the casting. The change in slope of the density-time curve distinguishes the change from liquid to mushy to solid during solidification. Figure 4-27 shows a simple schematic summarizing the density-time curves of the four solidification experiments. The shape of the density-time curve is dependent on the composition of the alloy. Pure metals and eutectics have density-time curves that are discontinuous. Alloys with a large mushy zone have density-time curves with very small slopes. It is hypothesized that various alloys can be categorized to a certain degree based on their inherent density-time curves. Particularly, the experimentally determined mushy zone transitions could aid computer modeling. By its nature, the ROI technique is limited to analysis of only one small region within the aluminum. However, a situation can be envisioned where many ROIs are used simultaneously to monitor the density change in critical areas of a casting. The results would show the "flow" of the solidification front and identify which locations solidify prematurely or belatedly. This would be a valuable tool for product design in identifying the location of hot spots, shrinkage, or porosity.

4.4.2 Compositional Variation

The micrograph analyses performed on the solidified Al-11.2wt.%Cu and Al-29.7wt.%Cu were done to confirm the density distributions predicted by the CT images. The Al-11.2wt.%Cu, in particular, was expected to solidify so that the $CuAl_2$-rich solute would be rejected ahead of the solidification front. This would have resulted in a variation in the copper concentration, increasing from the interior to the exterior of the casting. It was believed that this compositional variation could not be identified in the CT images because of the noise level and presence of artifacts. However, the CT image, micrograph analysis, and hardness measurements are all consistent and do not indicate any compositional deviations. Those results are only pertinent to the section of the casting scanned with the CT sensor. More than likely, some degree of copper rejection occurred at a different location in the casting. Given the 1.1% contrast resolution, this sensor should detect compositional variations resulting from solute rejection provided the density variation is 1.1% or larger. Verification of this assumption is left for future investigation.

4.4.3 Void Detection

Shrinkage, voids, and porosity are defects that plague the casting industry. Their formation is often spontaneous and unpredictable. This was the case here. The porosity and void formation that occurred during the 6061 alloy solidification experiment was completely unintentional. Regardless, their presence provides an excellent opportunity to assess the accuracy with which the CT sensor can detect their shape and position. Although the verification was limited to a crude visual inspection of cross-sections through the casting, the correlation with some of the major features was very strong. This is a beneficial finding because it implies that the sensor has the ability to not only monitor the solidification process, but also detect void and porosity formation *as it occurs*. Improved spatial resolution should detect increasingly smaller and smaller voids. In addition, the CT sensor could be used as a scientific tool for a more intensive study on the forces that drive shrinkage, voids, and porosity to determine how and why they happen.

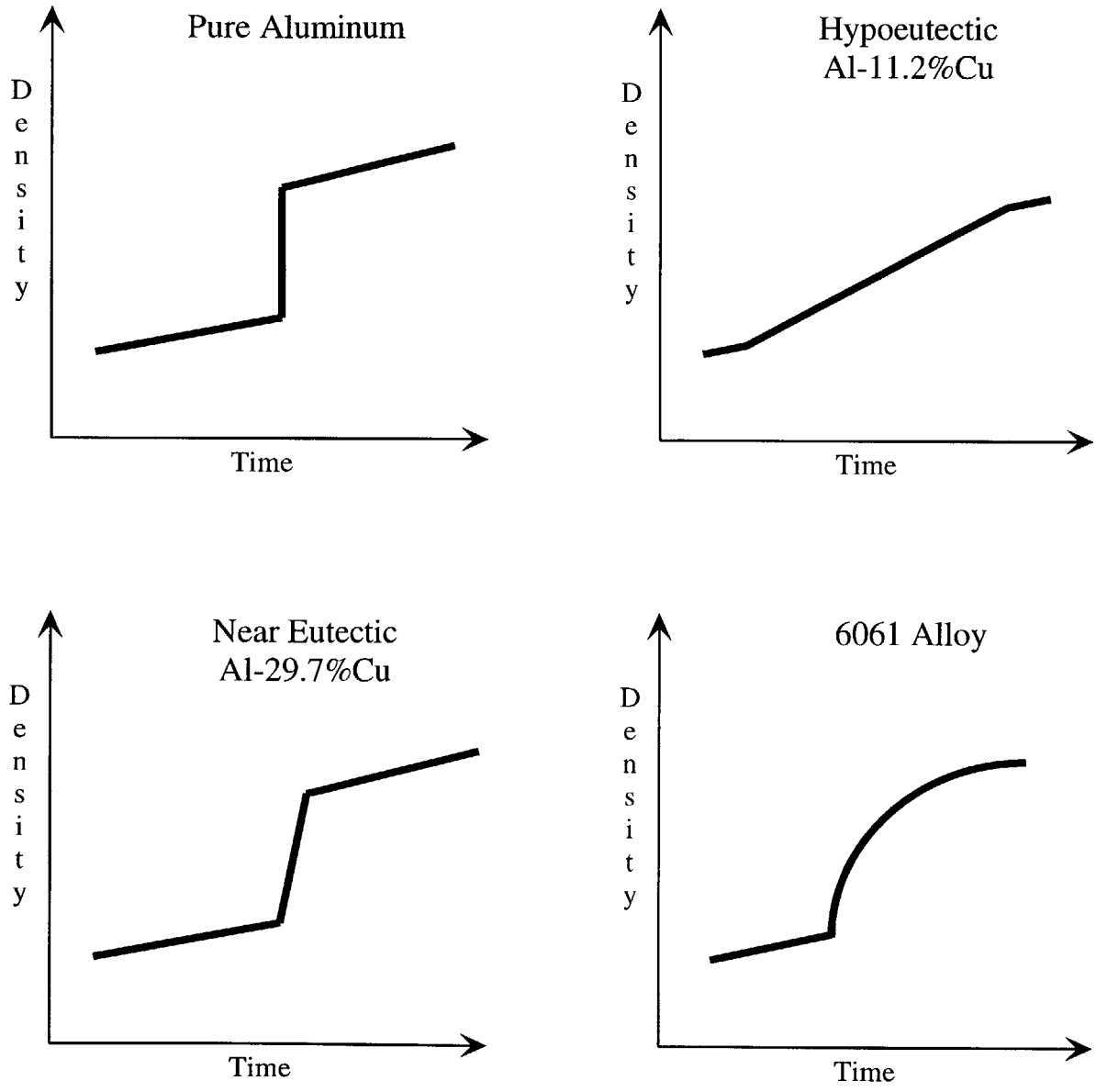

Figure 4-27: Comparison of the density evolution curves for the four aluminum solidification experiments.

Chapter 5 Summary and Conclusions

5.1 Implications of the Current Sensor

Although CT technology has existed since the 1970s, no previous attempt had been made to apply it as a tool in metal casting processes. In the past, limitations in x-ray source strength prevented serious pursuit of a CT-based sensor. However, the advent of modern, compact x-ray linear accelerators allows large, dense castings to be easily examined. As opposed to other non-invasive technologies, such as ultrasound, laser, eddy current, x-ray diffraction, or x-ray radiography, a CT-based sensor returns extremely comprehensive information regarding the evolution of the solidification front in a metal casting. The results of this work showcase the scientific and industrial potential that is offered by such a sensor system.

In its most basic capacity, time-lapse CT images are a two-dimensional visual history tracking the movement of the solidification front. Such information alone is beneficial for verification of computer solidification models. Further quantitative analyses of CT images yield specific values correlating to density for any region in a casting. These data shed light on the intricacies of mushy zone growth in alloys. In addition, a CT sensor of sufficient resolution can detect defects such as shrinkage, void formation, porosity, and compositional variation.

A CT sensor has great potential in the metal casting field based strictly on the quality of the data it generates. However, there are some drawbacks. Foremost is the severe radiation hazard created by a high-energy x-ray system. Any potential implementation requires extensive shielding and strict safety protocols. A second drawback is the significant cost. The majority of this cost resides with the x-ray source, a linear accelerator in this case. This factor alone limits the speed of any future implementation or development. The last drawback is the extreme precision required in both the design and operation of such a sensor. The degree to which noise and artifacts degrade CT image quality were clearly seen in this work. Additional factors such as a harsh industrial environment must be accounted for to prevent such degeneration in sensor performance.

5.2 Recommendations for Future Work

The current performance characteristics of the CT sensor include a 1.76 mm spatial resolution, a 4.5 mm beam height, a 1.1% contrast resolution, and a data acquisition time of approximately 2 minutes. The typical reconstruction time for a CT image ranges from 5 seconds to 60 minutes depending on the image parameters. Although these characteristics are adequate for continued laboratory experiments using this sensor, they have areas for improvement. For future industrial use in particular, the performance of the CT sensor must improve. There are two major criteria driving future sensor development: increased spatial resolution and shorter data acquisition time. The demand for increased spatial resolution is fueled by the need to understand the basic mechanisms of solidification: cell nucleation, dendrite growth, microporosity development, constituent segregation, etc. Such phenomena occur at or near the microscopic level. The demand for shortened data acquisition time is fueled by the need for a real-time sensor. Such a device could be implemented on-line as a casting process and quality control tool. Unfortunately, these demands are often mutually exclusive. An attempt was made to address some potential ways of improving the performance of both the current laboratory sensor and a future industrial-scale device. They are discussed on a component-by-component basis.

5.2.1 Improvements in X-Ray Source

Given the degree of complexity of the linear accelerator, most major improvements in its performance require large financial expenditure. As noted earlier, one source of noise and artifacts in the CT images was a result of both short- and long-term instabilities in the intensity of the x-ray output. Stabilizing the x-ray beam should be a priority for future development of the CT sensor. One option is to implement an automatic control unit to monitor and adjust for drift in the RF resonance frequency.

The spot size needs to be altered to improve spatial resolution. The spot size of the current linac is documented as 2.0 mm. The manufacturer has reported that new linac models have a spot size of 1.7 mm. Without changing any other parameters of the system, this 0.3 mm reduction in spot size would raise the theoretical spatial resolution from 1.34 mm to 1.27 mm. The added cost for such a limited improvement may not be worthwhile. Vertical spatial resolution and contrast resolution could also be improved through better source collimation. This would result in a narrower beam. Such an improvement may be necessary if a three-dimensional imaging capability is ever desired. However, added source collimation may reduce the number of emitted photons, which may increase data acquisition time.

For industrial use, the current linac may not have a satisfactory penetrating ability. Depending on the casting size and material, the x-ray attenuation may be so great that data acquisition time becomes

unduly long. This could be the case with steel or other high-density materials. The obvious solution would be to use a linac with an energy and dose rate sufficient enough to adequately penetrate the particular casting.

5.2.2 Improvements in Detector System

Data acquisition time and spatial resolution may be improved through modification of the detector array. For example, improving the efficiency of the detector array may decrease the data acquisition time. The efficiency of the current $CdWO_4$ crystals is only about 5%. Efficiency may be improved by substituting thicker $CdWO_4$ crystals into the current array or replacing the $CdWO_4$ crystals with a different detector material altogether. However, alternative crystal materials may be worse in other respects, such as a long afterglow. In addition to efficiency, changing the source-to-detector distance may increase the spatial resolution. However, as reported in Section 2.3.2 and Figure 2-12, little additional resolution would be gained since the geometry of the current system is nearly optimized.

5.2.3 Improvements in Positioning System

The current positioning system was developed for acquisition and reconstruction of two-dimensional images. Several simple modifications to the positioning stages would dramatically improve the performance of the current sensor. One improvement mentioned in Sections 2.3.5 and 3.5 is to increase the maximum velocity of the rotary stage. The current worm gear drive is susceptible to lockups at high speed, which limits the rate at which data can be acquired. Implementing a more reliable, higher speed system would significantly reduce data acquisition time. One possibility would be to use a linear-drive stage with servo-motors rather than the current stepper motor gear drive. However, caution must be exercised. If the accelerations imposed on the phantom by the rotary stage are too great, detrimental inertial effects become a problem. In particular, the solidification experiment could be disrupted.

A second simple improvement is to implement a closed-loop control routine. The current system operates by moving the stepper-motors a specified number of steps to a final position. Occasionally, positional accuracy is lost. With a shaft-mounted encoder, a closed-loop control scheme would effectively eliminate any positioning error. A final improvement of the current system is to add a third axis to facilitate three-dimensional tomography. A third axis would require linear vertical movement with the ability to support the load of the phantom and potentially, the other stages. Although the hardware design would require a notable effort, modifications to the data acquisition routine would be quite simple. A three-dimensional imaging capability would be beneficial for both solidification front observation and void detection.

The changes discussed thus far relate entirely to improving the current laboratory-based sensor. For industrial implementation, the positioning system would require significant modification. For example, the x-ray source and detector array would most likely be required to move about a fixed caster or casting. This would involve precise alignment and synchronization in movement. The specific design is dependent upon the particular industrial casting situation and implementation.

5.2.4 Improvements in CT Algorithm

The CT reconstruction algorithms used in this work were based on standard fan-beam filtered backprojection methods (Kak and Slaney, 1987). Minor customizations were made to accommodate the specific data acquisition method used herein. Typical reconstruction times ranged from 5 seconds to 60 minutes, depending on the number of angular views and the desired final image size. All processing was performed on a 200 MHz Intel PentiumPro®-based computer using the Microsoft Windows95® operating system. For this laboratory-based sensor, no premium was placed on reconstruction time. As a result, the performance of the reconstruction algorithm was adequate. For future development of the CT sensor, the method of both data acquisition and CT reconstruction should be improved upon. In particular, real-time or near-real-time performance is necessary for industrial implementation.

If the current data acquisition method and reconstruction algorithms are maintained, image reconstruction time could be improved through the use of dedicated computational hardware. Many medical and industrial CT scanners currently use such system architecture. In the current system, this would require design of customized computer hardware in addition to conversion and/or revision of the existing data acquisition and reconstruction software. Such an effort would involve significant cost with mostly limited returns.

A second course of action is the pursuit of alternative CT data acquisition and reconstruction procedures. These include such techniques as limited angle reconstruction and laminography. The latter avenue is the more logical venture if the CT sensor is eventually targeted for industrial application. Most industrial casting environments place considerable constraints on the allowable geometry, positioning, movement, and shielding of a potential solidification sensor. Given these constraints, a data acquisition scheme which requires 360° rotation about the casting is unrealistic. Any potential application will require data to be collected in a limited fashion while still maintaining rigorous performance specifications. Currently, Jureidini (1998) has examined alternative data acquisition and image reconstruction techniques specifically for this task.

5.2.5 Improvements in Solidification Platform

The solidification platform developed in this work was designed for melting aluminum and aluminum alloys. In addition, the air cooling system causes solidification from the interior of the casting. The experiments were carried out in a transient fashion; the aluminum was forcibly solidified over time. Although the current system performed remarkably well, there are several areas of improvement and redesign that can be done on the solidification platform.

One such improvement is to redesign the solidification platform so that the solidification front achieves a steady-state position with no movement. This can be done through a control process involving both active heating and cooling. Such a scheme was considered for the current system, but proved too difficult to implement. The large thermal mass of the aluminum coupled with the poor cooling from the pressurized airflow resulted in an unduly long response time. A steady-state solidification front is highly desirable because it would eliminate the transient conditions that create blurring and noise in the CT image.

A second improvement is to use an alternative cooling medium. The current system used pressurized air because it was simple to implement. However, the thermal capacity of air is quite low. This resulted in poor cooling rates and small thermal gradients in the casting. A medium such as water has a large thermal capacity. However, the risk of explosion is very high. A gas such as helium has a better thermal capacity than air. However, use of any gas other than air requires a recirculatory, closed-loop cooling system.

For more realistic casting conditions, the solidification platform should be modified so that the solidification front moves from the exterior of the casting inward. In addition, if porosity is to be controlled, molten aluminum should be cast in a controlled atmosphere, such as argon, to limit the hydrogen reaction. Other, non-cylindrical geometries should also be examined. In particular, it would be beneficial to test the CT sensor using discrete castings. Such experiments should yield interesting results in terms of solidification front movement and void formation.

Nomenclature

Symbol	Definition
A	Surface area
A_c	Cross-sectional area of flow
A_s	Total area of a micrograph
A_{side}	Surface area of the side of the crucible
A_{top}	Surface area of the top of the aluminum
A_{tube}	Surface area of the side of the airflow tube
A_α	Planar area of the alpha phase constituent in a micrograph
a	X-ray source spot size
C	Contrast resolution
D	Object dimension
D_h	Hydraulic diameter
d	Detector width
f	Friction factor
f_α	Fractional area of the alpha phase constituent in a micrograph
f_θ	Fractional area of the theta phase constituent in a micrograph
g	Gravitational acceleration
H_f	Heat of fusion
h	Heat transfer coefficient
I	Number of photons that pass through an object
I_o	Number of photons incident to an object
k	Thermal conductivity
L	Source-to-detector distance
L	Lengthscale
M	Mass ratio
m	Mass
N	Noise, measured as the standard deviation of pixel values in a selected area
N	Number of atoms per unit volume of traversed material
n	Number of view angles
Nu	Nusselt number
P	Probability of photon interaction
P	Wetted perimeter
p	Probability of photon interaction per unit length
$p(z,\theta)$	Radon transform projection
Pr	Prandtl number
Q	Volume flow rate
Q_L	Heat loss during solidification
$\dot{Q}_L$	Rate of heat loss
Q_M	Stored latent heat

q	Source-to-imaging-point distance
r	Spatial resolution
r_i	Radius of inner tube
r_o	Radius of outer tube
r_1	Radius of inner tube
r_2	Radius of outer tube
Ra	Rayleigh number
Re	Reynolds number
S	Signal, measured as the average pixel value in a selected area
T_a	Mean ambient temperature
T_M	Melting point temperature
T_o	Ambient temperature
T_r	Mean temperature
T_s	Surface temperature
t	Time
V	Velocity
V_s	Total volume of the specimen
V_α	Volumetric amount of the alpha phase constituent
V_θ	Volumetric amount of the theta phase constituent
x	Object coordinate system component
x	X-ray photon path length
y	Object coordinate system component
Z	Atomic number of a material
z	Projection coordinate system component
ε	Surface emittance
κ	Probability of pair production per atomic cross-section
μ	Mass attenuation coefficient
μ_o	Linear attenuation coefficient
ν	Kinematic viscosity
Ψ	Prandtl number function
ρ	Density of a material
ρ_s	Density of the binary specimen
ρ_α	Density of the alpha phase constituent
ρ_θ	Density of the theta phase constituent
σ	Probability of Compton scattering per atomic cross-section
σ	Stefan-Boltzmann constant
τ	Probability of photoelectric absorption per atomic cross-section
θ	Projection coordinate system component

References

Aluminum: Properties and Physical Metallurgy, ed. J. E. Hatch, American Society of Metals, Metals Park, OH, 1984.

B. H. Amstead, P. F. Ostwald, and M. L. Begeman, *Manufacturing Processes*, John Wiley and Sons, New York, 8th ed., 1987, pp. 23-25.

E. A. Avallone and T. Baumeister III, *Marks' Standard Handbook for Mechanical Engineers*, McGraw-Hill, Inc., New York, 9th ed., 1987.

J. A. Bakken and T. Bergstrom, "Heat Transfer Measurements During DC Casting of Aluminum, Part I: Measurement Technique," *Light Metals 1986*, The Metallurgical Society/AIME, Warrendale, PA, vol. 2, 1986, pp. 883-889.

M. B. Bever, "Introduction," *ASM Handbook: Metallography and Microstructures*, ASM International, Materials Park, OH, vol. 9, 1985, pp. 601-605.

M. Bobadilla, J. M. Jolivet, J. Y. Lamant, and M. Larrecq, "Continuous Casting of Steel: A Close Connection Between Solidification Studies and Industrial Process Development," *Materials Science and Engineering A*, vol. 173, 1993, pp. 275-285.

R. Bossi and G. Georgeson, "X-Ray Computed Tomography Analysis of Castings," *Light Metals 1992*, The Minerals, Metals & Materials Society, Warrendale, PA, 1992, pp. 901-905.

W. J. Boettinger, "Solidification Structures of Solid Solutions," *ASM Handbook: Metallography and Microstructures*, ASM International, Materials Park, OH, vol. 9, 1985, pp. 611-617.

T.F. Budinger and G.T. Gullberg, "Transverse Section Reconstruction of Gamma-Ray Emitting Radionuclides in Patients," *IEEE Transactions on Nuclear Science*, vol. NS-21, 1974, pp. 2-20.

P. Burstein, "Performance Issues in Computed Tomography Specifications," *Materials Evaluation*, vol. 48, 1990, pp. 579-593.

C. F. Chen and F. Chen, "Experimental Study of Directional Solidification of Aqueous Ammonium Chloride Solution," *Journal of Fluid Mechanics*, vol. 227, 1991, pp. 567-586.

S.E. Chidiac, J.K. Brimacombe, and I.V. Samarasekera, "A New Transient Method for Analysis of Solidification in the Continuous Casting of Metals," *Applied Scientific Research*, vol. 51, 1993, pp. 573-597.

H. Chikama, H. Shibata, T. Emi, and M. Suzuki, "*In-Situ* Real Time Observation of Planar to Cellular and Cellular to Dendridic Transition of Crystals Growing in Fe-C Alloy Melts," *Materials Transactions, JIM*, vol. 37, no. 4, 1996, pp. 620-626.

Z.-H. Cho, J.P. Jones, and M. Singh, *Foundations of Medical Imaging*, John Wiley and Sons, New York, 1993, pp. 71-88.

J. Chun, R. C. Lanza, and N. Saka, "Solid/Liquid Interface Detection in Continuous Casting Processes by γ-Ray Attenuation," Massachusetts Institute of Technology, Cambridge, MA, US Patent No. 5,509460, April 23, 1996.

J.-H. Chun, R. Lanza, N. Saka, and M. Hytros, " On-line Monitoring of the Solidification Front in Metal Casting," *Annals of the CIRP*, vol. 44, 1995, pp. 181-184.

D. S. Clark and W. R. Varney, *Physical Metallurgy for Engineers*, D. Von Nostrand, Inc., Princeton, NJ, 1958.

G. S. Cole, "Inhomogeneities and Their Control Via Solidification," *Metallurgical Transactions*, vol. 2, Feb. 1971, pp. 357-370.

D. C. Copley, J. W. Eberhard, and G. A. Mohr, "Computed Tomography Part 1: Introduction and Industrial Applications," *Journal of Metals*, January 1994, pp. 14-26.

P. A. Curreri and W. F. Kaukler, "Real-Time X-Ray Transmission Microscopy of Solidifying Al-In Alloys," *Metallurgical Transactions A*, vol. 27, 1996, pp. 801-808.

A. J. Dalhuijsen and A. Segal, "Comparison of Finite Element Techniques for Solidification Problems," *International Journal for Nuclear Methods in Engineering*, vol. 23, 1986, pp. 1807-1829.

G. N. Deryabina, "Controlling Thickness of Skin of Continuous Cast Billet," *Stal'*, vol. 5, 1980, p. 375.

G. N. Deryabina and A. G. Ripp, "Measuring the Ratio of Liquid Phase to Solid Phase in a Continuous Ingot," *Soviet Journal of Nondestructive Testing,* vol. 16, 1980, pp. 704-710.

Q. Z. Diao and H. L. Tsai, "Modeling of Solute Redistribution in the Mushy Zone during Solidification of Aluminum-Copper Alloys," Metallurgical Transactions, vol. 24A, 1993, pp. 963-972.

R. D. Evans, *The Atomic Nucleus*, McGraw-Hill, Inc., New York, 14th ed., 1972.

K. M. Fisher, "The Effects of Fluid Flow on The Solidification of Industrial Castings and Ingots," *PhysicoChemical Hydrodynamics*, vol. 2, 1981, pp. 311-326.

D. W. Fitting, W. P. Dube, T. A. Siewert and J. Paran, "A Process Sensor for Locating the Liquid-Solid Boundary through the Mold of a Casting," *Review of Progress in Quantitative Nondestructive Evaluation*, vol. 15, 1996, pp. 2315-2321.

M. C. Flemings, *Solidification Processing*, McGraw Hill Book Co., New York, 1974.

A. F. Giamei, "Solidification Process Modeling: Status and Barriers," *Journal of Metals*, January 1993, pp. 51-53.

M. E. Glicksman, R. N. Smith, S. P. Marsh, and R. Kuklinski, "Mushy Zone Modeling with Microstructural Coarsening Kinetics," *Metallurgical Transactions*, vol. 23A, 1992, pp. 659-667.

D. A. Granger, "Solidification Structures of Aluminum Alloy Ingots," *ASM Handbook: Metallography and Microstructures*, ASM International, Materials Park, OH, vol. 9, 1985, pp. 629-635.

A. G. Guy, *Elements of Physical Metallurgy*, Addison Wesley, Inc., Reading, MA, 1959.

R. C. Heine, C. R. Loper Jr., and P. C. Rosenthal, *Principles of Metal Casting*, McGraw Hill Book Co., New York, 1967.

S. H. C. Hughes, "Nonuniformity of Spatial Resolution in Computed Tomography Scanners," *Materials Evaluation*, vol. 48, 1990, pp.562-565.

M. Hytros, "A Feasibility Study of Solidification Front Monitoring via Tomographic Imaging," Massachusetts Institute of Technology, Cambridge, MA, Master's thesis, 1996.

K. A. Jackson, "Solidification Structures of Pure Metals," *ASM Handbook: Metallography and Microstructures*, ASM International, Materials Park, OH, vol. 9, 1985, pp. 607-610.

C.-K. Jen, B. Cao, K. T. Nguyen, C. A. Loong and J.-G. Legoux, "On-line Ultrasonic Monitoring of a Die-Casting Process Using Buffer Rods," *Ultrasonics*, vol. 35, 1997, pp. 335-344.

I. M. Jureidini, "A Design for a High Energy X-Ray Computed Tomography Sensor for the Study of Solidification Fronts in Aluminum," Massachusetts Institute of Technology, Cambridge, MA, Master's thesis, 1997.

I. M. Jureidini, "Design and Performance of a Compact High-Energy X-Ray Computed Tomography System for the Study of Solidifying Metals," Massachusetts Institute of Technology, Cambridge, MA, Doctoral thesis, 1998.

A. C. Kak and M. Slaney, *Principles of Computerized Tomographic Imaging*, IEEE Press, NY, 1987.

S. Kalpakjian, *Manufacturing Engineering and Technology*, Addison-Wesley, Inc., Reading, MA, 2nd ed., 1992.

W. Kaukler, F. Rosenberger and P. Curreri, "*In Situ* Studies of Precipitate Formation in Al-Pb Monotectic Solidification by X-Ray Transmission Microscopy," *Metallurgical Transactions A*, vol. 28, 1997, pp. 1705-1710.

C. V. Kropas, T. J. Moran, and R. N. Yancey, "Effect of Composition on Density Measurement by X-Ray Computed Tomography," *Materials Evaluation,* April 1991, pp. 487-490

K. Kubo and R. D. Pehlke, "Mathematical Modeling of Porosity Formation in Solidification," *Metallurgical Transactions B*, vol. 16B, 1985, pp. 359-366.

D. C. Kunerth and J. P. Wallace, "Eddy Current Study of Solidification in Lead and Lead 20 Pct Tin," *Metallurgical Transactions B*, vol. 11, 1980, pp. 273-283.

F. D. Lemkey and R. W. Kraft, "Solidification Structures of Eutectic Alloys," *ASM Handbook: Metallography and Microstructures*, ASM International, Materials Park, OH, vol. 9, 1985, pp. 618-622.

R.W. Lewis and P.M. Roberts, "Finite Element Simulation of Solidification Problems," *Applied Scientific Research*, vol. 44, 1987, pp. 61-92.

T. Matsumiya, W. Yamada, T. Ohashi, and O. Nittono, "*In Situ* Observation of Solidification of Silicon Steel by Synchrotron Radiation X-Ray Topography," *Metallurgical Transactions A*, vol. 18, 1987, pp. 723-727.

A. F. Mills, *Heat Transfer*, Richard D. Irwin, Inc., Homewood, IL, 1992.

L. F. Mondolfo, *Aluminum Alloys: Structure and Properties*, Butterworths Inc., Boston, 1976.

J. F. Moore, "Evolution of Computed Tomography," *Materials Evaluation*, vol. 48, 1990, pp. 630-640.

V. V. Nagarkar, J. S. Gordon, K. Daley, G. Entine and M. R. Squillante, "Automated Imaging of Semiconductor Crystal/Melt Interface Zone," *Applied Radiation and Isotopes*, vol. 44, 1993, pp. 1301-1311.

M. R. Ozgu, D. H. Bright and D. L. Watkins, "Experimental and Mathematical Study of Ingot Solidification, Mold Wall Deflection and Ingot-Mold Interfacial Gap Formation," *Proceedings of the 68th Steelmaking Conference*, vol. 68, 1985, pp. 315-329.

R. L. Parker, "Ultrasonic Measurement of Solid/Liquid Interface Position During Solidification and Melting of Iron and Steel," *Nondestructive Evaluation: Application to Materials Processing*, American Society for Metals, Metals Park, OH, 1983, pp. 23-25.

T. S. Piwonka and M. C. Flemings, "Pore Formation in Solidification," *Transactions of the Metallurgical Society of AIME*, vol. 236, 1966, pp. 1157-1165.

D. R. Poirier and G. H. Geiger, *Transport Phenomena in Materials Processing*, The Minerals, Metals and Materials Society, Warrendale, PA, 1994.

D. R. Poirier and E. J. Poirier, *Heat Transfer Fundamentals for Metal Casting*, The Minerals, Metals and Materials Society, Warrendale, PA, 2nd ed., 1994.

D. R. Poirier, K. Yeum, and A. L. Maples, "A Thermodynamic Prediction for Microporosity Formation in Aluminum-Rich Al-Cu Alloys," *Metallurgical Transactions A*, vol. 18A, 1987, pp.1979-1987.

R. E. Pool and J. N. Koster, "Visualization of Density Fields in Liquid Metals," *International Journal of Heat and Mass Transfer*, vol. 37, 1994, pp. 2583-2587.

G. V. Raynor, "Phase Diagrams and Their Determination," in *Physical Metallurgy*, ed. R. W. Cahn, North-Holland Publishing Company, Amsterdam, 1970.

J. B. Ross and K. McQueeney, "Computed Tomography Imaging of Turbine Blades," *Materials Evaluation*, Oct. 1990, pp. 1270-1273.

W. Rostoker and J. Dvorak, *Interpretation of Metallographic Structures*, Academic Press, New York, 1965.

J. Schade, K. D. Ives and W. A. Brown, "Operating Experiences with a Liquid Core Detection System at AK Steel's Ashland Slab Caster," *Iron and Steelmaker*, vol. 9, 1994, pp. 31-38.

D. J. Schneberk, S. G. Azevedo, H. E. Martz, and M. F. Skeate, "Sources of Error in Industrial Tomographic Reconstructions," *Materials Evaluation*, vol. 48, 1990, pp. 609-617.

Schonberg Radiation Corporation, *6 MeV MINAC: Operations and Maintenance Manual*, Santa Clara, CA, 1991.

S. Sen, W. F. Kaukler, P. Curreri and D. M. Stefanescu, "Dynamics of Solid/Liquid Interface Shape Evolution near an Insoluble Particle – An X-Ray Transmission Microscopy Investigation," *Metallurgical Transactions A*, vol. 28, 1997, pp. 2129-2135.

E.A. Sivers and M.D. Silver, "Performance of X-Ray Computed Tomographic Imaging Systems," *Materials Evaluation*, vol. 48, 1990, pp. 706-713.

C. J. Smithells. Metals Reference Book, Volume 3. Plenum Press, New York, 4th ed., 1967.

"Standard Hardness Conversion Tables for Metals," *1997 Annual Book of ASTM Standards*, sec. 3, vol. 3.01, ASTM, West Conshohocken, PA, 1997, pp. 264-283.

S. R. Story, R. B. Mahapatra, P. A. Woodberry, R. H. Davies, P. Larkin, and R. Serje, "Liquid Core Detection through Segment Load Measurements," *1993 Steelmaking Conference Proceedings*, 1993, pp. 405-413.

K. Suzuki, A. Hikata, and C. Elbaum, "Ultrasonic Technique for the Study of Solid-Liquid Interface in Metallic Alloys," Japanese Journal of Applied Physics, vol. 26, 1987, pp. 85-87.

J. B. Walter and K. L. Telschow, "Laser Ultrasonic Detection of the Solidification Front during Casting," *Review of Progress in Quantitative Nondestructive Evaluation*, vol. 15, 1996, pp. 607-613.

W. C. Winegard, *An Introduction to the Solidification of Metals*, The Institute of Metals, London, 1964.

V. E. Zinov'ev, *Handbook of Thermophysical Properties of Metals at High Temperatures*, Nova Science Publishers, Inc., New York, NY, 1996, pp. 139-142.

Appendix A Linear Accelerator

A.1 Component Description

As mentioned in Chapter 2, the linear accelerator comprised five major components: a control console; modulator unit; RF head; x-ray head; and water circulation unit. Each of these components is described in detail in the following sections.

A.1.1 Control Console

The control console contains most of the operating controls and indicators for the linac. It provides x-ray dose rate control, frequency control, and safety interlock information. Circuitry in the control console commands a motor-driven auto-transformer in the modulator unit, permitting adjustment of the AC supply to the modulator to obtain the correct pulse current to the magnetron, located in the RF head. The magnetron produces the microwave pulses that drive the x-ray head. A dosimeter in the control console monitors the radiation output of the x-ray head with a diode detector. The control console is located away from the remainder of the equipment, allowing for remote operation of the linac.

An integral part of the control console is the safety interlock circuitry. The safety interlocks monitor conditions necessary for safe operation. The interlock circuit is a sequential latching circuit that allows operation of the high voltage power supply only when all monitored conditions are ready. Each interlock circuit drives a status LED on the control console. Because the interlocks form a series circuit, all conditions monitored must be in an operational state for all the LEDs to light, progressing in a sequence. Should an interlock circuit detect a fault, the high voltage power is automatically turned off and the linac cannot be fired.

A.1.2 Modulator Unit

This assembly contains the high voltage pulse generating circuits that drive the RF system and accelerator gun, as well as the high voltage power supply. This circuit includes a pulse-forming network, the charging choke, a motor-driven auto-transformer, a three-phase step-up transformer, a three-phase high voltage rectifier, and a hydrogen thyratron tube. An external trigger drives the pulse-forming network at 180 Hz; the maximum and minimum pulse rates are 200 Hz and 50 Hz, respectively. Each pulse is 5 μs long. The pulses simultaneously excite the magnetron and the accelerator electron gun.

A.1.3 RF Head

This unit contains the pulse transformer, gun isolation transformer, accelerator grid control, mechanically-tunable magnetron, four-port circulator, water-cooled microwave power load, interconnecting waveguide, water circulating connections, and a sulfur-hexafluoride (SF_6) gas system for pressurizing the RF waveguide with a dielectric gas. The dielectric gas prevents arcing within the waveguide. The magnetron supplies RF energy to the tuned accelerator cavities in the x-ray head, while the electron gun produces electrons that are then accelerated by the RF energy. The radiation is produced in the x-band frequency at 9303 MHz.

A.1.4 X-ray Head

This assembly contains the linear accelerator that generates x-rays. The accelerator consists of an electron gun and a series of microwave accelerating cavities under vacuum. A 520 mm-long standing wave is produced in this accelerating section. An electronic vac-ion pump mounted on the accelerator maintains the vacuum. During each pulse, electrons are injected into the cavity with an energy of 15 keV and are accelerated to an energy of 6 MeV. The peak electron current during a pulse is 50 mA, with an average current of 50 μA. Two sets of electromagnetic steering coils provide beam steering, which centers the electron beam along the longitudinal axis of the accelerator cavities. Intense x-rays are created when the electron beam collides with a tungsten target wafer at the end of the x-ray head. The spot size is 2 mm. The x-rays produced are not monoenergetic, but range in intensity in a bremsstrahlung spectrum with a maximum of 6 MeV. The average x-ray intensity is 1.3 MeV (Jureidini, 1997).

A tungsten collimator mounted on the end of the x-ray head surrounds the tungsten target. The collimator attenuates the unwanted portion of the x-rays emitted by the target wafer, producing an x-ray beam with a 30° cone configuration. Figure 2-6 shows the x-ray head mounted in position on the optical table. For this project, the x-ray beam was further collimated to a 30° fan shape by using a brass insert and lead collimator, as shown in Figure 2-7. The theoretical beam height at the detectors is approximately 20 mm in size. This corresponds to a theoretical beam height of approximately 10 mm in the center of the CT field. The actual beam height in the center of the CT field was experimentally determined to be 4.5 mm, as discussed in Section 2.3.3.

A.1.5 Water Circulation Unit

This assembly consists of a closed-loop water-to-air heat exchanger (Neslab model HX-150) with a maximum flow capacity of approximately 6.3×10^{-5} m^3/s. The unit provides water cooling at 20°C to dissipate heat within both the RF head and x-ray head.

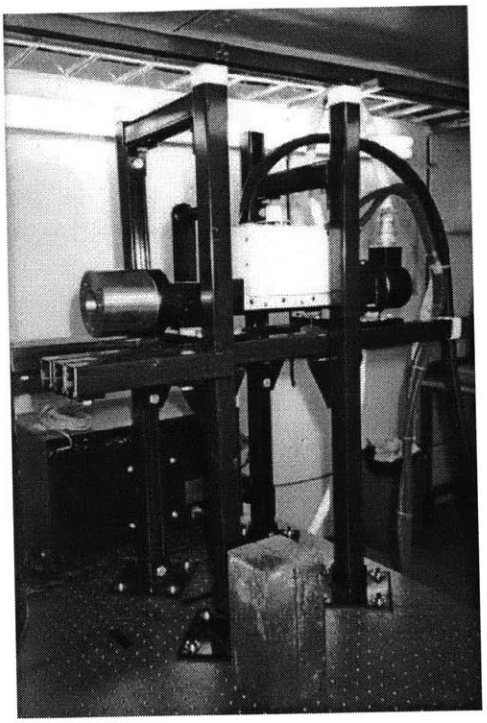

Figure A-1: The x-ray head of the linac mounted in position. Note the cylindrical tungsten collimator at left.

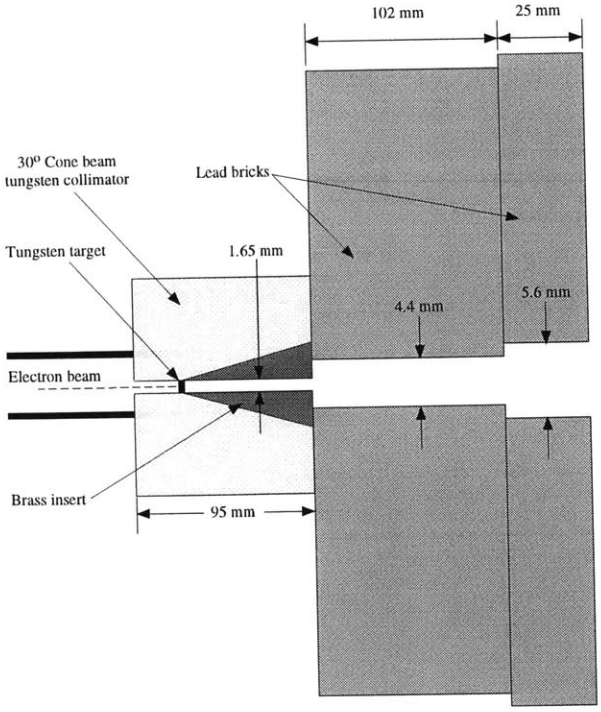

Figure A-2: Schematic of the x-ray head collimator design to attenuate the 30° cone beam into a 30° fan beam.

A.2 Shielded Laboratory Facility

The radiation hazards associated with the high intensity of the linac require a dedicated laboratory facility with proper x-ray shielding. The laboratory comprises a control room and a shielded concrete room. The control room houses the linac control unit, associated computer control equipment; it is the center of operations. The shielded room was designed and built with the linac specifications in mind and in accordance with proper radiation protection requirements. No personnel can be present inside the shielded room during linac operation.

The shielded room has 0.8 m thick concrete walls. The ceiling is composed of 0.6 m thick concrete ceiling blocks. In addition, the room has a maze-like entrance passage. Figure 2-12 shows the floorplan of the shielded room and the location of the CT sensor. To further attenuate x-rays in the forward beam direction, there is a lead wall, or beamstop, against the back wall. The beamstop is 2045 mm wide by 305 mm deep by 203 mm high. A reentrant design attenuates any back-scattered radiation. Ancillary lead is located around the x-ray head unit to reduce the amount of leakage radiation, reported to be 3 rads/min at 1 m (Schonberg, 1991).

Prior to construction of the facility, a Monte Carlo simulation was performed to determine the adequacy of the design (Jureidini, 1997). The program simulated the room geometry and the x-ray output from the linac. The radiation dose outside the room was calculated to be 0.02 mR/hr in the forward beam direction and 0.16 mR/hr at 90° to the linac target. In addition, the dose in the maze passage was calculated to be 0.014 mR/hr.

The actual radiation dose delivered by the linac outside of the shielded room was measured once construction was completed. The measurements were made using hand-held radiation dosimeters. Approximately 0.2 to 0.4 mR/hr was detected near the top of the wall in the forward beam direction. This higher than expected level was a result of radiation scattered upward from the lead beamstop. Background levels of radiation were found along all other points on the wall in the forward beam direction as well as along all of the side walls. Background levels were detected in the control room area. A dose of 1.3 mR/hr was found at the outlet of the maze passage and 0.3 mR/hr at the entrance of the shielded room. The radiation level at all critical points was below 0.5 mR/hr, which is the required guideline for a controlled radiation facility.

For additional radiation safety, a search-out system for the shielded room was added to the linac interlock system. The search-out ensures that no personnel are present inside the room prior to or during linac operation. The procedure requires the operator to:

1. Enter the shielded room and close the access door
2. Visually inspect the room to verify no one is inside
3. Secure the first interlock station at the rear of the room
4. Secure the second interlock station at the opening of the entrance maze
5. Open the access door and exit the shielded room
6. Close the access door and secure the last interlock station outside of the door

Once the search-out procedure is completed, the shielded room is secure and the linac can be operated. In case of emergency, there are several methods of breaking the interlock and shutting down the linac. These include two emergency off switches inside the shielded room and one emergency off switch on the linac control panel.

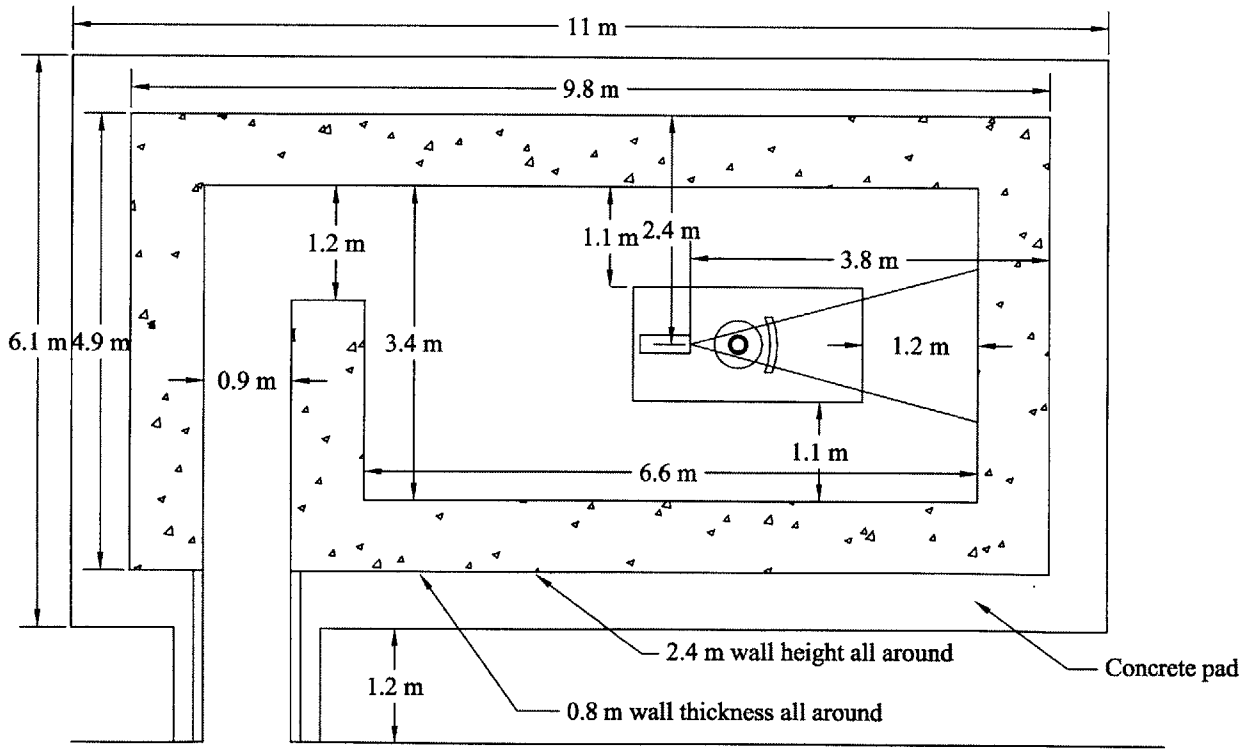

Figure A-3: Floorplan of the shielded room designed to house the high-energy CT sensor.

A.3 Linear Accelerator Operation

During normal operation of this CT sensor, the acquisition of a CT scan begins by mounting a phantom on the rotary stage of the positioning system. The phantom is positioned so that the desired cross-section for imaging is in line with the x-ray fan beam. The shielded room is then secured. Power to the linac and the data acquisition system is turned on. When the linac completes its warm-up cycle (approximately 15 minutes), it is ready. Activation of the x-rays involves several steps. First, the "x-ray on" switch located on the linac control console is depressed. Next, power to the modulator is increased until the input is approximately 11 kV. The frequency of the RF energy is then tuned to maximize x-ray intensity. Monitoring the output of the 64 detectors positioned behind the x-ray head of the linac aids the tuning process. It should be noted that the x-ray output is rather unstable and prone to drift at startup. The linac requires approximately 15 to 20 minutes to thermally stabilize in addition to the warm-up cycle. Then, the output is steady enough for a CT scan.

Appendix B Solidification Model

B.1 Model Description

An analytical model of the heat transfer within the system predicted the performance of the solidification platform. The goal of this model is to provide an estimate of the solidification time in a typical experiment using pure aluminum. Although several sources, such as Flemings (1974) and Poirier and Geiger (1994), provide methods for determining the solidification time and solidification growth of a cast metal, the present model derives from a basic enthalpy analysis tailored to this specific problem. This simple model equates the heat lost during solidification, Q_L, to the latent heat stored in the aluminum, Q_M, as outlined by Poirier and Poirier (1994):

$$Q_M = Q_L \tag{B.1}$$

The latent heat is equal to the product of the mass, m, and the heat of fusion, H_f, of the aluminum. As a result, Equation B.1 can be rewritten as:

$$mH_f = Q_L \tag{B.2}$$

This relation assumes that the aluminum is not superheated. The heat loss may be generalized as:

$$Q_L = \dot{Q}_L t \tag{B.3}$$

where $\dot{Q}_L$ is the rate of heat loss and t is the solidification time. Furthermore, the rate of heat loss may be rewritten as:

$$\dot{Q}_L = hA(T_M - T_o) \tag{B.4}$$

where h is the heat transfer coefficient, A is the surface area perpendicular to the heat flux, T_M is the melting temperature of the aluminum, and T_o is the ambient temperature. Heat loss may occur via three mechanisms: conduction; convection; and radiation. This simplified model assumes that there are only five routes by which heat is lost from the aluminum, as shown in Figure B-1. These are forced convection through the airflow tube, natural convection from the top of the aluminum, natural convection from the sides of the crucible, radiation from the top of the aluminum, and radiation from the sides of the crucible. Using these five sources of heat loss, Equations B.2 and B.3 may be combined to solve for solidification time of the aluminum:

$$t = \frac{mH_f}{\sum_{i=1}^{5} \dot{Q}_{Li}} \qquad \text{B.5}$$

where each of the five sources of heat loss must first be determined before evaluating the numerator. Although there are five methods of heat loss, there are only three surfaces through which the heat loss occurs: the surface comprising the airflow tube, A_{tube}, the surface comprising the sides of the crucible, A_{side}, and the surface comprising the top of the aluminum, A_{top}. Figure B-2 shows a schematic of the three surfaces with relevant dimensions. Based on these dimensions, the areas of the three surfaces are:

$$A_{tube} = 1.42\times10^{-2}\ \text{m}^2$$
$$A_{side} = 1.33\times10^{-1}\ \text{m}^2$$
$$A_{top} = 1.72\times10^{-2}\ \text{m}^2$$

It is assumed that no heat is transferred through either the tube bottom or the crucible bottom. As a result, the area calculations do not include their contribution. Calculation of each of the heat transfer coefficients is presented in the following three sections.

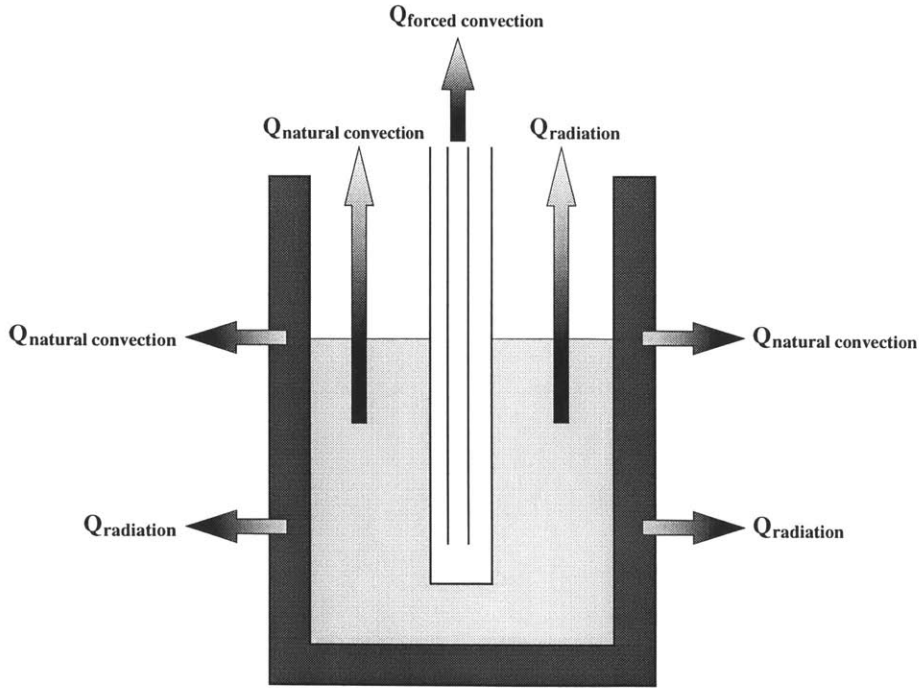

Figure B-1: Model of heat loss mechanisms for the solidification platform.

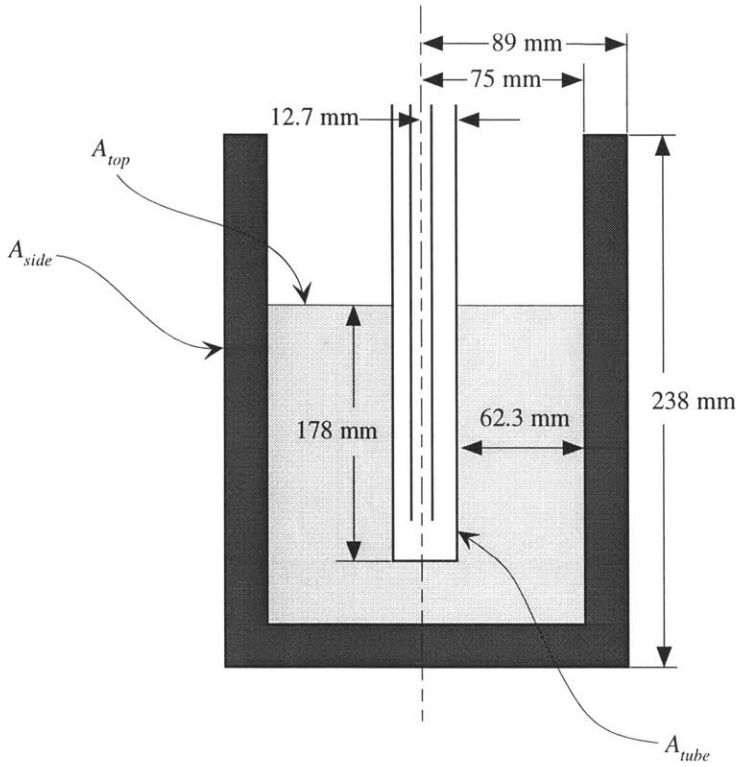

Figure B-2: Schematic of model geometry with dimensions.

B.2 Forced Convection Heat Transfer

The main source of heat loss in the aluminum is by forced convection through the airflow tube. The heat transfer coefficient for the forced convective flow can be calculated using the dimensionless Reynolds and Nusselt numbers, Re and Nu, in which:

$$\mathrm{Re} = \frac{\rho V D_h}{\nu} \tag{B.6}$$

and

$$\mathrm{Nu} = \frac{h D_h}{k} \tag{B.7}$$

where ρ is the density of the air, V is the velocity of the airflow, D_h is the hydraulic diameter of the airflow tube, ν is the kinematic viscosity of the air, and k is the conductivity of the air. Experimentally, the inflow and outflow air temperatures were measured at T_i=30°C and T_o=200°C, respectively. As a result, the material properties of the air were evaluated at a mean air temperature of T_f=115°C. The

density, conductivity, kinematic viscosity, and the dimensionless Prandtl number for air at 115°C are ρ=0.911 kg/m^3, k=3.238×10^{-2} W/m·K, ν=24.208×10^{-6} m^2/s, and Pr=0.69, respectively. The equivalent hydraulic diameter is required for the annular geometry of the airflow tube. It is defined as:

$$D_h = \frac{4A_c}{P} \tag{B.8}$$

where A_c is the cross-sectional area and P is the wetted perimeter. The cross-sectional area of flow for the annular passage and the wetted perimeter are defined as:

$$A_c = \pi(r_2^2 - r_1^2) \tag{B.9}$$

$$P = 2\pi(r_1 + r_2) \tag{B.10}$$

where the inner tube diameter, r_1, is 7.95 mm and the outer tube diameter, r_2, is 11.45 mm. As a result:

$$A_c = 2.13\times10^{-4}\ \text{m}^2$$
$$P = 1.22\times10^{-1}\ \text{m}$$
$$D_h = 6.98\times10^{-3}\ \text{m}$$

The flow rate, Q, of the air through the cooling tube was experimentally measured to be 3.3×10^{-3} m^3/s. The velocity, V, along the annular passage in the airflow tube is therefore:

$$V = \frac{Q}{A_c} \tag{B.11}$$
$$V = 15.49\ \text{m/s}$$

From Equation B.6, the Reynolds number was calculated as:

$$\text{Re} = 4069$$

For forced convection through an enclosed tube, transition to turbulent flow occurs at Re≅2300. For a hydrodynamically fully developed flow, the friction factor, f, for a smooth wall, is defined by Petukhov's formula (Mills, 1992):

$$f = (0.790\ln\text{Re} - 1.64)^{-2} \tag{B.12}$$

Using Equation B.12, the friction factor is:

$$f = 4.1\times10^{-2}$$

The Nusselt number for turbulent flow through an enclosed tube is found using Gnielinski's formula (Mills, 1992):

$$\mathrm{Nu} = \frac{(f/8)(\mathrm{Re}-1000)\,\mathrm{Pr}}{1+12.7(f/8)^{1/2}(\mathrm{Pr}^{2/3}-1)} \qquad \text{B.13}$$

Evaluating Equation B.13, the Nusselt number is:

$$\mathrm{Nu} = 13.55$$

Because of the annular geometry of the airflow tube, the Nusselt number requires a correction factor. Petukov and Roizen (Mills, 1992) define this correction factor as :

$$1-0.14\left(\frac{2r_i}{2r_o}\right)^{0.6} \qquad \text{B.14}$$

Using the correction factor from Equation B.14, the corrected Nusselt number is:

$$\mathrm{Nu} = 12.06$$

Finally, by rearranging Equation B.7, the heat transfer coefficient for the forced convection in the airflow tube is:

$$h = h_l = 55.95\ \mathrm{W/m^2\cdot K}$$

B.3 Natural Convection Heat Transfer

Heat transfer by natural convection occurs along the outside walls of the crucible in addition to along the top of the aluminum. The heat transfer coefficient for these two cases is found by calculating the dimensionless Rayleigh and Nusselt numbers:

$$\mathrm{Ra} = \frac{(T_s - T_o)gL^3\,\mathrm{Pr}}{T_r\nu} \qquad \text{B.15}$$

where T_s is the surface temperature, T_o is the ambient temperature, g is the acceleration due to gravity, 9.8 $\mathrm{m/s^2}$, L is the lengthscale, and T_r is the mean air temperature. Experimentally, the ambient temperature inside the furnace during solidification was measured at roughly 645°C.

In the case of natural convection along the crucible wall, it is assumed that there was no temperature gradient. As a result, the surface temperature of the crucible and the surface temperature of the top of the aluminum are assumed to be at the melting point. The resultant mean air temperature is 925.5°K. The material properties of air at this temperature are ν=103.37×10^{-6} m^2/s, k=6.30×10^{-2} W/m·K, and Pr=0.70. The height of the crucible wall, L=0.238 m, was chosen as the lengthscale. Using Equation 3.15, the Rayleigh number is:

$$\mathrm{Ra} = 2.48\times10^{6}$$

There is laminar flow exists for Ra<10^9. The Nusselt number is found using the relation provided by Churchill and Chu (Mills, 1992) for laminar flow along a plate with a sharp leading edge :

$$\mathrm{Nu} = 0.68 + 0.670(\mathrm{Ra}\Psi)^{1/4} \qquad \text{B.16}$$

where Ψ is the Prandtl number function. For this case, Ψ=0.345. From Equation B.16, the resultant Nusselt number for natural convection along the crucible wall is:

$$\mathrm{Nu} = 21.05$$

when the lengthscale, L, is substituted for the hydraulic diameter, D_h, in Equation B.7, the heat transfer coefficient for the case of natural convection along the crucible wall is:

$$h = h_2 = 5.57 \text{ W/m}^2\cdot\text{K}$$

For natural convection along the top of the aluminum, the inside diameter of the crucible was chosen as the lengthscale, L=0.15 m. The remaining material parameters are the same as those used for the case of natural convection along the crucible wall. From Equation B.15, the Rayleigh number is:

$$\mathrm{Ra} = 1.56\times10^{6}$$

Again, the natural convection is laminar. The Nusselt number for laminar natural convection along a heated horizontal plate is given by McAdams (Mills, 1992):

$$\mathrm{Nu} = 0.54\mathrm{Ra}^{1/4} \qquad \text{B.17}$$

Using Equation B.17, the Nusselt number for natural convection along the top of the aluminum is:

$$\mathrm{Nu} = 19.09$$

Rearranging Equation B.7, the resultant heat transfer coefficient for natural convection along the top of the aluminum is:

$$h = h_3 = 8.02 \text{ W/m}^2\cdot\text{K}$$

B.4 Radiation Heat Transfer

As is the case for natural convection, heat transfer by radiation occurs along the outside walls of the crucible as well as along the top of the aluminum. In the model, the crucible wall and the top of the aluminum are patterned as gray bodies. In addition, the view factors between the crucible wall and its surroundings and the aluminum top and its surroundings are assumed to be unity. The heat transfer coefficient for radiation from a gray body can be linearized (Mills, 1992):

$$h = 4\varepsilon\sigma T_r^4 \qquad \text{B.18}$$

where ε is the emittance of the surface, σ is the Stefan-Boltzmann constant, 5.67×10^{-8}, and T_r is the mean air temperature. The mean air temperature is assumed to be the same as that used in the case of natural convection. The emittance for the crucible wall was 0.81. The emittance for the aluminum was 0.325. Using Equation B.18, the heat transfer coefficient for radiation from the crucible wall is:

$$h = h_4 = 145.63 \text{ W/m}^2\cdot\text{K}$$

The heat transfer coefficient for radiation from the aluminum is:

$$h = h_5 = 58.43 \text{ W/m}^2\cdot\text{K}$$

B.5 Model Results

Having determined the heat transfer coefficient for each of the five methods of heat loss, Equation B.4 can be substituted into Equation B.5:

$$t = \frac{mH_f}{h_1 A_{tube}(T_M - T_o) + (h_2 A_{side} + h_3 A_{top} + h_4 A_{side} + h_5 A_{top})(T_M - T_a)} \qquad \text{B.19}$$

where T_o is the mean air temperature in the airflow tube and T_a is the mean ambient air temperature in the furnace. The model parameters chosen were m=5 kg, H_f=3.91×10^5 J/kg, T_o=115°C, T_M=660°C, and T_a=645°C. Using Equation B.19, the estimated solidification time with no superheat is:

$$t = 2600 \text{ seconds} \approx 44 \text{ minutes}$$